# Structure of 12Be via the study of multi-neutron decays and two-neutron correlations

Armel Kamenyero

Normandie Université

# THÈSE

## Pour obtenir le diplôme de doctorat

**Spécialité PHYSIQUE**

**Préparée au sein de l'Université de Caen Normandie**

# Structure of 12Be via the study of multi-neutron decays and two-neutron correlations

## Présentée et soutenue par
## ARMEL KAMENYERO

| Thèse soutenue le 24/02/2022 devant le jury composé de | | |
|---|---|---|
| M. DIDIER BEAUMEL | Directeur de recherche au CNRS, Labo. de Physique des 2 Infinis Irène Joliot-Curie | Rapporteur du jury |
| MME ANNA CORSI | Ingénieur HDR, CEA Paris-Saclay | Rapporteur du jury |
| MME MARLÈNE ASSIE | Chargé de recherche, Labo. de Physique des 2 Infinis Irène Joliot-Curie | Membre du jury |
| M. FRANCOIS DE OLIVEIRA SANTOS | Directeur de recherche au CNRS, 14 GANIL de CAEN | Président du jury |
| M. OLIVIER SORLIN | Directeur de recherche au CNRS, 14 GANIL de CAEN | Directeur de thèse |
| M. MIGUEL MARQUES | Directeur de recherche au CNRS, Laboratoire de Physique corpusculaire | Co-directeur de thèse |

**Thèse dirigée par OLIVIER SORLIN (Grand accélérateur national d'ions lourds) et MIGUEL MARQUES (Laboratoire de Physique corpusculaire),**

UNIVERSITÉ CAEN NORMANDIE

ED 591 PSIME

GANIL spiral2 laboratoire commun CEA/DRF CNRS/IN2P3

# Acknowledgements

I would like to start by thanking everyone who contributed to the success of this work.

First, I would like to express my heartfelt thanks to my supervisors Olivier SORLIN and Miguel MARQUES for giving me the opportunity to work on this topic and for their guidance and support, especially when things were not easy.

My gratitude to François DE OLIVEIRA, Didier BEAUMEL, Anna CORSI and Marlène ASSIE for taking their time to read the PhD thesis. I also wish to thank Christelle STODEL, Laurent MAUNOURY and Olivier LOPEZ for the follow up and the encouraging words.

Let me take this opportunity to also thank all the fellow PhD students and post-docs that I have encountered during my stay at GANIL and in the different conferences and seminars. My special thanks to Aldric, Bélen and Sylvain for the practical help.

I wouldn't forget to thank the people at GSI for their useful discussion, especially Valerii PANIN, Thomas AUMANN, Dominic ROSSI and Christoph CAESAR.

Last but not least, I would like to thank my family and friends for supporting me in different ways.

# Table of Content

# List of Figures

# List of Tables

# Introduction



In this introductory chapter, we will first make a quick review of the general description of the atomic nucleus and the phenomena occurring in stable nuclei. Then we will discuss the new phenomena that are specific to nuclei near the neutron dripline and give the motivations that led us to study the structure of $^{12}$Be in particular. The chapter will end with a presentation of the experimental approach to study loosely bound nuclei close to the neutron dripline.

## 1.1 General landscape of the nuclear chart

The general landscape of atomic nuclei is often illustrated by the two-dimensional chart, also called Segré chart (Fig. 1.1), with the y-axis representing the number of protons (Z) in an atomic nucleus and the x-axis the number of neutrons (N). The black squares in the middle of the chart show the region of stable nuclei forming the so-called valley of stability. These stable nuclei contain almost equal number of protons and neutrons for light nuclei, but have more neutrons for heavier nuclei to compensate the increasing Coulomb repulsion induced by the protons. Nuclei off the valley of stability are unstable and undergo radioactive decay. They are represented with different colors corresponding to their decay modes. For example, neutron-rich nuclei will decay via $\beta^-$ by converting neutrons into protons. Similarly, neutron-deficient (or proton-rich) nuclei will decay via $\beta^+$ converting protons into neutrons. The $\beta^-$( $\beta^+$) decay is accompanied by the emission of an electron (positron) and an anti-neutrino (neutrino). Heavier nuclei can emit bound $^4$He nuclei, also called $\alpha$-particle, or fission in smaller pieces.

Our knowledge on the properties of the atomic nucleus are derived from studying nuclei near the valley of stability. Away from this valley of stability, atomic nuclei become more unstable as the imbalance between the number of protons and neutrons becomes bigger. The limits where it is no longer possible to form a bound nucleus by adding neutrons (or protons) to a given one, are called the neutron and proton driplines.

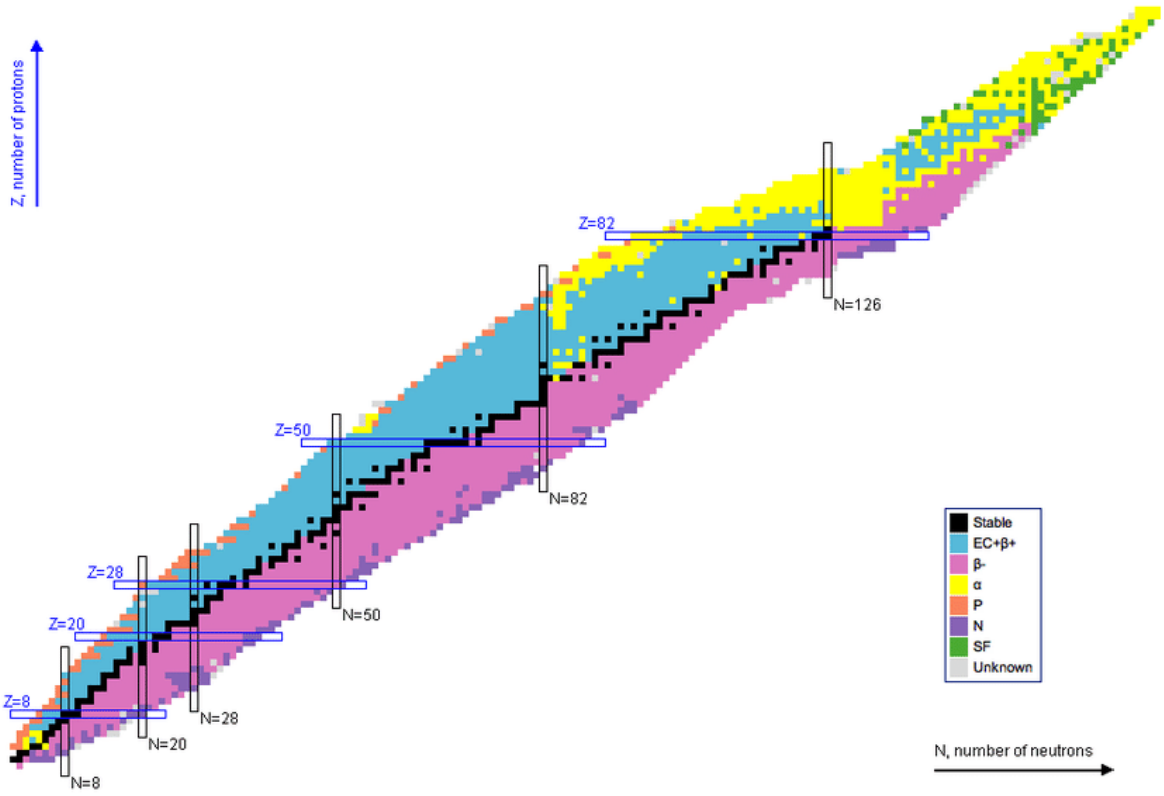


**Figure 1.1** – Chart of atomic nuclei with two axes, the number of protons Z and the other is the number of neutrons N. The black squares represent stable nuclei forming the so-called valley of stability. Squares of other colors represent unstable nuclei and each color represents their decay mode. Image taken from Ref. [1].

Attempts to understand the basic underlying phenomena observed in nuclei led to a variety of theoretical models that can be classified in three main categories:

- Single-particle models that considers the individual degrees of freedom of nucleons.
- Collective models that view the nucleus as a whole.
- Mixed models that consider both individual and collective degrees of freedom.

In the early days of nuclear physics, the liquid-drop model was proposed by Niels Bohr, considering the atomic nucleus as a classic liquid with some quantum corrections. It describes well some properties of nuclei, especially their binding energy [2] and phenomena inherent to nuclear fission [3, 4]. However, this model did not succeed to reproduce all experimental data, for example the observed extra-stability in some regions of the nuclear chart. The shell model of nuclear physics was introduced to explain this phenomenon, among others.

### 1.1.1 The shell-model description of the nucleus

The shell model of nuclear physics introduced by Mayer and Jensen in the 1940's considers the nucleons as single particles moving in a mean field created by other nucleons [5–8]. It was successful in describing nuclei, especially the experimentally observed extra-stability in some of them, by considering the existence of "magic numbers" which is a further indication of a shell structure of nuclei.

The states of the nucleus as a quantum system are governed by the Schrodinger equation [9,10]:

$$H|\psi(r_1, r_2, ..., r_A)\rangle = E|\psi(r_1, r_2, ..., r_A)\rangle \tag{1.1}$$

where, considering only two-body interactions, the Hamiltonian $H$ is defined as:

$$H = \sum_{i=1}^{A} \frac{P_i^2}{2m_i} + \sum_{i<j}^{A} V_2(r_i, r_j) \tag{1.2}$$

with $\frac{P_i^2}{2m_i}$ being the kinetic energy of the $i^{th}$ nucleon and the potential $V_2(r_i, r_j)$ represents the two-body interaction between the $i^{th}$ and $j^{th}$ nucleons.

Eq. 1.2 can be rewritten in such a way that we can separate it in two parts, one that treats the independent motion of the nucleon, $H_{s.p.}$, and another taking into account the residual interaction $V_{res}$:

$$\begin{aligned} H &= [\sum_{i=1}^{A} \frac{P_i^2}{2m_i} + \sum_{i}^{A} V_1(r_i)] + [\sum_{i<j}^{A} V_2(r_i, r_j) - \sum_{i}^{A} V_1(r_i)] \\ &= H_{s.p.} + V_{res} \end{aligned} \tag{1.3}$$

The independent-particle Hamiltonian can be chosen such that it includes the major part of the two-body interaction. Hence, the residual interaction $V_{res}$ is weak and would be treated as a perturbation, or in the best case ignored. It is then crucial to define the potential. Apart from the nuclear mean-field potential, the Coulomb interaction for protons is added to better describe the experimental data. The Harmonic oscillator and square-well potentials are sometimes used as the mean-field nuclear potential, but the commonly used potential is the spherical Woods-Saxon potential [11–15]:

$$V_{WS}(r) = -\frac{V_0}{1 + exp(\frac{r-R}{a})} \tag{1.4}$$

whose parametrization is $V_0$ = 40.5 + 0.13A MeV is the depth of the potential, a = 0.65 fm is surface diffuseness, $R_0 = r_0\ A^{1/3}$ the radius of the spherical nucleus, $r_0$ = 1.27 fm, and A the mass number of nuclei.

The Woods-Saxon potential alone does not fully reproduce the experimentally observed magic numbers, that are a signature of shell closure in nuclei. A spin-orbit term, $V_{LS}$, is

then added, producing a splitting of the orbitals J↑ and J↓, formed by the alignment or anti-alignment of the angular momentum L of the nucleon with its intrinsic spin value S. The nuclear potential is then given by the sum of the two :

$$V_{res} = V_{WS} + V_{LS}$$

The potential is pictured in Fig. 1.2, where we can see that it is deeper for neutrons than for protons due to the Coulomb repulsion term for the latter. On the right-hand side of Fig. 1.2, we see the effect of the spin-orbit term on the potential for the two cases when the spin is opposite or parallel to the orbital momentum.

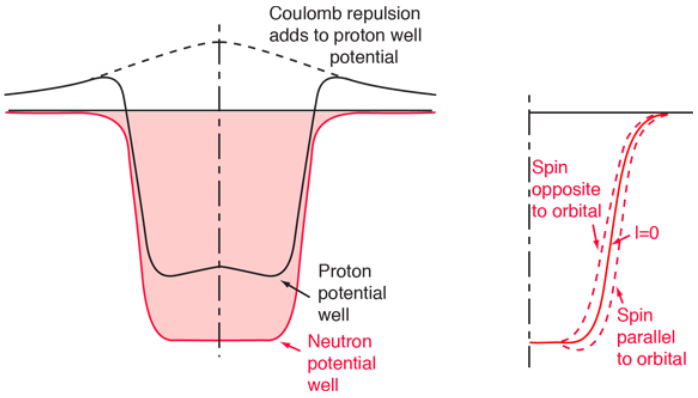


**Figure 1.2** – Left: illustration of the potential felt by the protons and neutrons in the nucleus. Right: the splitting induced by the addition of the spin-orbit term. Taken from [16].

The solutions, $\psi$, of Eq. 1.1 are the products of the individual wave functions $\phi^i_{nljm}$ of each nucleon with energy $E^i_{nlj}$. Since nucleons are fermions, the wave function $\psi$ of the nucleus is antisymmetrized according to the Pauli exclusion principle, through the Slater determinant. The lowest energy solution corresponds to the ground state of the nucleus, and the excited states are obtained from the other possible combinations of orbitals' occupations. The spectrum of individual levels of the mean field is shown in Fig. 1.3. On the left side, the principal orbitals arising from the Wood-Saxon (WS) are shown, then the degenerate individual orbitals obtained after the spin–orbit interaction are labeled by quantum numbers $n$, $l$ and $j$.

The lowest energy orbitals are filled first, and we see that the predicted magic numbers correspond to the full occupancy of an orbital which is well separated in energy from upper orbitals. The energy required to move one nucleon from these closed shells to upper shells is of the order of few MeV or more. Thus, the closed shells may be considered as not participating in the interactions with outer nucleons, forming an inert core. The remaining nucleons occupy the next shells, called valence shells, just above the closed one. It is assumed that the inert core is completely described by the independent-particle approximation of the potential, whereas the residual interactions are included for the valence nucleons.

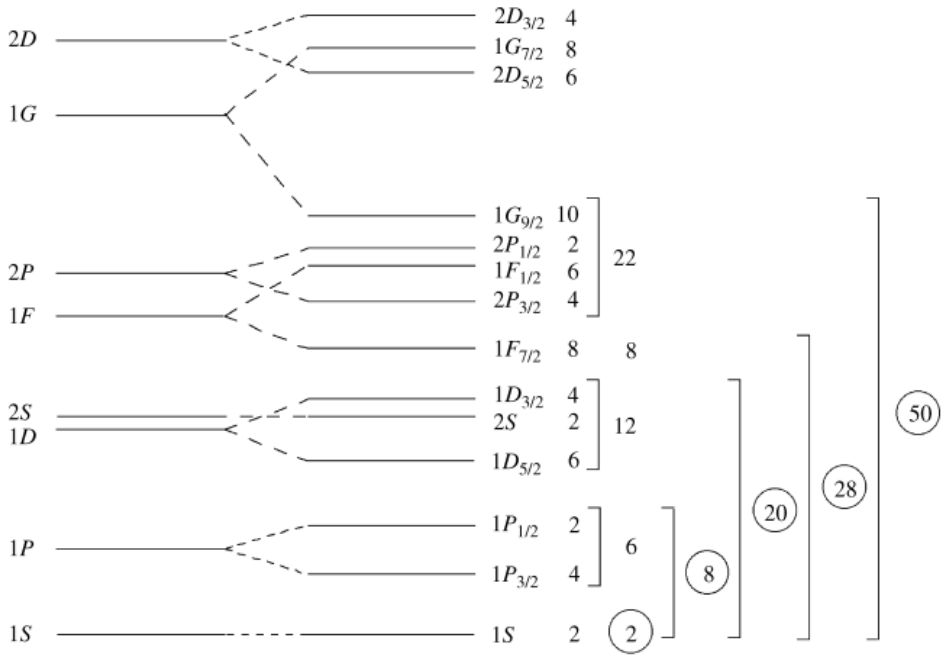


**Figure 1.3** – Low-lying energy levels in a single-particle shell model using the Woods-Saxon potential (the levels on the left side), plus spin-orbit term. Image taken from [17].

The shell model presented here describes well nuclei with or around a closed shell, where the spherical symmetry still holds. However, some features, like rotations and vibrations, observed in nuclei far from closed shells are better described in terms of the collective degrees of freedom of the nucleus. These nuclei are characterised by low-lying excitation with enhanced transition probabilities, suggesting that they are intrinsically deformed.

### 1.1.2 Collective models of nuclei

The collective model of atomic nuclei was first introduced by Bohr and Mottelson [18]. This model, contrary to the shell model that deals with nucleon individual degrees of freedom, treats the nucleus as a whole [19, 20]. In fact, the nucleus under certain conditions, can manifest collective behavior such as the oscillation of its surface around a fixed position (vibration), or rotation if the nucleus is rigidly deformed. The surface of the nucleus is defined through the expression of its radius, R$(\theta, \phi)$, in terms of deformation parameters as :

$$R(\theta,\phi) = R_0(1 + \sum_{\lambda=1}^{\infty} \sum_{\mu=-\lambda}^{\lambda} \alpha_{\lambda,\mu}(t) Y_{\lambda,\mu}(\theta,\phi)) \tag{1.5}$$

The parameter $\lambda$ determines the degree of deformation: $\lambda$ = 0, 2, 3, etc, corresponding to the spherical (non-deformed), quadrupole and octupole deformation, respectively (Fig. 1.4).

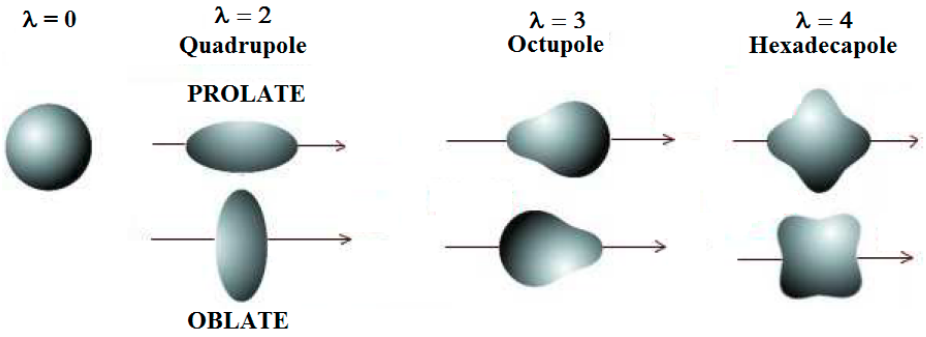


**Figure 1.4** – Different shapes of nuclei, from a non-deformed spherical ($\lambda = 0$) to quadrupole ($\lambda = 2$), octupole ($\lambda = 3$), etc. Image taken from [21].

### Vibration

The surface of the nucleus can vibrate around its spherical equilibrium ($\lambda = 0$). The vibrational excitations of the nucleus are described in terms of phonons. Above the $0^+$ ground state, the first excited state of an even-even vibrational nucleus is a $2^+$ and has an energy that equals the energy of a phonon $E_{ph}$, followed by 3 degenerate states $0^+$, $2^+$, $4^+$ at an energy of $2\times E_{ph}$. In Fig. 1.5, the first vibrational states of an even-even nucleus are shown on the left-hand side.

The transition probabilities from an initial state with $N_{ph}$ phonons to a given final state $N_{ph}$-1 phonons are given by :

$$B(E2, J_i^\pi(N_{ph}) \rightarrow J_f^\pi(N_{ph}-1)) = N_{ph} \times B(E2, 2^+ \rightarrow 0^+) \tag{1.6}$$

For example,

$$B(E2, 4^+ \rightarrow 2^+) = 2 \times B(E2, 2^+ \rightarrow 0^+) \tag{1.7}$$

In reality these equations are only approximations as the vibrational motion mixes with other collective degrees of freedom of the nucleus.

### Rotation

A deformed nucleus can rotate and its kinetic energy, similarly to the rotational bands of diatomic molecules, is given by the expression:

$$E_k = \frac{I\omega^2}{2} = \frac{L^2}{2I} \tag{1.8}$$

where $I$ is the moment of inertia of the nucleus as a rotating system and $L = I\omega$ is its angular momentum. The quantum expression of this energy is straightforward, taking the eigen-values of $L^2$, $\ell(\ell+1)\hbar^2$:

$$E_\ell = \frac{\hbar^2}{2I}\ell(\ell+1) \tag{1.9}$$

The transition probabilities in this case are given by [11]:

$$B(E2, 4^+ \rightarrow 2^+) = 1.4 \times B(E2, 2^+ \rightarrow 0^+) \tag{1.10}$$

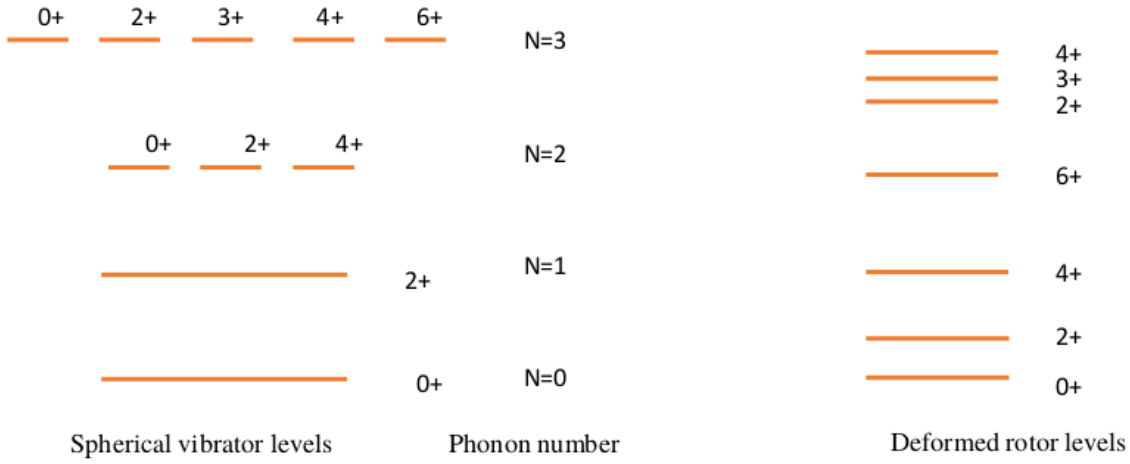


**Figure 1.5** – Vibrational and rotational low-lying states in an even-even nucleus. Image taken from [22].

Though, the moment of inertia required to account for the energy of rotational states is about three times lower than that of a rigid body with the same shape [11]. The current interpretation of this observation is based essentially on the fact that the nucleons form Cooper pairs, that gives a superfluid behavior to the nucleus.

### 1.1.3 Nuclear superfluidity and pairing

The majority of nuclei exhibit a superfluid behavior, that is experimentally seen in the phenomena such as the back-bending effect [25]. Superfluidity is the macroscopic manifestation of the pairing of nucleons. It was initially believed that, in collective models, the nucleus vibrates and rotates around the spherical or deformed shape equilibrium as an irrotational liquid drop. In this model, the internal degrees of freedom of the nucleus are suppressed and the nucleus is regarded as a homogeneous fluid characterized only by a set of shape coordinates. However, the observed quenching of the moment of inertia in deformed nuclei suggested the existence of a rotational phase of the nucleus. Hence, the nucleus would comprise two phases, of which the superfluid one corresponds to the maximum pairing and therefore to the absence of rotation. In Fig. 1.6 the experimental moment of inertia is plotted together with the moment of inertia calculated for a rigid body, we see that the experimental one is lower, i.e. it is quenched.

This model then predicts a sudden increase in rotational inertia when a pair is broken and therefore gives a critical value of $\ell$ at which the pairing correlations vanish:

$$\frac{\hbar^2}{2I}\ell(\ell+1) > \frac{\hbar^2}{2I_{rig}}\ell(\ell+1) + 2\Delta \tag{1.11}$$

where $\Delta$ is the pairing gap, $I_{rig}$ is the moment of inertia of a rigid body of the same dimension as the nucleus and $I \sim I_{rig}/3$ is its expected moment of inertia if all the nucleons were paired. The transition from superfluid to normal fluid phase produces the backbending effect. This phase transition is attributed to the Coriolis force, acting as an anti-pairing force for the nucleons. We emphasise that this model is an approximation as several pairs should usually be broken before reaching $I_{rig}$.

The existence of pairing correlations in nuclei was first suggested by Bohr, Mottelson and Pines [23] by analogy between the gap in the excitation spectra of superconducting metals and the gap in the excitation spectra of even-even nuclei. The theory of Bardeen–Cooper–Schrieffer (BCS) explains the mechanism by which a superfluid phase is formed. Pairing correlations justify the fact that the ground state of all even-even nuclei is of $0^+$ configuration [24]. And as shown previously, the superfluid behavior of the nuclei is understood by considering the pairing of nucleons.

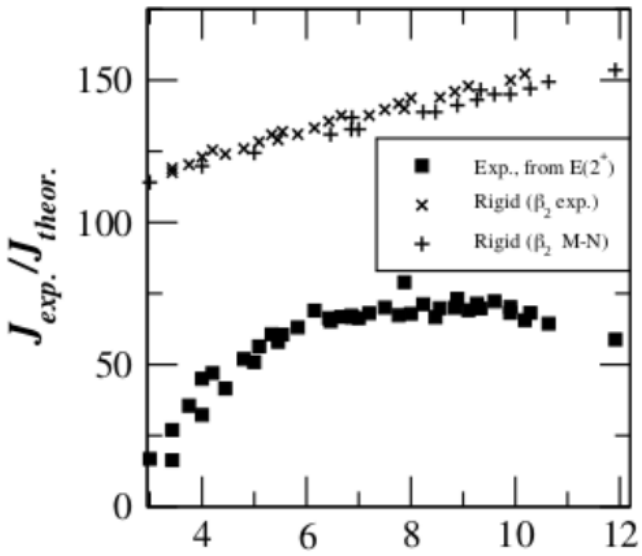


**Figure 1.6** – Moment of inertia for a rigid nucleus (black crosses) and for the rotational $2_1^+$ state (filled black squares). Image taken from [32].

However, questions rise on whether this approximation still holds for nuclei at the neutron dripline. In fact, the Fermi surface in these nuclei is close to the continuum, in such a way that the neutron separation energy is of the same order as the pairing gaps. Hence, the Cooper pairs are scattered in the continuum, leading to a diffuse gas of unbound neutrons surrounding the nucleus. Consequently, it is interesting to investigate if pairing regime is still in the BCS approximation there.

## 1.2 New phenomena at the neutron dripline

Far from stability, as the balance between protons and neutrons shifts, previous magic numbers can be replaced with new ones [33]. The binding energy also falls rapidly towards this region, leading to spatially increased neutron density as compared to that of protons and to new phenomena at the drip-line: neutron halo nuclei, clusters, quasi-molecular states, etc. (Fig. 1.7).

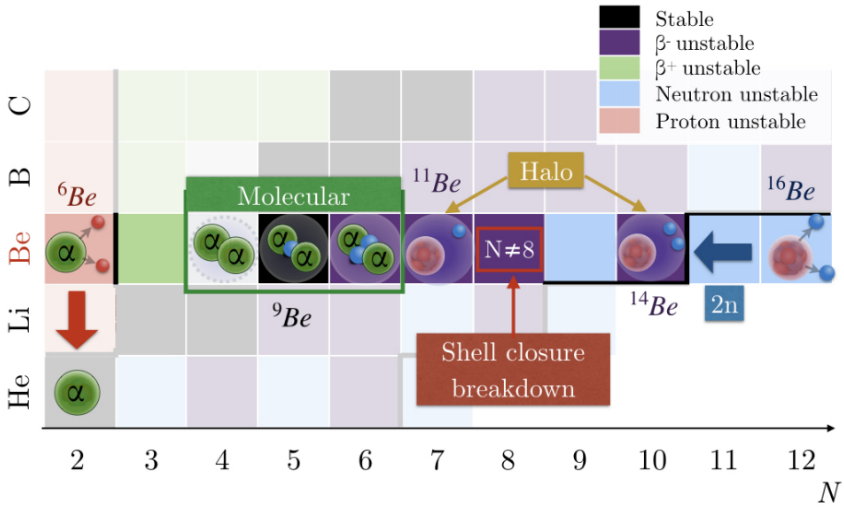


**Figure 1.7** – Illustration of some new phenomena happening in nuclei (Be isotopes) close to the dripline, from molecular-like ($^{8-10}$Be) to halo ($^{11}$Be and $^{14}$Be) nuclei. Image taken from Ref. [133].

### 1.2.1 Nuclear superfluidity at the dripline

It is interesting to look at the pairing regime in the neutron-rich nuclei near the dripline [34–37], where the binding energy is reduced and where low-density distributions of neutrons are found, i.e. formation of a neutron skin or halo surrounding the nuclear surface [47–49]. Therefore, one may want to know how the pair correlation in these exotic nuclei is different from that in stable nuclei, evidencing the effect of density dependence. Or in other words, how the mean size of a pair of nucleons at low nucleon density differs from that around the normal density?

The existence of spatially correlated Cooper pairs of neutrons called "dineutrons" was theoretically suggested in Refs. [34, 38–42] and experimentally discussed in Refs. [43–46]. It was then suggested the existence of a crossover from a superfluid system of BCS-type to a Bose-Einstein condensate of spatially compact bound Fermion pairs [47, 48, 50–52]. Fig. 1.8 illustrates the possible spatial correlations of two neutrons for a stable nucleus and a nucleus close to the dripline, where there is formation of halo or skin of neutrons.

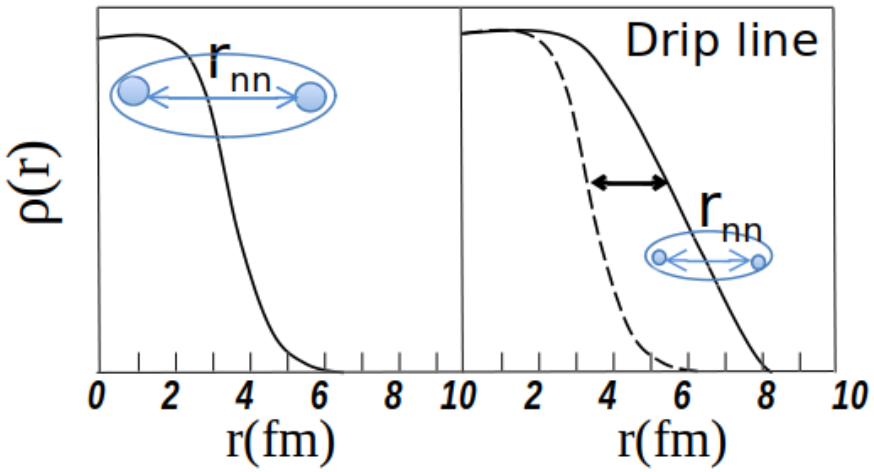


**Figure 1.8** – Nuclear density as a function of the radius of the nucleus. Left: neutrons form BCS-like pairs in stable nuclei. Right: at the dripline, the pair regime becomes closer to a BEC-like.

In this work, we will study the nuclear structure of $^{12}$Be and find a mean to study neutron-pair correlations of its 2n-unbound states through the observation of their decay. In order to understand the choice of this nucleus, let us first look at its structure in comparison with its isotones.

### 1.2.2 Isotonic chain N=8

In this section we will compare the shell structure evolution of N=8 isotones. The known magic number N = 8 corresponds to the filling of the 1*s* and 1*p* orbitals. Hence, the value of the gap that is formed between the occupied $1p_{1/2}$ and the valence $1d_{5/2}$ and $2s_{1/2}$ orbits determines whether N=8 is a magic number or not. Fig. 1.9 left shows the binding energies of the corresponding states for different Z (number of protons) value. The gap energy is comparable but slightly bigger for $^{16}$O (Z=8) than $^{14}$C (Z=6), of 7 MeV and 6 MeV respectively [55].

Another measure of the evolution of the N=8 gap is the energy of the negative parity states formed by exciting one neutron from the $1p_{1/2}$ orbital to $2s_{1/2}$ or $1d_{5/2}$ ones. As for excitations to the former, the states are $0^-$ and $1^-$ while we have $2^-$ and $3^-$ for excitations to the latter. The energies of the $1^-$ state are shown in Fig. 1.9 right for three N=8 isotones, $^{12}$Be, $^{14}$C and $^{16}$O, and one can compare them with the value of the N=8 gap obtained independently in Ref. [55]. We see a drastic drop of E($1^-$) in $^{12}$Be (Ref. [68]), which was historically one of the first indication of the disappearance of N=8 magic number in this nucleus.

A. Barrière [56] studied the N=8 shell gap in $^{13}$B by determining the proportion of the *sd*-intruder orbitals in the ground state of $^{13}$B. Using one-neutron knockout reaction from a high-energy beam of $^{13}$B, he compared the population rates of normal (positive parity) and intruder (negative parity) states in $^{12}$B. The results show a contribution of 11.7(16) % of the intruder sd-orbitals to the ground state of $^{13}$B. Such a small fraction of intruder states, which is comparable to that in the $^{16}$O and $^{14}$C isotones, confirms the N=8 shell closure in $^{13}$B.

The breaking of the N=8 magic number was also observed in Ref. [57] where, performing one-neutron knockout on $^{12}$Be, they observed 75% of the $2s_{1/2}$ and $1d_{5/2}$ strength in the ground state, instead of $1p_{1/2}$ if the shell was closed. This shell filling inversion, together with the partial occupancy of the weakly-bound $2s_{1/2}$ orbital, explains the halo configurations of

the $^{11}$Be and $^{14}$Be nuclei in the vicinity of N=8. In the following, we will focus on the Be isotopes.

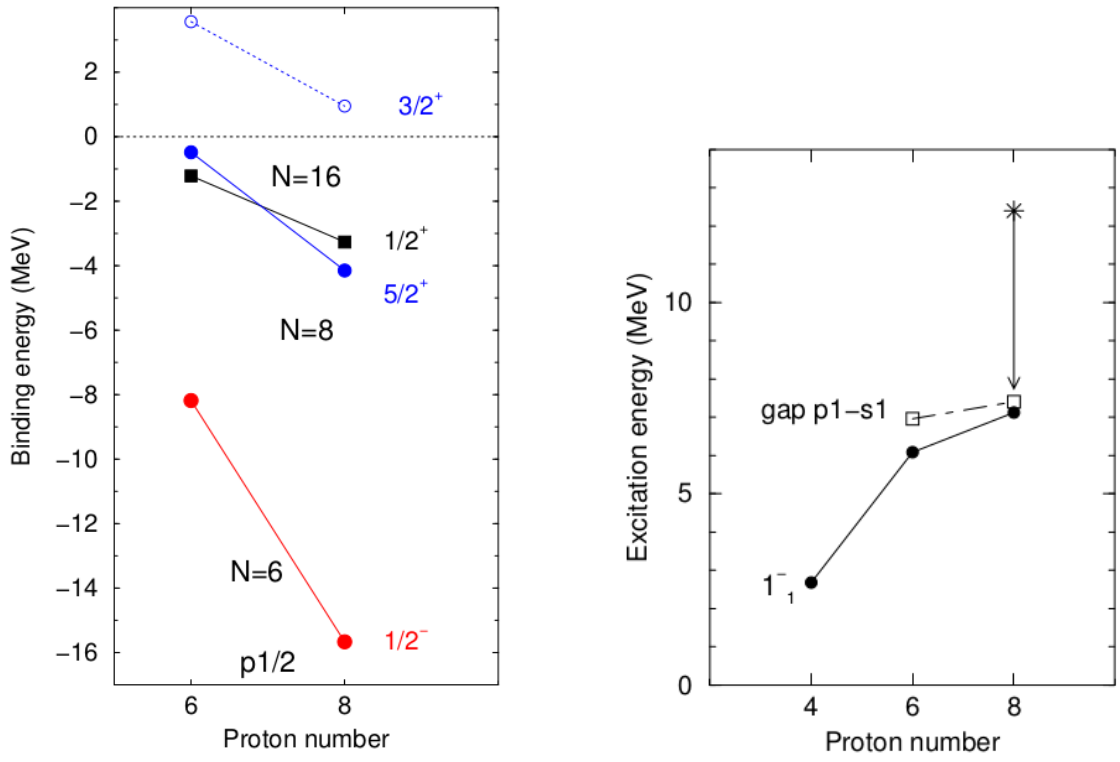


**Figure 1.9** – Left: Binding energies of states corresponding to the $1p_{1/2}$, $1d_{5/2}$ and $2s_{1/2}$ shells for N=8 isotones. Right: Energy of the $1^-$ states for three N=8 isotones, $^{12}$Be, $^{14}$C and $^{16}$O, is compared to the gap energy (empty squares). From Ref. [55].

### 1.2.3 Beryllium isotopes

Beryllium isotopes are particularly interesting as they exhibit a wide range of shapes and structures. With a small number of protons, Z = 4, the evolution of the isotopic chain of Beryllium can be experimentally assessed from the proton to the neutron driplines (Fig. 1.7). They exhibit different and interesting features that we are going to present briefly.

The light $^8$Be is a typical example of $\alpha$-cluster nucleus. The study of the $\gamma$-decay from the $4^+$ state to the $2^+$ state in $^8$Be led to the determination of the B(E2) of $25\pm8$ e$^2$fm$^4$, which was translated as a proof of both $\alpha$-clustering and collective behavior in $^8$Be [58]. Analyzing the moment of inertia of $^9$Be in comparison with that of $^8$Be, it was seen that both have the same core, namely the $\alpha$-$\alpha$ core. This molecular structure was also seen in the rotational bands of $^9$Be [59]. Measurements of the decay correlations of $^7$Be and $^6$Li nuclei following the interaction with a $^9$Be target evidenced the molecular structure of the ground-state of $^9$Be [60].

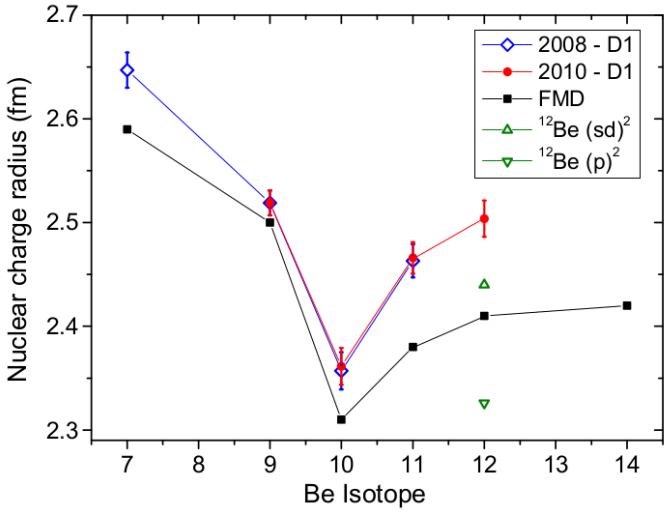


**Figure 1.10** – Experimental charge radii of Be isotopes from isotope-shift measurements. Taken from [61].

However, in $^{10}$Be the molecular structure only shows up in highly excited states, close to the $\alpha$- and neutron-decay thresholds [59]. The ground state of $^{10}$Be is only weakly clusterized, contrary to the other Be-isotopes. The systematic change of cluster structures along the Be-isotope chain is reflected in the N dependence of charge radii, which have been precisely determined by isotope shift measurements in Refs. [61, 62]. The charge radius is the smallest at N=6 (Fig. 1.10) for $^{10}$Be, indicating the disappearance of the N=8 magic number. This trend is well described by the weakening and enhancement of the cluster structures in AMD calculations [63]. The nuclear charge radius, shown in Fig. 1.10 decreases from $^{7}$Be to $^{10}$Be, but then increases for $^{11}$Be. The increase from $^{10}$Be to $^{11}$Be was attributed to the motion of the $^{10}$Be core relative to the center of mass. A mean (rms) distance of 7.0 fm between the neutron and the center of mass of $^{11}$Be was extracted [62], confirming its halo structure. Another example of a halo nucleus is the last bound isotope of the isotopic chain, the Borromean $^{14}$Be with N = 10. In this case, the system is described as a two-neutron halo with a $^{12}$Be core [64–66], for which the subsystem $^{12}$Be+n is neutron unbound.

As a result of the vanishing of the N=8 magic number, the ground states of $^{11}$Be and $^{12}$Be have molecular structures characterized by intruder configurations with enhanced clustering. This was corroborated by experimental observations such as Gamow-Teller and E2 transitions, in Refs. [67–71].

### Motivation for the study of $^{12}$Be

In the Be-isotopic chain, $^{12}$Be is a key isotope to study many features that occur at the neutron dripline. In fact, it is located at the crossroad of nuclei with different structures, from the $\alpha$-cluster $^{8}$Be, to the doubly-magic $^{14}$C, as well as the one-neutron halo $^{11}$Be and two-neutrons halo $^{11}$Li and $^{14}$Be. One would then expect that these configurations can be found at various excitation energies in $^{12}$Be.

Bound states of $^{12}$Be were thoroughly studied using various experimental techniques, which can be summarized as follow:

- The charge radius [61], one-neutron knockout reaction [57,72], transfer reaction $^{11}$Be(d, p)$^{12}$Be [74–76], two-neutron stripping reaction $^{10}$Be(t, p)$^{12}$Be [77] and the charge exchange reaction $^{12}$B($^{7}$Li, $^{7}$Be)$^{12}$Be indicated that the ground state of $^{12}$Be was dominated by the neutron *sd*-intruder configuration and that the N=8 magic number was broken in $^{12}$Be.

- Excited bound states that were identified below the neutron separation energy ($S_n$=3170 keV) are the $2^+_1$ at 2.109(1) MeV [67,77,78], the isomeric state $0^+_2$ at 2.251(1) MeV [170] and the negative parity $1^-$ state at 2.715(15) MeV [68]. The transition probabilities, B(E2, $2^+_1 \rightarrow 0^+_1$) and B(E2, $2^+_1 \rightarrow 0^+_2$) indicate a larger overlap between the $2^+_1$ and $0^+_1$ states rather than between the two $0^+$ states.

A theoretical calculation [63] suggests that the $0^+_1$ and $2^+_1$ states have a 2$\alpha$-core and two neutrons in the *sd*-indruter orbitals, which leads to a prolate deformation. On the contrary, the $0^+_2$ and $2^+_2$ form a band dominated by the *p* orbital ($0\hbar\omega$). Fortune [79] suggested that the observed resonance at 1.243(31) MeV by Smith *et al*. [95] is the most likely candidate for the spherical $2^+$ state. However, there is a disagreement on the parity and decay mode of this state between the two works. While Smith *et al*. suggested a $2^-$ state decaying mainly to the ground state of $^{11}$Be, Fortune proposed that it is a $2^+$ state that would then decay mainly to the excited (spherical non-halo) $1/2^-$ state of $^{11}$Be. Checking the decay on excited state of $^{11}$Be requires a $\gamma$-ray detection, which was not available in the experiment by Smith *et al*.

This controversy, together with the interest in studying the structure of the resonant states of $^{12}$Be above the 2n-emission threshold, rise the need of studying this nucleus with all the tools to allow a better understanding of its structure. If we can populate the two-neutron unbound states of $^{12}$Be, we can then investigate the pairing regime as a function of excitation energy. This may tell us how the superfluidity evolves in this exotic nucleus.

## 1.3 Experimental approach

The experimental tools for studying the nucleus, especially the ones far from stability, have evolved in recent years [80]. The development of high-energy radioactive beams from the fragmentation of heavy ions was crucial to the field and allowed the use of nuclear reactions as a tool for studying unstable nuclei. This method was used in Refs. [81,82] to estimate the radii of exotic nuclei from interaction cross-section measurements. The knockout reaction was used for the first time in Ref. [83] to study spectroscopy of unbound nuclei. Since then, this method is commonly used in investigating the nuclear structure far from stability.

### 1.3.1 Knockout reactions

Knockout reactions have been used to probe the wave function of exotic nuclei. Following Ref. [84], by considering a projectile at high energy approaching a target at rest, they will interact if close enough. The nature of the projectile-target interaction can be nuclear (light target) or Coulomb (heavy target) in its origin. For large impact parameters, the reaction would be peripheral, and would result in the dissociation or breakup of the projectile into one (or a few) nucleon(s) and a core-fragment that would continue its path almost unaffected by the reaction, with almost the same energy as the projectile. The superposition of different removed-nucleon + core-fragment configurations resulting after breakup creates a realistic picture of the original exotic projectile wave function. Therefore, the projectile's wave

function can be factorized as:

$$|Projecticle\rangle \sim \sum C^2S(|Core\rangle \bigotimes |nucleon\rangle) \tag{1.12}$$

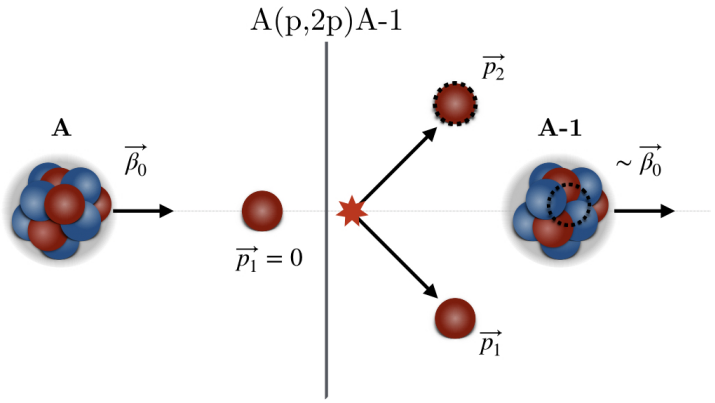


**Figure 1.11** – Illustration of the knockout reaction with an example of the 1p removal, A(p,2p)A-1, reaction. Taken from [133].

As compared to other reactions, such as transfer reactions, at high energy, this knockout reaction is quite favoured, giving rise to relatively large ($\sim$ 100 mb for loosely bound nuclei) cross-sections [84]. Below we will give some general properties of knockout reactions, and details can be found in Refs. [85–87]. In this picture, the incoming projectile interacts with the target at high energy (Fig. 1.11). The reaction products are detected at forward angles.

Knockout reactions are mainly of two kinds:

- "Stripping" or inelastic breakup, in which case the removed nucleon reacts with and excites the target, and the nucleon is scattered to large angles.
- "Diffraction" or elastic breakup, corresponds to reactions where the target remains in its ground state and the removed nucleon is emitted in forward direction, almost at the projectile's velocity.

There could be a third contribution, called Coulomb dissociation, which is the electromagnetic elastic breakup. But this contribution plays a minor role in the case of light targets and can be neglected.

The single particle cross-section, $\sigma_{sp}$, of the process can be expressed as:

$$\sigma_{sp} = \sigma_{str} + \sigma_{dif} \tag{1.13}$$

where the stripping $\sigma_{str}$ and diffraction $\sigma_{dif}$ contributions are often calculated assuming that the projectile constituents follow a straight line with constant velocity. This approximation is called the eikonal or Glauber theory [87]. A more accurate picture of these single-particle cross-sections is provided by the "spectator-core" approximation to the many-body eikonal

theory.

Given the low neutron separation energy for nuclei close to the dripline, the knockout reactions will populate unbound states of these nuclei forming resonances in the continuum, which then decay by emitting the extra neutron(s). We then need to detect all reactions products after knockout in order to determine the physical observables of interest.

### 1.3.2 Decay of unbound states

Unbound states lie above the neutron (or proton) emission threshold. Close to the dripline the nucleon emission threshold is low, favoring the formation of unbound states at relatively low excitation energy. In this thesis, we are mostly interested by the $^{12}$Be nucleus which is significantly less bound than nuclei in the valley of stability. Above the 1n- and 2n-emission threshold ( $S_n$ = 3170 keV and $S_{2n}$ = 3670 keV), in the continuum, we find 2-body and 3-body unbound systems that decay by emitting 1n or 2n, respectively.

As it was shown in Ref. [115], describing neutron unbound states in the continuum comes down to describing resonant scattering of a neutron with a wave function $\phi_n = exp(ikz)$ on the potential of the core nucleus. The potential has two components, the attractive nuclear potential and the repulsive centrifugal potential due to the orbital momentum $\ell$:

$$V_{eff} = V_N + \frac{\hbar^2 \ell(\ell+1)}{2\mu r^2} \tag{1.14}$$

Where r is the fragment-neutron distance and $\mu$ the reduced mass of the system neutron plus core-fragment. This schematic representation shows that the neutron may be trapped in the $\ell$-dependent potential. The larger $\ell$ is, the higher the potential and the longer the neutron will remain trapped in the potential forming a resonant state. The time required for the neutron to overcome the potential can be expressed as the lifetime $\tau$ of the neutron-fragment resonance and is linked to its width $\Gamma$ by the Heisenberg uncertainty principle:

$$\Gamma \times \tau \sim \frac{\hbar}{2} \tag{1.15}$$

The resonant state will then have a width in energy and its shape is seen through the expression of the cross-section, which is obtained by integrating the scattered wave function:

$$\sigma(E) \sim \frac{\Gamma_\ell^2(E)}{(E - E_r) + \frac{1}{4}\Gamma_\ell^2(E)} \tag{1.16}$$

where the width $\Gamma_\ell(E)$ depends on the orbital momentum of the neutron $\ell$. The expression above is known as the Breit-Wigner formula and gives the line shapes for the resonances that can be seen in the inserts of Fig. 1.12.

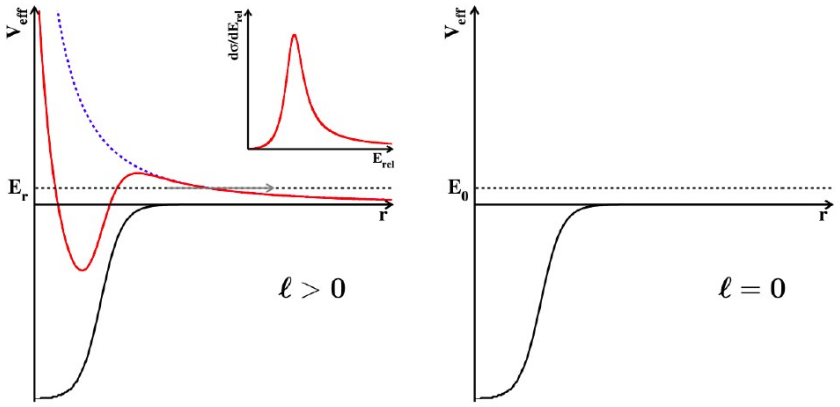


**Figure 1.12** – Left: the potential felt by a neutron inside the nucleus for $\ell$>0 is the sum (red line) of the centrifugal (dashed blue line) and nuclear (plain black line) potentials. Right: the nuclear potential felt when $\ell$=0 (no centrifugal barrier). The $\ell$-dependent Breit-Wigner function in the insert shows the line shape of the resonance. Taken from [91].

The Breit-Wigner function is then used in a fitting procedure to compare to the experimental data. It has four parameters : angular momentum $\ell$, intrinsic width $\Gamma$, centroid energy $E_r$ and the amplitude A. This description of the decay of unbound states will be continued in Sect. 3.4 while analysing the experimental data.

# Experimental Setup



In this chapter I will describe the experiment s393 performed at GSI on which the current work is based. In this experiment, the R3B-LAND setup was used. The apparatus is presented from the production and selection of the radioactive ion beam to the setup used for the detection of the reaction products. In the last section of this chapter, I describe the calibration procedure for the different detectors.

## 2.1 Beam production and selection

In the s393 campaign performed at GSI, in Darmstadt Germany, the radioactive ion beam (RIB) was produced in fragmentation reaction, and was subsequently selected and transmitted through a magnetic spectrometer. This radioactive beam production is briefly explained in the following paragraph. A bird-eye view of the GSI facility is shown in Fig. 2.1.

The mechanism of production of the RIB begins by extracting a stable primary beam from the ion source. At GSI, the primary beam is injected into the "UNIversal Linear ACcelerator" (UNILAC) for a first acceleration. For the s393 experiment, $^{40}$Ar ions were used as primary beam and were accelerated in the UNILAC to reach an energy of about 11.5 MeV/nucleon. From the UNILAC the $^{40}Ar^{11+}$ is injected into the "Schwer Ionen Synchrotron-18" (SIS-18) for further acceleration. At the exit of the SIS-18, the $^{40}$Ar ions have been accelerated to an energy of 490 MeV/nucleon and have an intensity of $6 \times 10^{10}$ ions/bunch. The primary beam is then guided onto the production target at the entrance of the FRagment Separator (FRS) (see Fig. 2.1). A 4 g/cm$^2$ thick $^9$Be production target was used to induce the fragmentation reactions. A large variety of elements with masses smaller than or around the one of $^{40}$Ar is produced, leading to a cocktail of radioactive secondary beams with an energy of about 430 MeV/nucleon.

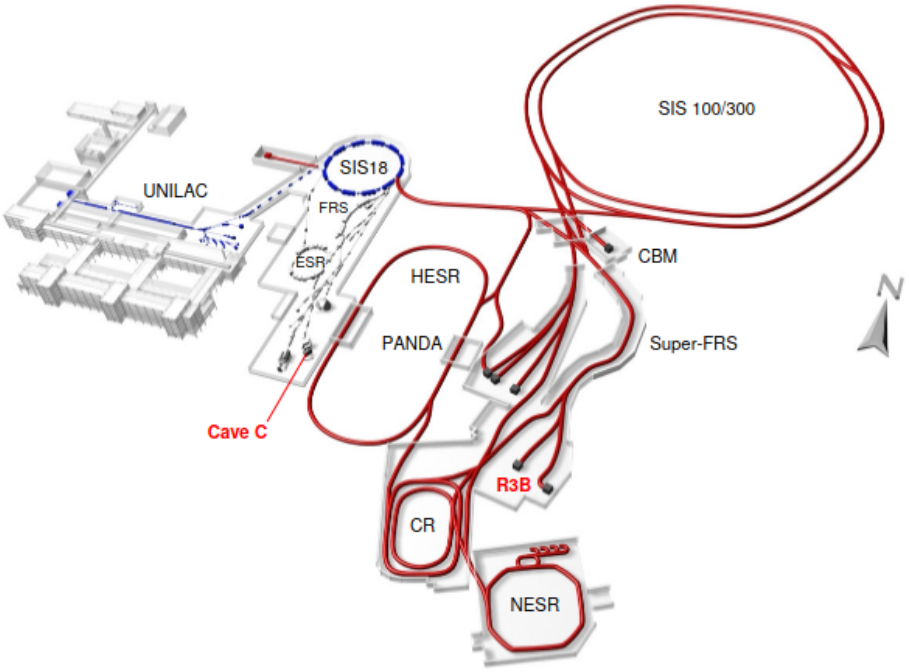


**Figure 2.1** – Sketch of the GSI facility. The area in which this experiment was located (left, blue) is shown together with the current FAIR facility (right, red). Taken from Ref. [100].

The radioactive beam of interest is then selected by means of the B$\rho$ method (Fig. 2.2) which is applied in the FRS prior to be transmitted to the R3B-LAND experimental setup located in Cave C. The secondary beam of choice is delivered to the cave by tuning the FRS settings. For our experiment we are interested in the $^{13}$B secondary beam. Therefore, the magnetic rigidity B$\rho$ of the FRS is set in such a way that only nuclei with $A/Z \sim 2.6$ are transmitted.

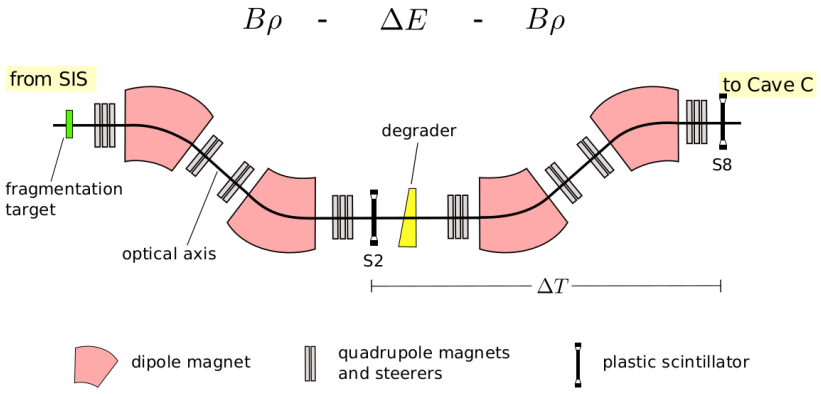


**Figure 2.2** – Illustration of the Fragment separator FRS. Dipoles are used to bend and select the beam following the B$\rho$-$\Delta$E-B$\rho$ method. A degrader is added as well in order to have a position and Z-dependent energy loss ($\Delta$E). Image taken from Ref. [93].

The FRS beam line was equipped with two scintillator paddles of 3 mm thick each. One scintillator paddle was placed at the middle focus (S2) and the other one downstream the FRS (S8). The one at the intermediate focal plane (S8), nearly 55 m upstream of the reaction target, was used for time of flight measurement. The scintillator S2 was not used because it was overloaded with the intense beam.

### 2.1.1 POS and ROLU detectors

The plastic scintillator detector POS is used as a starting reference for the measurements of the time of flight and serves as a trigger for the incoming beam. It is located at a distance of about 2 m before the target, between two Position Sensitive Pin diode (PSP1 and PSP2) used to identify the incoming beam. We can see in Fig. 2.3 the design of the detector. The active area of POS is constituted by a 5×5 $cm^2$ plastic scintillator with a thickness of approximately 200 $\mu$m. When a charged particle hits the scintillator, it produces light which is collected by four photomultiplier tubes (PMTs) attached to either side of the scintillator. The integrated charge and arrival time of a signal in every PMT are recorded and used to determine energy loss, time and position of a particle hit in the scintillator [100].

The Rechts-Oben-Links-Unten (ROLU) detector is used to define the spot size of the beam. It consists of four movable scintillator paddles each with an area of 9.5×10 $cm^2$, a thickness of 5 mm, and readout by a PMT. The paddles are arranged around the beam in a way that only a small rectangle in the middle is not covered by them. Only particles traversing through the empty spot are accepted. All particles which hit at least one scintillator paddle of ROLU produce a signal used as a veto for recording and are ruled out. By moving the paddles mounted on drives, the size of the accepted beam can be varied. It is usually chosen in a way that all accepted particles hit the target.

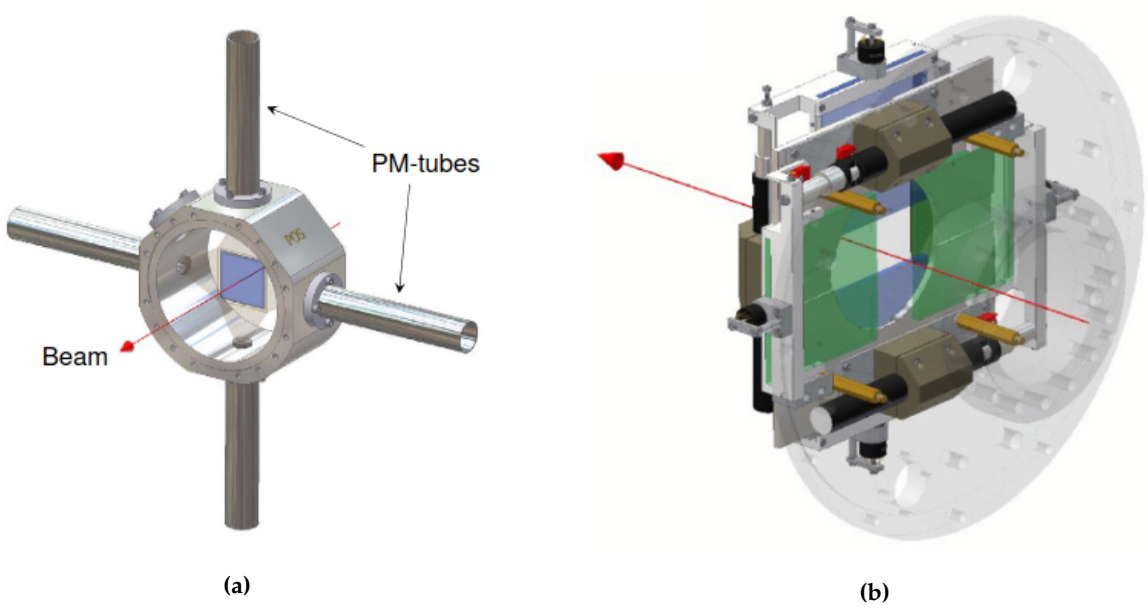


(a) (b)

**Figure 2.3** – (a): The plastic-scintillator detector POS provides time measurements and a trigger for the incoming beam. A light signal created by the penetrating ions, in the scintillator (blue) is read out by four PMT. (b): The ROLU detector consists of plates of two scintillators each moving in the x (green) and y (blue) directions. An accepted ion ("Good Beam", indicated by the red arrow) is the one that did not interact. Taken from Ref. [100].

## 2.2 Reaction targets

For the purpose of the present research a hydrogen target was required. From a practical point of view a $CH_2$ target is preferable, because it is more compact than a pure hydrogen target (gas or liquid) and is easier to handle. Neglecting the carbon component, the $CH_2$ can be considered as a hydrogen (or proton) gas confined in the volume of the target sample,

where the reaction can occur. However, the carbon component also contributes to the total reaction yield and causes an additional straggling of the beam. In order to estimate this background, complementary measurements with a pure carbon target were conducted. Then, two different reaction targets were used during the experiment: a 922 mg/cm$^2$ $CH_2$ target and a 935 mg/cm$^2$ C target. During the experiment, those two targets were mounted on a remote-controlled target wheel so they could be changed in vacuum without beam interruptions.

While going through the reaction target, the incoming ion has a probability to react with a nucleus from the target. In our experiment, we are looking for knockout reactions from which bound and unbound states can be populated. These unbound states are decaying with the emission of one or several neutrons. We are therefore left with neutron(s), a charged fragment and possible $\gamma$-rays if excited states of the fragment are populated. In order to characterize all the states, bound and unbound, we need to be able to identify and characterize all those reaction products. We briefly specify the technique used to detect them in the following section.

## 2.3 Detection of reaction products

The Crystal Ball calorimeter around the target (Fig. 2.6) was placed to measure $\gamma$-rays and protons emerging in quasi-free-scattering (QFS) reactions. In order to obtain angular information about reaction products, the target area was additionally equipped with an array of six double-sided Silicon microStrip Detectors (SSDs). The forward moving fragments were deflected by the ALADIN magnet and were further measured in the corresponding detection systems. The neutrons were detected by the Large Area Neutron Detector (LAND), the heavy fragments were tracked via two scintillating fiber detectors GFIs and a time of flight wall (TFW). In the following I will give a detailed description of each detection system.

### 2.3.1 Double-sided Silicon microStrip Detectors

The type of reactions intended for the present study imposes a set of requirements on the design of the tracking detectors located in the vicinity of the target. Firstly, due to a strong kinematical focusing of the reaction fragments in the forward direction, the trackers are expected to have a high granularity in order to obtain a reasonable position resolution. Secondly, a wide dynamic energy range of the detectors is important for the identification of various nuclear species. Moreover, the detectors need to have a low noise level and multihit capability. All these requirements are met by the AMS-type [104] SSDs. They have been specially developed for tracking high-energy cosmic rays (from protons to iron) as an essential part of the Alpha Magnetic Spectrometer (AMS) [105] operating on board of the International Space Station (ISS).

The detection principle in the SSDs is based on the creation of electron-hole pairs along the particle trajectory in the depleted semiconducting silicon volume. Due to the presence of an electric field in the volume, the created charges drift towards the nearest strip sensors, which cover the silicon bulk from two sides, orthogonally to each other. Thus, an accurate position of the hit on a plane and the energy loss (i.e. charge) of the particle can be measured. An implantation pitch on the junction side (p- or S-side) is 27.5 $\mu$m with the corresponding readout pitch of 110 $\mu$m, i.e. only each fourth strip is read out while others are left floating. The charge collection in the floating strips is achieved through capacitive couplings between the strips which provides a position resolution with the readout pitch larger than the implant pitch. On the ohmic (n- or K-side) the implant pitch is 104 $\mu$m with every strip being read out. It has been demonstrated in Ref. [104] that the position resolution of about 10 $\mu$m can be achieved with up to 200 $\mu$m readout pitch, that corresponds to roughly 1 mrad of angular

resolution in the present experimental geometry.

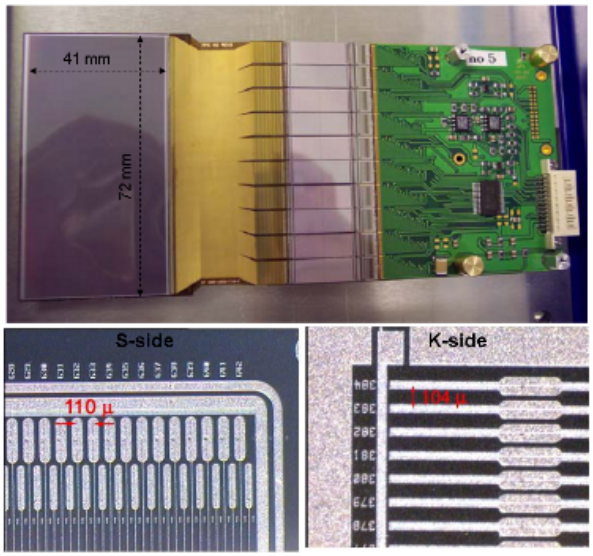


**Figure 2.4** – A design of the AMS-type silicon microstrip detector. The double-sided 0.3 mm thick silicon sensor has the dimension 72×41 mm$^2$. The number of readout channels is 640 on the long S-side and 384 on the short K-side. The attached front-end electronics board (green) is used to read out signals from the strips. Taken from Ref. [100].

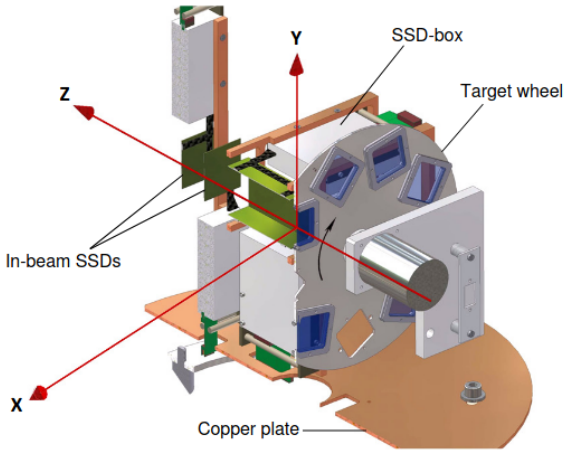


**Figure 2.5** – The cross-section view of the installation inside the target chamber. Six silicon trackers (green) together with the target-wheel (blue) are fixed on a copper plate. The laboratory coordinate system is shown in red. The Z axis coincides with the beam direction. The target can be changed during the experiment via rotating the target wheel which is remotely controlled. Taken from Ref. [100].

Signals from individual readout strips are preamplified and shaped via DC-coupled VA-chips (64 strips per one chip), which transfer the signals further to the operational amplifiers in the front-end electronics board (see Fig. 2.4). The output signals are generated separately for the K- and S-side by the front-end electronics, which send the signals to an external custom-designed readout module SIDEREM8.
In total, six SSDs were located inside the evacuated aluminum target chamber as shown in Fig. 2.5. Two detectors were inserted into the beam line at a distance of 11 cm and 13.5 cm downstream from the target to identify and track the outgoing reaction fragments. The other

four SSDs were assembled into a $41\times41\times72$ mm$^3$ box around the target for measuring the QFS protons.

It should be noted that the SSDs are rather "slow" detectors, it takes the readout electronics approximately 5 $\mu$s to digitize the output signals for all the 1024 channels of a single SSD. Therefore, the SSDs are inappropriate for any sort of time measurements and, as a consequence, they cannot be used for triggering purposes. Instead, an external trigger coming from other parts of the setup is always used for these detectors.

### 2.3.2 Proton and $\gamma$-ray detection

The Crystal Ball (XB) is a large calorimeter aimed at the detection of photons and light charged particles. It consists of 162 NaI scintillating crystals folding into a sphere around the target. Each crystal is 20 cm long and is canned in 600 $\mu$m thick aluminum shell. The inner volume of the XB contains the evacuated aluminum target chamber with a supportive construction holding the target wheel and the SSDs (Fig. 2.5). The geometrical center of the XB coincides with a point at the downstream surface of the target, which is also chosen to be the origin of the laboratory coordinate system. The view of the XB, as well as the rest of the experimental section before ALADIN, is shown in Fig. 2.6.

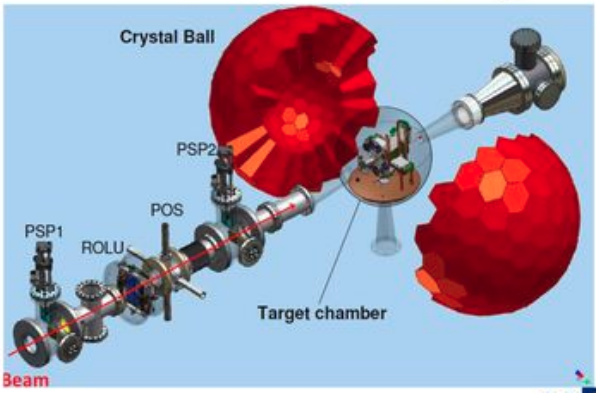


**Figure 2.6** – View of the Crystal Ball calorimeter and the experimental section before the ALADIN magnet. The target chamber with six Si-microstrip detectors is situated inside the calorimeter. 162 NaI crystals cover almost the entire $4\pi$ solid angle around the target.

The scintillating light produced by photons or by charged particles in individual crystals is converted into electric signal in the PMT attached to the outer flanges of the crystals. The initial design of the XB was intended for $\gamma$-ray detection only, however, it was accommodated to also detect protons. The energy deposited by a high-energy proton in one crystal can be one or two orders of magnitude higher compared to the energy of $\gamma$-rays, resulting in intense light pulses. Hence, for the sake of measuring proton energies, the configuration of some PMTs has been slightly modified [106]. Additional "low-gain" (proton) readouts were implemented on the 64 crystals located in the forward hemisphere, where most of the proton pairs from QFS reactions are expected to be observed. Therefore, each of these crystals is read out twice. One signal, called $\gamma$-ray branch, is read out at the final pickup anode of the PMT as before, while the second signal, called proton branch, is read out at the last dynode. The proton branch is not amplified any further, whereas the $\gamma$-ray branch undergoes an additional preamplification. While only the energy is recorded (using a Charge-to-Digital Converter (QDC)) for the proton branch, the signal from the $\gamma$-ray branch is split to measure both its time and energy. The energy is recorded with a QDC and the time signal is processed with a Constant

Fraction Discriminator (CFD) before being recorded with a Time-to-Digital Converter (TDC). Furthermore, the time signals (before the CFD) of several crystals together are used to provide a trigger signal for the whole detector.

### 2.3.3 Fragment tracking and detection

After the target, the outgoing reaction fragments have to be identified and measured. This is achieved with the aid of the dipole magnet ALADIN situated approximately 2 m away from the target and via the fragment tracking arm after the magnet.

Due to the Lorentz force, which acts on charged particles moving through the magnetic field, the trajectories of fully stripped fragments are bent in the magnet depending on their A/Z ratios. Thus, different isotopes travel along different trajectories. We can select the nuclei of interest by adjusting the magnet, for example in a way that only the fragments with $2 \leq A/Z \leq 3$ ( mostly B and Be isotopes) reach the TFW detector. They were deflected by an angle of $\sim 15°$ with respect to the incident beam.

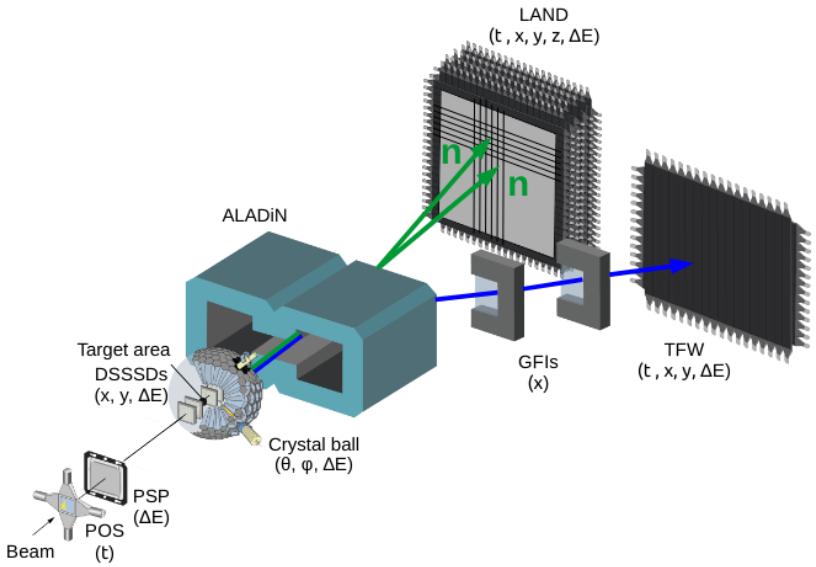


**Figure 2.7** – A sketch of the experimental setup used for the s393 experiment at GSI. Different detectors are shown and the observables they measure are listed in parenthesis. Taken from Ref. [93].

Behind the magnet, at a distance of 3 and 5 m, two Grosse Fibers detectors (GFIs) measured trajectories of the fragments in the dispersive plane of the magnet. Each GFI consists of 480 vertical 1 mm thick scintillating fibers arranged in a single row, forming a sensitive area with a total size of $50 \times 50$ cm$^2$. The scintillating light produced by a charged particle in a fiber is guided onto the cathode mask of the position-sensitive PMT. The light signal from each fiber arrives at a specific spot on the cathode and initiates an electron avalanche towards the anode, where the signal appears as a local charge distribution on the two-dimensional anode grid represented by 16 and 18 perpendicular readout wires. The center of gravity of this charge distribution is strongly correlated with the initial position of the light spot on the cathode, that is in turn associated with a specific fiber and the X−coordinate in the laboratory frame. More detailed information about the detectors and the hit reconstruction algorithm can be found in Refs. [107, 108]. A horizontal position resolution of about 1 mm can be achieved,

which corresponds to the thickness of a single fiber.

The TFW, placed 5 m downstream of the last GFI, measured the time of flight and the energy loss of the fragments. This detector is built out of 14 horizontal scintillator paddles in the first plane and a second plane having 18 vertical paddles. Each horizontal paddle has the dimension $196.6 \times 10.4 \times 0.5$ cm$^3$, while the vertical paddles have a dimension of $154.6 \times 10.4 \times 0.5$ cm$^3$. All 32 paddles are read out using a PMT on each side. The time, the energy loss $\Delta$E, as well as the position of each hit is measured. Having the time of flight between target and the TFW and knowing the length of the trajectory gives the velocity $\beta_f$ of the outgoing fragment, while the deposited energy determines its charge $Z_f$. As an example, the identification in charge and mass of the fragments observed after the interaction between the target and a $^{13}$B beam is presented (Fig. 3.4) in Sect. 3.1.

### 2.3.4 Neutron detection

As noted before, when produced in an unbound state during a knockout reaction, nuclei may emit neutrons. As neutrons are not influenced by the Lorentz force in the field of ALADIN because they are not charged, they will be distributed at around 0° outgoing angle after the magnet. Since the interaction cross-section of relativistic neutrons with matter is small, the measurements rely on a specific detection principle and a large active volume of the detector in order to increase the efficiency. The neutron detection is based on the conversion of neutron hits inside iron material into a shower of charged particles, which in turn can produce light in the scintillating material.

The "Large Area Neutron Detector" (LAND), which was located at around 14 m downstream of the target, is used for neutron detection (Fig. 2.8). The detector consists of ten identical $2 \times 2$ m$^2$ planes composed of 20 horizontal or vertical paddles. Each paddle is a composition of alternating 5 mm thick plastic-scintillator sheets and 5 mm thick iron sheets, and two PMTs are attached to the ends of a paddle. The times and charges in the PMT are readout by TDCs and QDCs, respectively. This information is used for reconstruction of the time and location of a hit within the paddle. The other two coordinates are determined by the absolute position of the paddle in the laboratory. LAND can provide high-efficiency time of flight measurements of neutrons with energies ranging from 0.1 to 1 GeV. A total depth of the detector's active volume is about 1 m, that is sufficient to reach an absolute efficiency of more than 90% for 1 GeV neutrons [109]. The time resolution ($\sigma$) is approximately 250 ps.

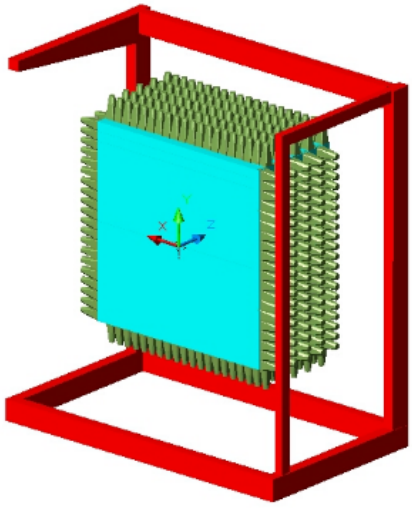

**Figure 2.8** – The Large Area Neutron Detector (LAND) consists of ten $2\times2\times0.1$ m$^3$ planes composed of 20 horizontal and vertical paddles. Each paddle is composed of alternating 5 mm thick plastic-scintillator sheets and 5 mm thick iron sheets with two PMTs attached to its ends.

## 2.4 Trigger system

Signals from different detectors are stored in the Data AcQuisition system (DAQ), where a trigger stamp can be assigned to each event based on user-defined conditions. Usually, the signal is sent from the trigger channel to the Constant Fraction Discriminator (CFD), which produces a logical output signal with the appropriate timing characteristics. By combining coincident logical signals arriving from different parts of the setup, one can set specific trigger bits to characterize the current event using a predefined trigger pattern (Tpat). For example, when the "spill-on" logic signal comes from the accelerator system in coincidence with a signal from POS and no signal from ROLU slits (POS !ROLU), it means that there was an incoming ion which will hit the target. This trigger is then called "Good Beam (G.B))". Requiring additional signals from XB, LAND or TFW, one can construct a Tpat indicating potential $\gamma$-ray, neutron or fragment event, respectively. The Tpat "XB OR" is assigned when at least one crystal in the Crystal Ball has a signal above the threshold, indicating a potential $\gamma$-ray event. "XB SUM" is another Crystal Ball trigger intended for the high-energy proton hits. It requires an integrated analog sum of all signals in the detector to be higher than a certain threshold value.

**Table 2.1** – Main experimental "spill-on" triggers.

| Trigger pattern | POS !ROLU | TFW | XB | LAND | Description |
|---|---|---|---|---|---|
| 1 | X | - | - | - | GB |
| 2 | X | X | - | - | GB + TFW |
| 8 | X | - | X | - | GB + XB |
| 128 | X | - | - | X | GB + LAND |

In the present analysis, we are only concerned with the "spill-on" bits, which means it is in coincidence with a trigger from the FRS monitor system, corresponding to delivery of beam to the R3B-LAND setup. Generally, for an event to be recorded, several detector systems need to provide a signal in coincidence for a TBit to be set. As an example, for XB Sum TBit to be set we need triggers from the Crystal Ball, TFW and POS!ROLU (signal in POS and no signal in ROLU ). The trigger signals were aligned time wise by delaying the signals from the different detectors. As a consequence, the trigger signal from the start detector (the POS!ROLU condition) is always supposed to come last and define the event time.

The "spill-on" TBits were built by a combination of detector triggers, which had timing conditions on them to reject pileups, and late triggers (i.e. only triggers within a certain time window after the start are recorded). Furthermore, the DAQ had a dead time of about 400 $\mu$s, which is about the time it needs to collect and write the data to disk. Any valid event arriving within this dead time was discarded. Since the reaction rate of the incoming ion on the reaction target is about 1%, and data acquisition rates are limited, only a fraction of the events was written to disk based on the TBit value. This is the down-scaling process. It is done to reduce the dead time of the DAQ and the storage space. What this means is that if a specific TBit has a down-scaling factor of say n, every $n^{th}$ event with that TBit is recorded and the rest are discarded. The aim is to record as much of the reaction data as possible while discarding the data with unreacted events. If an event has multiple TBit values set, each TBit has to undergo the down-scaling check separately. So if for example, Fragment and XB Sum (Crystal Ball) TBit were present in an event, but Fragment TBit was removed due to down-scaling then only XB Sum Tbit will be written for that event. In the present experiment, reaction TBits like XB Sum and Neutron were not down-scaled but the G.B and Fragment TBits were heavily down-scaled by factors like 64/128 or 32/64 respectively depending on the run.

Since the present analysis requires counting of reacted as well as unreacted events, a precise estimation of the down-scaling factors had to be made as explained in Appendix A. Since only 1% of the incoming beam undergoes reaction (i.e. very small cross-sections) at the target, with such large down-scaling ( of the order of $\sim 100$) we are left with very small numbers with large uncertainties. Therefore, even though the experiments are designed generally to run for several days, we have only a few events corresponding to the reaction of interest and if we use down-scaling factors like n $\sim$100, the uncertainties are also scaled by this factor. Hence, it is suggested, in future experiments, in order to facilitate such cross-section calculations, to

take at least a couple of hours of data without down-scaling as compared to several days with such large down-scaling factors.

## 2.5 Calibration of detectors

At this stage, recorded data are in the form of digitized analog signals coming from individual detector channels. These signals are collected from all detectors during the experiment, processed and recorded by the Data AcQuisition system (DAQ) [110] based on some trigger decisions. Before using these "raw" recorded data for the actual analysis, the signals from detectors must be converted and calibrated so that they can be interpreted in terms of physical quantities such as times, distances, energy losses etc. The calibration uses the LAND02 software package developed mainly by H. Johansson for the LAND-R3B setup [110]. The code is based on gradual conversion of the initially digitized signals from the electronics ("RAW" level) into individual particle hits in the detectors and eventually to particle tracks ("HIT" and "TRACK" levels, respectively). A set of input parameters is determined on every calibration step using specific LAND02-utility programs. Applying these parameters to the current data level, the following level can be reconstructed. Additionally, the LAND02 software can output the data at each level in a user-specified format (e.g. ROOT file).

In general, all detectors record either deposited energies or times of occurrence. This information can then be combined to determine energy losses, charges, times of flight, positions, and masses of the involved particles. The calibration of the s393 campaign was made by other members of the R3B collaboration shortly after its completion. In the following, I will give the general lines of these calibration procedures, more specific details can be found in Refs. [111, 112].

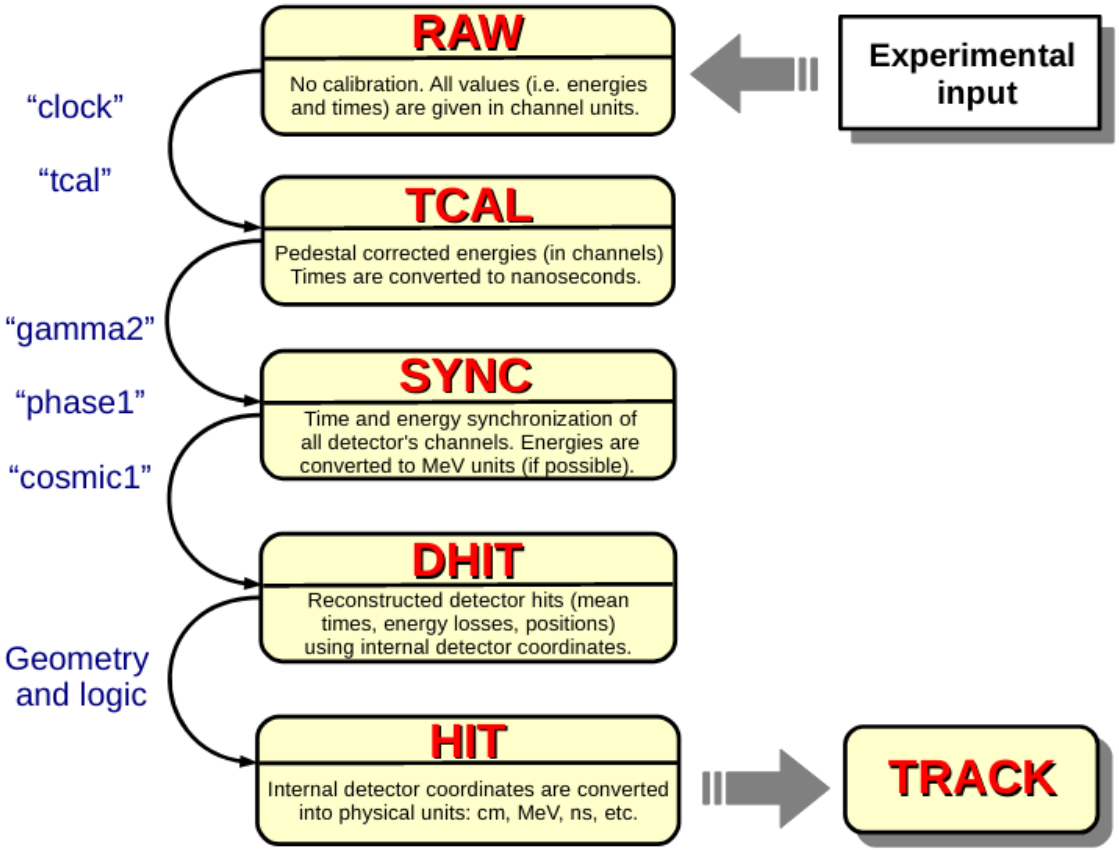


**Figure 2.9** – Structure of the LAND02 software. Different calibration levels are shown inside boxes together with a short description of the specific calibration steps. The corresponding LAND02-utility programs (blue font) are shown on the left side. In most of the cases, the transition from DHIT to HIT level requires essentially the knowledge of the detector/setup geometry. Figure taken from Ref. [100].

- Crystal Ball: The calibration of XB consists of three parts:
  - The energy calibration of the $\gamma$-rays readout of every single crystal.
  - The energy calibration of the proton readout of every single crystal.
  - The synchronization of the time information of all crystals among each other.

  First of all, the calibration of the $\gamma$-ray branch is done with dedicated calibration runs with $\gamma$-ray sources. For the experimental campaign s393 (and s389), $^{22}$Na, $^{56}$Co, $^{60}$Co, and $^{88}$Y sources were available with energies up to 3.3 MeV. The lack of high-energy calibration sources results in a systematic uncertainty for high-energy entries. Next, the proton branch is calibrated using muons from the cosmic background radiation. They are measured "spill-off" during physics runs and in dedicated cosmic runs during the whole experiment. The energies of the traversing muons are then compared to simulations. Finally, the time synchronization is done using runs with a source emitting two coincident $\gamma$-rays. For this calibration step, events in which the full energy of both $\gamma$-rays was deposited in exactly one crystal each are selected and the time difference between these crystals is saved. With time differences between each combination of crystals, the time offset for each crystal can be determined. In this case only the $\gamma$-ray readout is used for synchronization. The resulting calibration parameters are then applied to both, the

$\gamma$-ray and the proton readout. The gamma2 routine provided by LAND02 helps with the calibration using muon events and the time calibration. The calibration used in this work was done by Ronja Thies and is described in detail in Ref. [117].

During the energy calibration it was observed that the energy resolution of several crystals was not good enough to calibrate them, since the photopeaks from the source measurements merge or could not be identified at all. Those detectors are excluded from the analysis completely. Furthermore, crystals whose energy resolution is bad and which have a big uncertainty in their energy calibration are used during the addback procedure but are excluded from the $\gamma$-ray spectrum if they are the dominating crystal.

- TFW. The calibration routines clock, tcal, and phase1 are embedded in the LAND02 calibration software. On the lowest level, the calibration includes the subtraction of the baseline for the energy measurement, and a gain and offset to convert channel numbers into times in ns for the time measurement for each PMT. Within the next step, gain factors are applied to match the energy and offsets to match the times of the two PMTs of one paddle. Additional gain factors are then used to match the paddles with each other to finally get one time, position, and energy-loss measurement for the whole detector. A detailed description of the procedure can be found in Ref. [112]. The calibration used in this work was done by Christoph Caesar in Ref. [113].

- Silicon Trackers. For the SSDs, the first step of the calibration is the same as for the TFW. The LAND02 routine clock is used to determine the baseline and the width, $\sigma$, of the noise. After the subtraction of the baseline, energy entries in neighboring strips are sorted into clusters. The energy and the position of these clusters are then used to determine the energy loss and the position of the traversing particles. This procedure is explained in detail by Matthias Holl in Ref. [114]. He points out that the charge collection varies with the position $\eta$ within one strip. This leads to a variation of the measured energy depending on $\eta$. Furthermore, hits seem to occur more often close to the border of a strip than in the center. This effect needs to be corrected in order to calculate the correct cluster energy as well as the correct cluster position. Additionally, Matthias Holl describes how to reconstruct the cluster energy, when some strips in a cluster, especially in the center, are broken and do not provide an energy signal.

  In Ref. [99], Ina Syndikus completed this calibration as she found out that it was not sufficient. The calibration parameters for the $\eta$ correction seem to be run dependent. Therefore, the $\eta$ correction was redone for the analyzed data using a dedicated script written by Matthias Holl. The first step of this procedure is the $\eta$-position correction. Without the correction, the probability for a reconstructed position is higher at the edges of each strip, i.e. $\eta$=0 and $\eta$=1. After the correction the probability is the same for all $\eta$. An intermediate step corrects for the different gains of the strips by fitting normal distributions to the energy loss depending on the position.

# Analysis techniques



In this chapter, I will present the techniques used to analyze the data obtained from the experiment described in the previous chapter. To analyze the data, we start by identifying incoming nuclei and outgoing fragments after reaction with the target. Secondly, I present the methods used to fit spectra of the $\gamma$-rays that were emitted in coincidence with residual fragments and deduce the efficiency of detecting the $\gamma$-rays. I will then present the invariant-mass method that is used for reconstructing the decay energy when one or more neutrons are emitted. This method is going to be described, as well as the fit methods for fragment+1n and fragment+2n energy spectra. Finally, I present the method of Dalitz plots used for studying three-body correlations.

## 3.1 Identification of the incoming beam

In the scope of our study, we need to be able to identify and characterize the incoming nuclei event by event. Therefore, we need to know the mass-to-charge ratio $A_b/Z_b$ and the charge number $Z_b$. The quantity $A_b/Z_b$ is related to the velocity of the beam $\beta_b$ and the magnetic rigidity $B\rho$ of FRS by the following equation:

$$\frac{A_b}{Z_b} = \frac{B\rho}{C}\frac{1}{\beta_b\gamma_b} \tag{3.1}$$

While B$\rho$ is given by the settings of FRS, $\beta_b$ needs to be deduced by the ToF measurement. The velocity $\beta_b$ and the charge number Z are also linked to the energy lost $\Delta$E by ion passing through matter by the well known Bethe-Block formula:

$$\Delta E \propto \frac{Z_b^2}{\beta_b^2} \tag{3.2}$$

We can rearrange this formula such as

$$Z_b \propto \beta_b \sqrt{\Delta E} \tag{3.3}$$

The incoming $^{13}$B beam is identified by two position-sensitive silicon detectors PSP1 and PSP2, placed at the entrance of the experimental hall. In addition to these tracking detectors, the beam line before the target was equipped with a beam collimator ROLU and a thin plastic scintillator POS (see details on POS in Sect. 2.1.1), which was designed for ToF, position and $\Delta E$ measurements.

To complete the identification of the incoming ion, given the FRS setting (B$\rho$), we only have to determine its velocity $\beta_b$. This is done by measuring the ToF between a start and stop detectors separated by a distance of 55 m. In our case, the start detector is the plastic scintillator paddle at S8 (see Fig. 2.2) and the stop detector is the plastic scintillator POS at the entrance of Cave C . With the times measured by these two detectors, $t_{start}$ and $t_{stop}$, we can deduce the velocity of the incoming ion $\beta_b$ using the ToF method below:

$$\beta_b = \frac{d}{c \times (t_{start} - t_{stop})} \tag{3.4}$$

Where $c$ is the speed of light and d is the distance between these two detectors (55 m). Now that we have access to $Z_b$ and $A_b/Z_b$, we can select the ion of interest among the cocktail of secondary beams (Fig. 3.1 ).

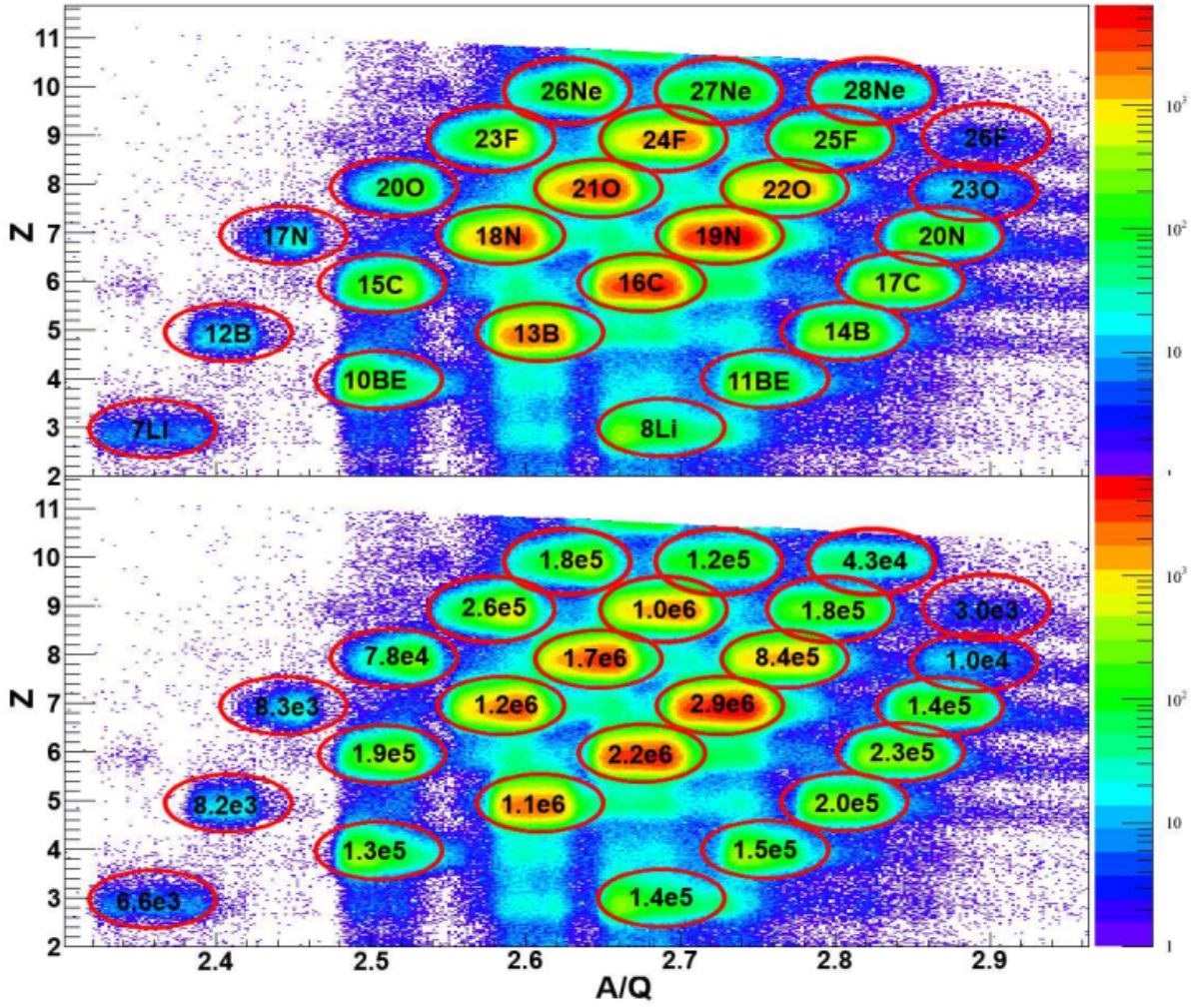


**Figure 3.1** – Top: Identification of the nuclei in the cocktail of secondary beams. Bottom: Number of detected events associated to each identified ion beam.

Now that the identification of the incoming ions is completed, we need to determine their trajectories using the PSP and deduce the position of the interaction of the ion onto the reaction target. The convention used in the current analysis for the coordinates is the following: Z-axis is in beam direction, X-axis and the y-axis are perpendicular to the beam direction, with the former pointing to the left and the latter to the top. Each in-beam SSD has two sides, s and k, delivering the measurements in the x- and y-directions, respectively. Thus, the trajectories of the incoming ions are determined from these positions, knowing the distance between the two SSDs.

## 3.2 Identification of outgoing fragments

When the incoming beam of $^{13}$B hits the target nucleus, reactions occur. We then need to identify the outgoing reaction products that are eventually emitted in coincidence with one or more neutrons and/or $\gamma$-rays. It is done in two steps:

- We first determine the charge Z corresponding to Z = 4 (Be) from the measurement of energy-loss $\Delta E$ in the SSDs located after the target and in the TFW.
- Second, we use the charge obtained together with the trajectories through the magnetic field of ALADIN to reconstruct the mass of the outgoing fragments.

### 3.2.1 Determination of the charge of the fragments

The charge Z of the outgoing fragments is determined by using the energy deposition in two SSDs, placed downstream of the target and in the TFW at the end of the fragment arm. By selecting the same Z value in the SSDs and in TFW, we ensure that no reaction occured. The two SSDs, SSD3 and SSD4, could not be fully used. The k-side of SSD4 had several broken strips and it wouldn't be a good choice to use it for the charge cut. Also, the s-side of both SSD3 and SSD4 have a bad energy resolution even after the $\eta$ correction (see Sect. 2.5). Therefore, only the energy loss measured with the k-side of SSD3 and the TFW are used to determine the charge of the outgoing fragments. As an example, the 2D-plot below (Fig. 3.2) shows isotopes produced by reaction of $^{13}$B with the target. We can see all identified isotopes down to helium. For the analysis, fragments of interest are selected by applying two dimensional cuts to the 2D-graph. A cut on beryllium isotopes is shown as an example.

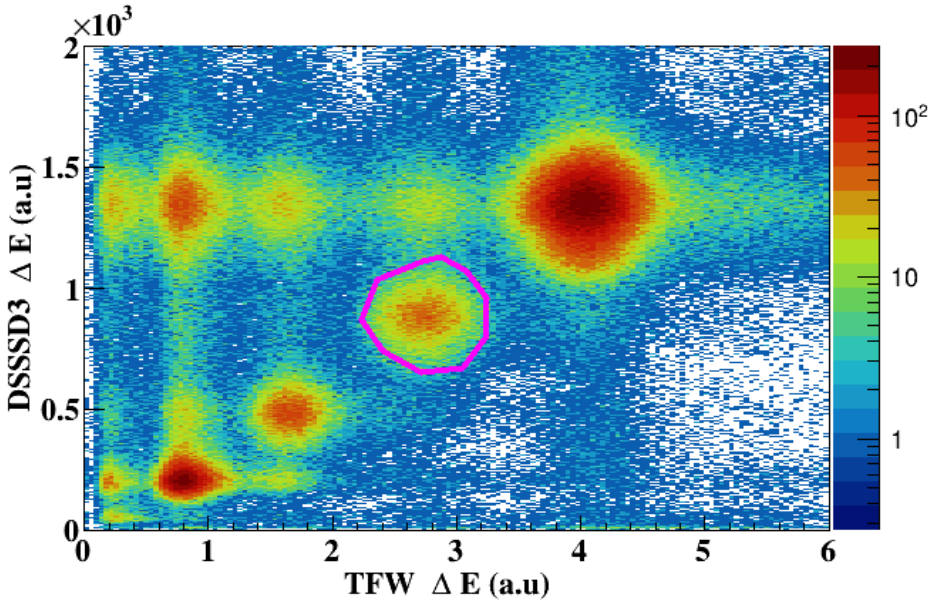


**Figure 3.2** – Charge identification of the isotopes produced from the reaction between $^{13}$B beam and the target. The selection on Be isotopes is shown here as we are interested in one proton removal reactions.

### 3.2.2 Calculation of the fragment mass

For a complete identification of the outgoing fragments, their mass needs to be determined. For this purpose, we use the detection position in the GFis and time and position detection of TFW. At first order, a separation in mass is possible by looking on how the x-position in GFi1 changes compared to the difference between x-positions in GFi1 and GFi2. In fact, the difference in detection position in the two GFis indicates the existence of an angle $\theta_{fra}$ formed by the trajectory of the fragments with respect to the direction of the beam (z-position) (see Fig. 3.4). Given that this angle is small, we can approximate it by:

$$tan(\theta_{fra}) \sim \theta_{fra} = \frac{GFi1_x - GFi2_x}{GFi1_z - GFi2_z} \tag{3.5}$$

Since the distance between the two detectors, d = GFi1$_z$ - GFi2$_z$, is constant, the difference in trajectories for two different fragments depends only on x-positions in GFi1 and GFi2:

$$\theta_{fra} \sim GFi1_x - GFi2_x \tag{3.6}$$

Hence, we can deduce an expression for the mass for a given Z:

$$A = \theta_{fra} - constant \times GFi2_x \tag{3.7}$$

or

$$A = C_1 \times GFi1_x + C_2 \times GFi2_x \tag{3.8}$$

A further precision on the mass is made by considering the interaction position of the incoming beam on the target and the ToF from the target to TFW. It was shown in Ref. [116] that the mass of the outgoing fragment, can be calculated using the following formula:

$$A \propto C1 \times GFi1_x + C2 \times GFi2_x + C3 \times X_{target} + C4 \times ToF_{target-TFW} \tag{3.9}$$

The parameters C1, C2, C3 and C4 are fixed by the experimental measurements, by tuning ALADIN to match the position and time information for a given charge Z.

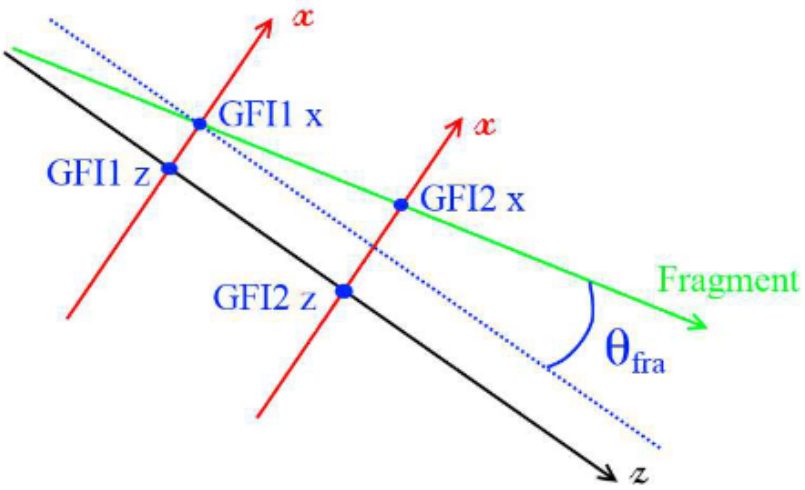


**Figure 3.3** – GFi detectors are used for fragment tracking after ALADIN. The x-position in both GFi's are used to deduce the mass A of the fragment. Figure taken from [116].

With the mass calculated this way, different isotopes are clearly separated and a cut can be applied to select the outgoing fragment of interest. An example of the identification of different fragments produced from the reaction $^{13}$B(-1p)$^{12}$Be is shown on Fig. 3.4. Three fragment masses ($^{12}$Be, $^{11}$Be and $^{10}$Be) are identified corresponding to bound states of $^{12}$Be and unbound states decaying by emitting one or two neutrons.

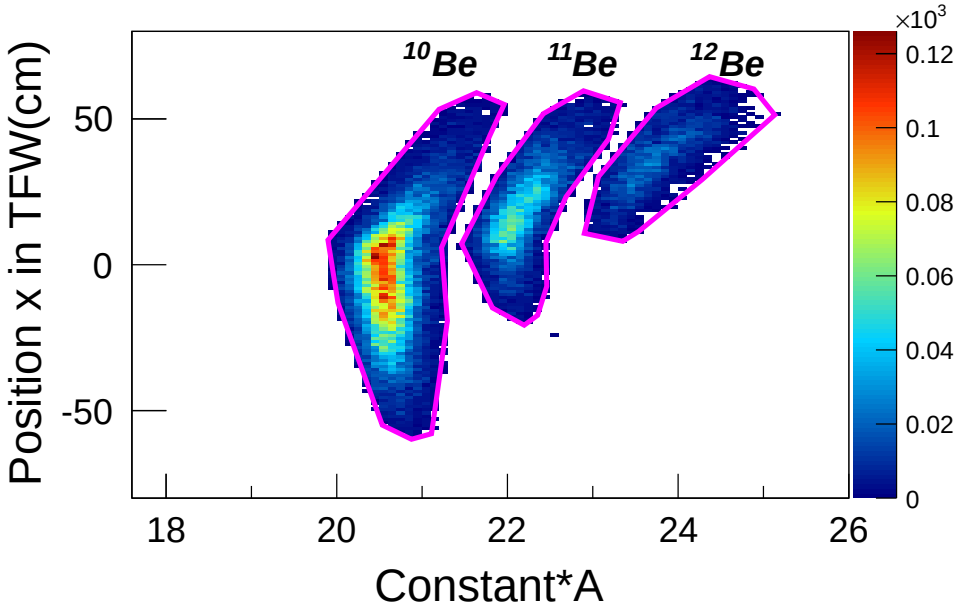


**Figure 3.4** – Mass identification of Be isotopes (Z=4) produced from the interaction of a $^{13}$B beam with the target (here $CH_2$s).

## 3.3 Analysis of $\gamma$-ray energy spectra

As stated before, one of the goals of this thesis is to study bound states of the nucleus of interest ($^{12}$Be), which can be populated in the ground state or in excited states. The study of bound excited states is performed through the detection of $\gamma$-rays, whose energy gives direct information on the energy of the levels where they decay from. $\gamma$-rays are detected via their interaction with the materials of the detector (NaI crystals). At a few MeV energy range, there exists three kinds of interaction between $\gamma$-rays (photons in general) and matter : photoelectric effect, Compton effect and $e^-e^+$ pair creation.

The $\gamma$-rays can deposit the whole energy in a single crystal via the photoelectric effect, but also can be Compton scattered to neighboring crystals, depending on their energy. An addback routine, consisting in summing up the energies in different crystals which belong to one $\gamma$-ray, is applied in order to correct for the Compton effect.

Energy and number of the emitted $\gamma$-rays can then be deduced from $\gamma$-ray energy spectrum by fitting it taking into account the photopeak and other contributions to the spectrum. In this thesis, all other contributions except the photopeak will be called background. This "background" includes Compton continuum, cosmic and background $\gamma$-rays in the experimental hall and the Bremsstrahlung effect induced by the deceleration of protons emitted in the knockout reactions or electrons/positrons from $e^-e^+$ pair creation. Additionally, since the $\gamma$-rays are emitted by fragments moving with relativistic velocities v $\sim 0.73c$, the $\gamma$-rays are boosted in the forward direction and their energies need to be Doppler corrected.

Finally, after applying an addback algorithm and the Doppler correction, the resulting $\gamma$-ray energy spectrum can be fitted to study the bound states of nuclei of interest.

### 3.3.1 Estimation of the background in $\gamma$-ray energy spectra

The first step in fitting the $\gamma$-ray energy spectrum is to estimate the background and identify all the photopeaks. Previously, in Ref. [100], an exponential form was taken for the background. However, a more rigorous way is to estimate the background from a nucleus that does not have any bound excited state, for which, the $\gamma$- ray energy spectrum contains only the background.

The first excited state of $^{23}$O at 2.8 MeV is above the neutron separation energy ($S_n$ = 2.7 MeV) [102]. Then, no photopeak is expected and the only contribution to the $\gamma$-ray energy spectrum of $^{23}$O is from the background. The shape of the background is then better fitted in the experimental spectrum using this function:

$$f_{BG} = E_{\gamma}^{(1-a\times E_{\gamma})} \times exp(-b \times E_{\gamma}) \tag{3.10}$$

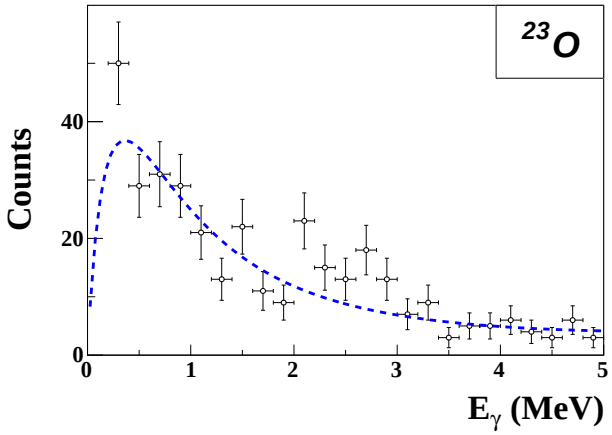


**Figure 3.5** – The shape of the background (in blue) is obtained by fitting $\gamma$- spectrum of $^{23}O$ by the function given in Eq. 3.10.

The function in Eq. 3.10 (Fig. 3.5) is chosen such that it increases rapidly from low energies, and decreases exponentially at higher energies (hereby mimicking a trigger threshold effect). We will use this lineshape in order to describe the background contribution to the different $\gamma$-ray energy spectra analyzed in this thesis.

### 3.3.2 Determination of photopeak's resolution

The photopeak of detected $\gamma$-ray has a width which is due to different experimental effects, such as resolution of the detector and the Doppler broadening. The photopeaks will be fitted by Gaussian distributions with the Full Width at Half Maximum (FWHM) defined as $2.355 \times \sigma$. The resolution $\sigma_E(E_{\gamma})$ is determined by fitting a Gaussian function to the photopeak of nuclei that were studied, and whose energy levels are known from previous studies: $^{11}$Be (320 keV),$^{14}$B (650 keV), $^{12}$Be (2 MeV),$^{22}$O (3.1 MeV) and $^{10}$Be (2.59 MeV and 3.3 MeV). The results of the fits are reported in Tab. 3.1.

**Table 3.1** – Values of the width in % of $E_\gamma$ obtained by fitting several photopeaks using a Gaussian function.

| $E_\gamma$ (MeV) | 0.320 | 0.650 | 2.08 | 3.1 | 3.3 |
|---|---|---|---|---|---|
| $\sigma_E$/E (% ) | 15 ± 1 | 12 ± 3 | 9 ± 2 | 8.4 ± 2.0 | 9.0 ±1.5 |

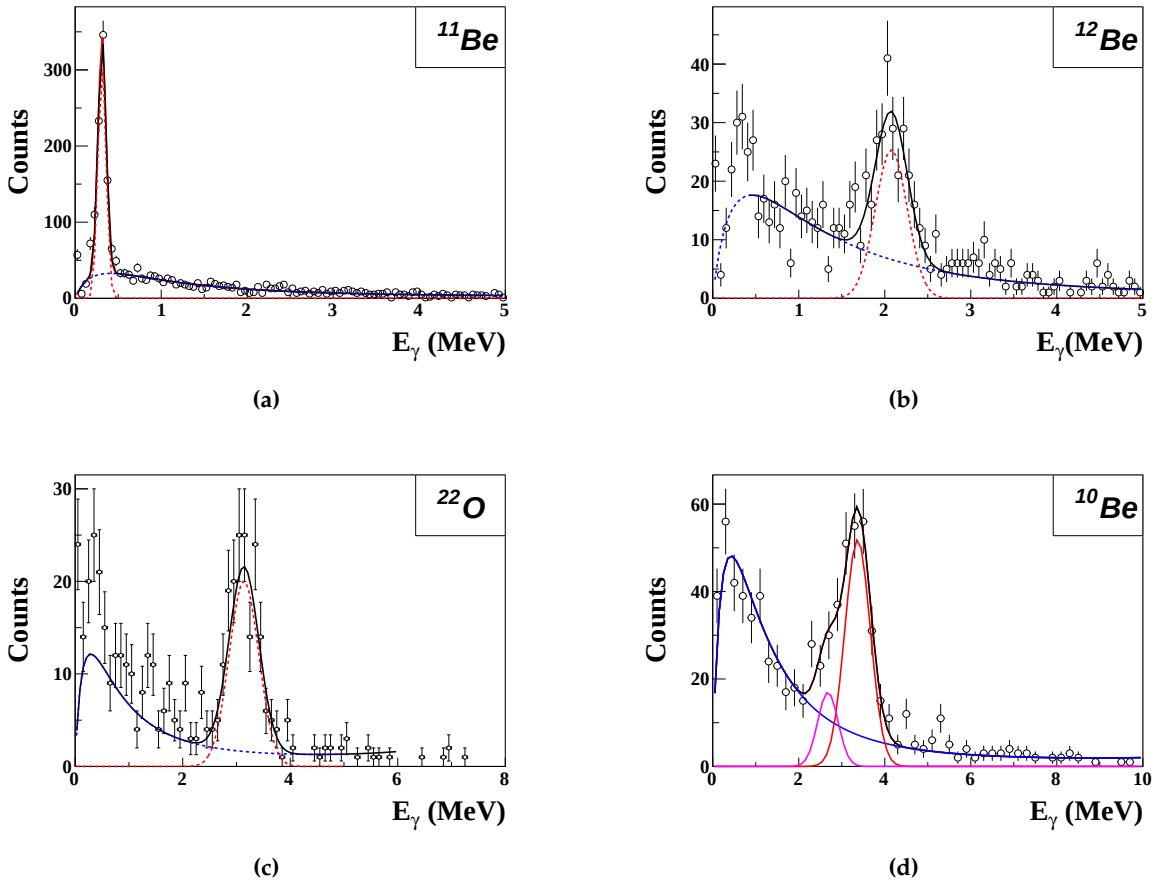


**Figure 3.6** – Fit of the photopeaks in different nuclei. $\gamma$-energy and the width $\sigma_E$ are deduced from the fit. Results are reported in Tab. 3.1.

Looking at the values in the table, we see that at high energy $\sigma_E / E$ is constant. It increases slightly at low energy, i.e the resolution decreases at low energy. An energy-dependent resolution curve is obtained by fitting the values in Tab. 3.1 by the following function:

$$\frac{\sigma_E}{E} = e^{(-a-b\times E_\gamma)} + c \tag{3.11}$$

The result is a resolution curve that can be used to fix the width of the photopeak given the $\gamma$-ray energy (Fig. 3.7).

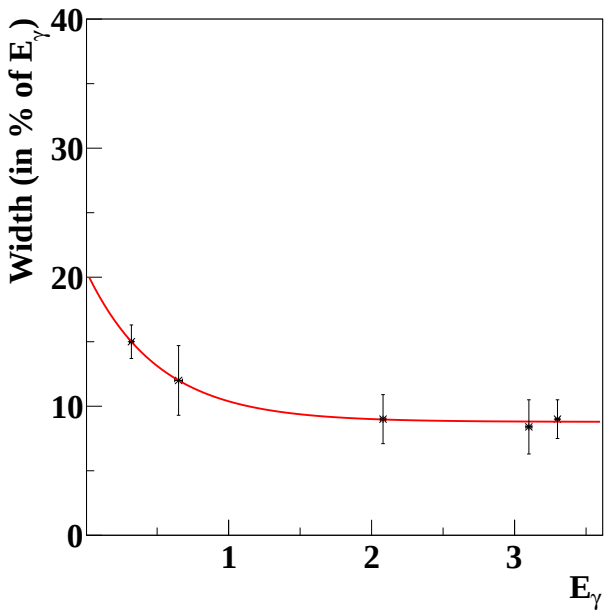


**Figure 3.7** – Resolution curve that gives the relation between the width and energy of a photopeak. The values of the Tab. 3.1 are fitted by a function of the form $\sigma_E/E = exp(-a - b \times E_\gamma) + c$, with a= 2.13, b= 1.99 and c= 0.087.

### 3.3.3 Efficiency of Crystal Ball

The geometry of the array and the thickness of the detectors are true assets to detect $\gamma$-rays with high efficiency. However, due to the mechanisms of interaction with detector materials, not all of them are detected in the photopeak, which is used for their counting. The number of detected $\gamma$-rays over that of the emitted ones is called the $\gamma$-ray efficiency. There are also holes where the beam can pass and this leads to some loss of geometrical efficiency. Hence, we must determine the $\gamma$-ray efficiency before doing the counting from fitting the $\gamma$-ray spectrum.

The traditional way of getting the efficiency of a detector is to use a source measurement and simulation, as done in Refs. [99, 100]. In Ref. [99], they used a $^{60}$Co source which decays mainly by the $4^+$ state of $^{60}$Ni, and then via a cascade of two successive $\gamma$-ray with energies of $E_1 = 1.173$ MeV and $E_2 = 1.332$ MeV. An $^{88}$Y source with $\gamma$-rays at 0.898 MeV and 1.836 MeV was also used in Ref. [100]. This source was placed at the center of Crystal Ball before and after the experiment. Simulations using a GEANT4-based code, R3BRoot, were made and compared to the measured events from the source. In this way the simulation is validated and can be used to determine the $\gamma$-ray efficiency also in regions where no source was available. We report the efficiencies of Refs. [99, 100] in the Tab. 3.2 and in Fig 3.8a.

| $E_\gamma$ (MeV) | 0.898 | 1.173 | 1.332 | 1.836 |
|---|---|---|---|---|
| $\epsilon_\gamma$ ( % ) from source measurement | 48 | 43.6 | 41 | 36 |
| $\epsilon_\gamma$ ( % ) from simulation | - | 44.3 | 42.3 | - |

**Table 3.2** – The $\gamma$-efficiencies obtained from source and from simulation [99, 100].

This method is valid for sources at rest. However, in the experiment with radioactive beam, the determination of $\gamma$-ray efficiency becomes tricky due to the presence of a background from high-energy protons [100]. In fact, the $\gamma$-rays emitted by in-flight nuclei will be detected in the same event as $\gamma$-rays of the proton-induced background. Moreover, an unexpected decrease of the efficiency in the current data set was noticed. Therefore, we need to determine the factor by which the efficiency decreases, assuming that it is the same at all energies. For this purpose, we deduced experimentally three values of the efficiency, which are 34 $\pm$ 7%, 30.5 $\pm$ 9.8% and 28 $\pm$ 5% at 320, 620 and 3368 keV, respectively. The value of 30.5 $\pm$ 9.8% at 620 keV is obtained by comparing the spectroscopic factor $C^2S$ of $^{14}$B from Ref. [118] and the cross-sections measurement with the data of our experimental campaign. The other values will be deduced by using $\gamma$-neutron coincidence discussed in Sect. 4.3. As we can see on Fig. 3.8, the $\gamma$-ray detection is energy-dependent and decreases at both ends of the energy spectrum. The low energy efficiency cut is rather sharp due to the electronic threshold applied to cut off the low energy $\gamma$-rays from the background. The value at 320 keV gives the $\gamma$-ray efficiency at the threshold. The procedure is as follows, first we use simulations to determine the global shape of the efficiency curve for $\gamma$-rays emitted in-flight. Second, we apply a scaling factor of 0.523 $\pm$ 0.065 in order to match the efficiencies determined for the three cases mentioned above.

Using the function in Eq. 3.12 [129] to fit the efficiency values, we obtain an efficiency curve that we can use for any detected $\gamma$-ray energy (Fig. 3.8b).

$$ln\varepsilon + 25 = p_1 + p_2 \times ln(E_\gamma) + p_3 \times (ln(E_\gamma))^2 \tag{3.12}$$

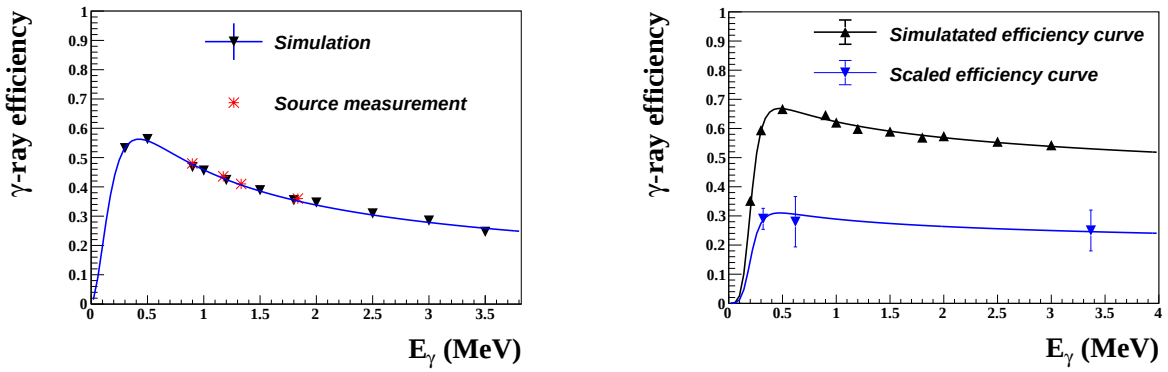


**Figure 3.8** – (a): $\gamma$-ray efficiency curve from source simulation (black dots and line) validated by source measurement from Refs. [99, 100] (red). (b): $\gamma$-ray efficiency curve simulated for $\gamma$-rays emitted in-flight. The simulated curve is scaled down by a factor of 0.523 $\pm$ 0.065 which is deduced from the in-flight data described in the text.

## 3.4 Analysis of the fragment+ neutron(s) relative energy

In this section, I will present the techniques used to analyze fragment + one or more neutrons decay energy spectra. When resonant states above the neutron emission threshold are populated, we study them by reconstructing the energy of the unbound systems before they decay. This is done by computing the relative energy between the emitted $x$ neutrons detected in LAND and the fragment $^{A-x}X$ detected in TFW using the invariant-mass method,

which is described in the following. In the case of fragment+2n, the interactions between the neutrons in the final state play a major role in the study of n-n correlations. We will then also present the method of Dalitz plots used to study these final state interactions.

### 3.4.1 Invariant-mass method

For an unbound system, after decay, the invariant-mass can be computed from the momenta of the decay products. The full kinematics measurement of reaction products allows us to deduce the invariant-mass which is linked to the decay energy of the unbound system. We will express physical quantities (energy and momenta) in natural units ($c = 1$). The invariant-mass is given by the relations below:

$$M_{inv} = \sqrt{\left(\sum_{i=1}^{N} E_i\right)^2 - \left(\sum_{i=1}^{N} \vec{p}_i\right)^2} \tag{3.13}$$

Where $P_i = (E_i, \vec{p}_i)$ , is the 4-momentum of a particle labelled "i". The rest mass is :

$$m^2 = (E, \vec{p})^2 = E^2 - p^2 \tag{3.14}$$

The decay energy $E_d$ of the unbound system before decaying is defined as the difference of the invariant-mass of the system and all the rest masses $m_i$ of the decay products:

$$E_d = M_{inv} - \sum_{i=1}^{N} m_i \tag{3.15}$$

Applying the relation of Eq. 3.15 in the case of a two-body unbound system composed by a fragment and one neutron, we obtain:

$$E_d = \sqrt{m_f^2 + m_n^2 + 2(E_f E_n - |\vec{p}_f|\,|\vec{p}_n|\,cos\theta)} - m_f - m_n \tag{3.16}$$

where $f$ denotes the fragment and $n$ the neutron, and $\theta$ is the relative angle between them.

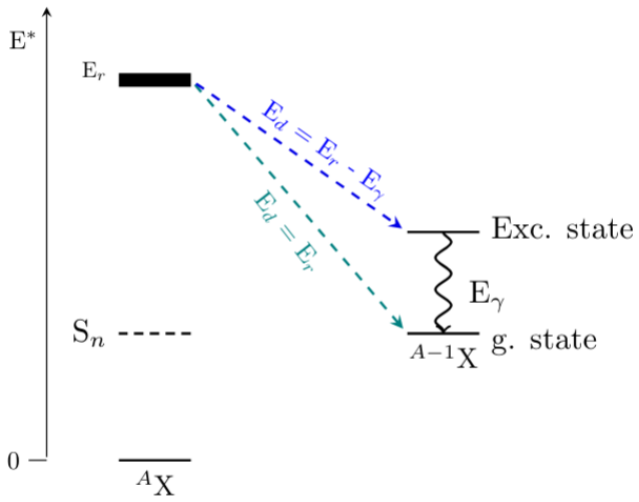


**Figure 3.9** – Schematic representation of the relation between the resonance energy $E_r$ and the decay energy $E_d$ for a fragment $+n$ system, where the fragment is populated in its ground and excited state (see text for more details).

The fragment can be populated in its ground state or excited state (Fig. 3.9). In the first case the excitation energy is given by the decay energy plus the neutron separation energy $S_n$. If the fragment was populated in the excited state, it will emit a $\gamma$-ray that is detected and analyzed as described in Sect. 3.3. The excitation energy $E_x$ is then given by the expression:

$$E^* = S_n + E_d + E_\gamma \tag{3.17}$$

### 3.4.2 Fit procedure

The $E_d$ spectrum obtained by the invariant-mass method contains information about resonances and their decay modes. To extract the information on the centroid energy or width of the resonance for example, we are going to fit the experimental spectrum using Breit-Wigner function (described in Sect. 1.3.2), folded by the response of the detector, which will be addressed in Sect. 3.4.3. Below, I give a brief description of the fit procedure. $E_d$ histograms are composed of events distributed in bins that we can compare with the Breit-Wigner function bin by bin. We use the notation:

- $y_i$ : number of events in the $i^{th}$ bin of the test function.
- $n_i$ : number of events in the $i^{th}$ bin of the experimental spectrum.
- N : total number of experimental events ( $N = \sum n_i$).

The fit procedure follows three steps:

- The first step, called point estimation, consists in the determination of the best fit parameters matching the fit function $y_i$ to the experimental points $n_i$.
- The second step is to determine the uncertainty of the result. This step is called confidence interval estimation.
- The final step is to check the goodness of fit.

The fit procedure provides a result in the first step, but this last step will show if the model is suited to describe the data. The most common method to do all three steps is the usage of $\chi^2$ statistics. The point estimation is done by minimizing the $\chi^2$ value. The result corresponds to a value $\chi^2_{best}$. The uncertainties of the fit parameters are estimated by the values for which $\chi^2$ = $\chi^2_{best} + 1$ ([119], p.525). The goodness of fit is tested by calculating the reduced $\chi^2$ expressed as:

$$\chi^2_{red} = \frac{\chi^2}{NDF} \tag{3.18}$$

with NDF being the number of degrees of freedom of the fit. In this work, histograms are compared bin by bin, the degrees of freedom can be estimated as the number of bins used for the fit minus the number of parameters in the fit, which are the centroid energy, width, amplitude and angular momentum. $\chi^2_{red}$ is close to 1 when data and the fit are in excellent agreement, larger than 1 otherwise.

### 3.4.3 Resolution and efficiency of neutron detection

When comparing the $E_d$ spectrum to fit function as described in previous section, one has to take into account the response of the experimental setup. The apparent width of the resonance is broadened by the experimental resolution which varies also as a function of the decay

energy. Hence, in the process of fitting experimental data, the fit function is folded with the resolution(Fig. 3.10). The latter is obtained by simulating at different relative energies of the 2-body system $^{11}$Be+n, assuming a Dirac delta function as input and observe the broadening due to the experimental setup. The energy of the incoming beam is 430 MeV/nucleon.

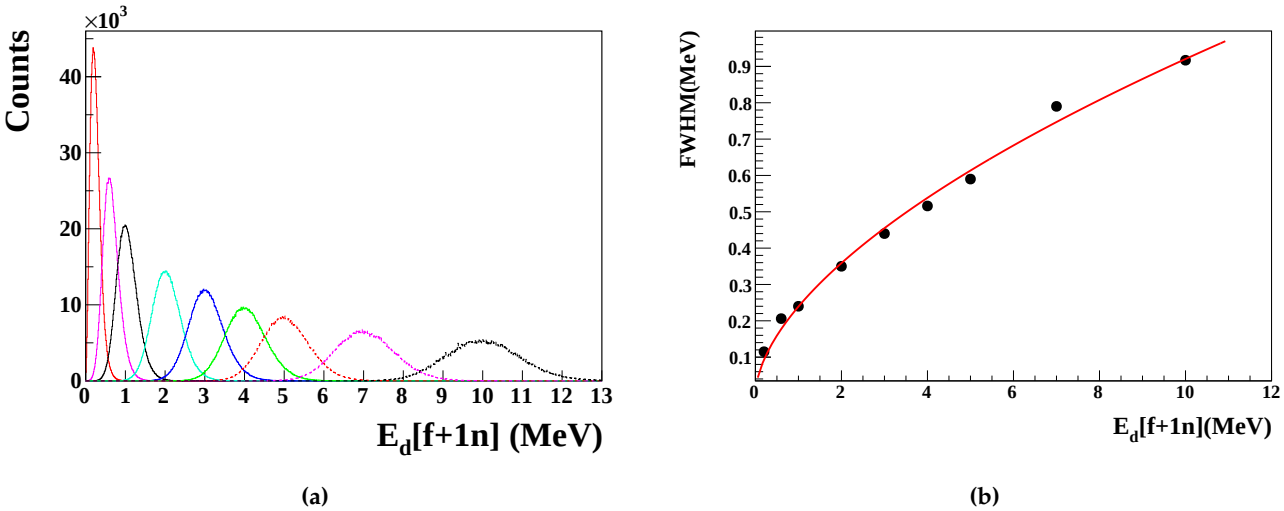


(a) (b)

**Figure 3.10** – (a) Evolution of the fragment-neutron relative-energy resolution as a function of the decay energy $E_d$ obtained by simulation. The inputs of the simulations are Dirac delta functions. (b) Evolution of the resolution as a function of decay energy. Data points are fitted by the function FWHM= $0.24 \times E_d{}^{0.58}$.

The number of counts and shape of the $E_d$ spectrum are also affected by the detection efficiency and geometrical acceptance, respectively. The geometrical acceptance is the probability that an emitted neutron reaches the detector. In fact, a neutron of high relative energy may not be detected in LAND when emitted far off the beam axis. The geometrical acceptance for 1n and 2$n$ detection (Fig. 3.11) decreases at high relative-energies, where neutrons start to deviate from the initial trajectory and fall off the detector. We see a also a decrease of the 2n acceptance at low relative energies due to the cross-talk filter.

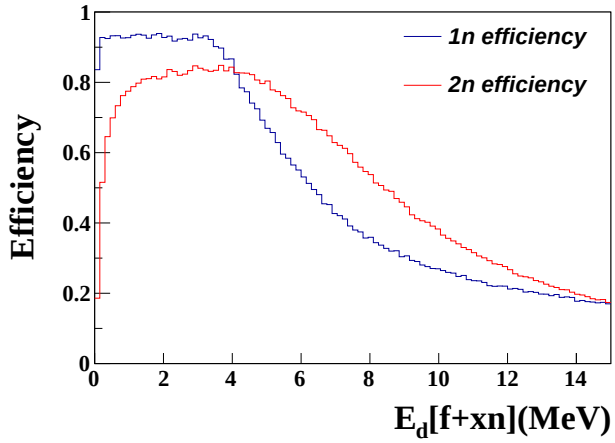


**Figure 3.11** – Neutron detection efficiencies for one (in blue) and two (in red) neutrons as a function of decay energy. The decrease of the 2n efficiency at low energy is due to the cross-talk filter. The decrease at high energy of both 1n and 2n efficiencies is due to the neutrons falling off the detector.

When neutrons reach the detector, their interaction with detector materials generates charged particles that will emit light. The light is then collected by the photo-multipliers. The efficiency is the ratio of neutrons that induced light in the photo-multiplier over total neutrons that reached the detector. This efficiency can be deduced experimentally by comparing, in a system that decays by an excited state of the nucleus $^{A-1}X$, the neutron-gated $\gamma$-spectrum and the non-gated one. Here we use an example of the reaction $^{13}$B(p,2p)$^{12}$Be$^{*}$ –> $^{11}$Be$^{*}$. The excited state of $^{11}$Be (320 keV above ground state) is populated by this reaction and the corresponding $\gamma$-ray is detected in Crystal Ball. Requesting the coincidence of the $\gamma$-ray with the detection of the neutron would reduce the $\gamma$-spectrum by a factor which is the efficiency of LAND. We make a gate on 0<$E_d$<3 MeV and plot $\gamma$-ray spectrum (Fig. 3.12a) which we compare with the non-gated spectrum (Fig. 3.12b). This gives the efficiency of $\epsilon_n$ = 93 $\pm$ 6% to detect a neutron in LAND.

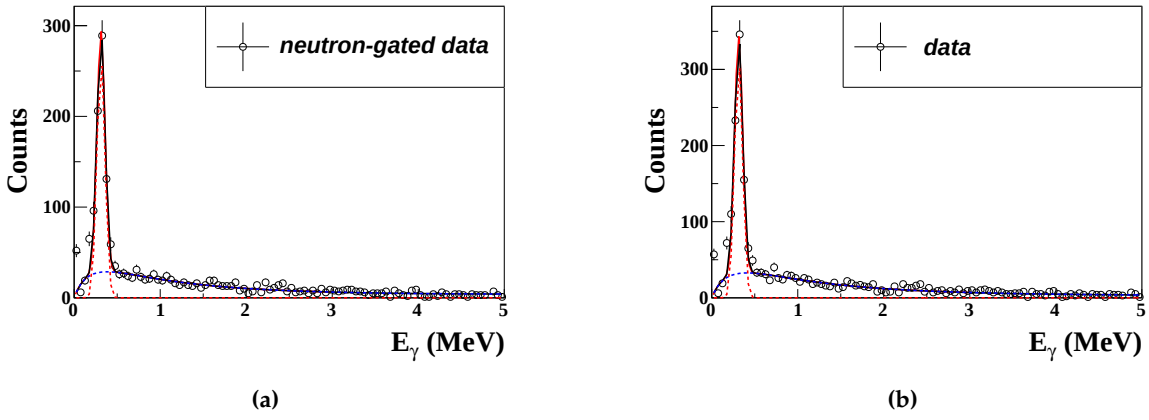


**Figure 3.12** – Using the reaction $^{13}$B(p,2p)$^{12}$Be$^{*}$ –> $^{11}$Be$^{*}$, neutron gated $\gamma$-spectrum (a) is compared to the non-gated $\gamma$-spectrum (b). The efficiency, which is the number of counts in the spectrum in (a) over that in (b) is 93% .

The total efficiency is a product of the geometrical acceptance and the probability that the neutron interacts with the detector. Fig. 3.11 shows one and two neutron(s) efficiencies as a

function of the decay energy.

## 3.5 Three-body final-state interactions

In this part, high energy three-body (fragment+n+n) unbound states are explored. In particular, we present the method of Dalitz plots [121] used for analyzing correlations in three-body systems. The method allows to use a simple model [97] and deduce nn-correlations as a function of the n-n distance and time delay between the emission of the two neutrons. As will be seen, the latter is related to the presence of fragment-n final-state interactions (FSI) in the exit channel. In principle, the present approach allows us to distinguish between simultaneous and sequential decay.

### 3.5.1 Phase space

The basic correlations are the ones imposed by energy and momentum conservation, which are independent of the nature of the particles. These correlations are given by the N-body phase space. The interaction between particles may give rise to "physical" correlations that are added to these basic ones. In this thesis, we will use an interacting three-body phase-space model developed for the analysis of triple correlations. To compare the model with experimental data, we will perform a simulation where the experimental $E_d$ distribution is used as input to generate events $\vec{p}_{f,n,n}(E_D)$ following three-body phase-space [122]. The final momenta of the three particles generated are then filtered to include all experimental effects (like energy resolution, angular acceptance, or cross-talk rejection). In order to illustrate the method used, we are using the result of the simulation for the reaction $^{13}$B(p,2p)$^{12}$Be where unbound states above the $2n$ emission threshold are populated ($E_d$ is shown in Fig. 3.13). I will describe in the following the different observables that we use in this analysis of three-body correlations.

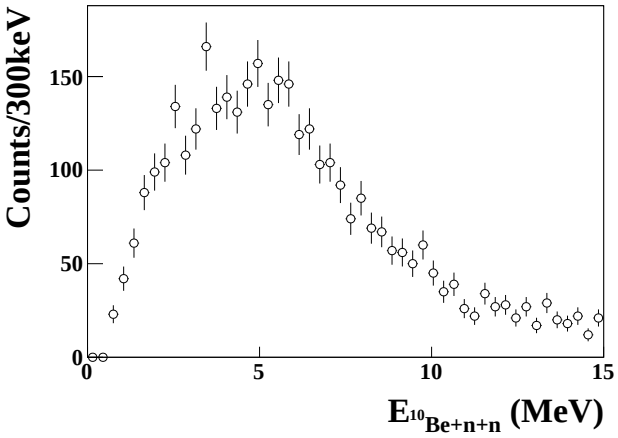


**Figure 3.13** – Experimental $E_d$ spectrum of the decay $^{10}$Be+n+n.

### 3.5.2 Dalitz Plots

The main observables that we are going to use in the study of correlations are n-n and n-fragment relative energies. The correlation between these two can be viewed using the Dalitz plots technique. This technique has been extensively used in particle physics to determine multi-particle correlations [121]. In a three-body decay as the ones investigated in this work,

the Dalitz plot can be obtained by representing the reduced fragment-neutron relative energy, $\epsilon_{fn}$, as a function of the reduced neutron-neutron relative energy, $\epsilon_{nn}$. The reduced relative energy, $\varepsilon_{ij}$ is defined as:

$$\varepsilon_{ij} = \frac{E_{ij}}{E_d} \tag{3.19}$$

These variables are normalized and range from 0 to 1, which is one of the major advantages of this method [123]. If instead of $\epsilon_{ij}$ we use directly the relative energy $E_{ij}$ variables, which can go from 0 to the $E_d$ of the event, the resulting plot will not have a definite boundary as each event presents a different value of $E_d$. The $\epsilon_{ij}$ variables are used in this thesis because it is more intuitive than the reduced invariant-mass that is commonly used for Dalitz plots. We show that using either variable amounts to the same results. Introducing the invariant-mass of the binary system as:

$$M_{ij} = m_i + m_j + E_{ij} \tag{3.20}$$

and the squared reduced mass as

$$m_{ij}^2 = \frac{M_{ij}^2 - (m_i + m_j)^2}{(m_i + m_j + E_d)^2 - (m_i + m_j)^2} \tag{3.21}$$

If we now introduce the expression of reduced relative energy, $\varepsilon_{ij} = E_{ij}/E_d$ in the equation 3.20

$$M_{ij} = m_i + m_j + \varepsilon_{ij} E_d \tag{3.22}$$

equation 3.21 becomes

$$m_{ij}^2 = \frac{(m_i + m_j + \varepsilon_{ij} E_d)^2 - (m_i + m_j)^2}{(m_i + m_j + E_d)^2 - (m_i + m_j)^2}$$

$$= \varepsilon_{ij} \frac{2(m_i + mj) + \varepsilon_{ij} E_d}{2(m_i + mj) + E_d} \approx \varepsilon_{ij} \tag{3.23}$$

In nuclear physics the masses of the particles are larger than the relative energy, *i.e.*, $2(m_i + m_j) \gg E_d$. Indeed, twice the particle masses are several GeV, while $E_d$ represents several MeV. This, together with the fact that $\varepsilon_{ij} \leq 1$, shows that the reduced energy $\varepsilon_{ij}$ can be used instead of the reduced mass $m_{ij}^2$. Fig. 3.14 shows a Dalitz plot for phase-space correlations. Since we have two neutrons involved in the decay, we fill the Dalitz plot for each event, one time for each neutron. The plot exhibits a uniform population as there is no any correlation other than the phase space. The projections over the reduced relative energies, Fig. 3.14b and 3.14c, both show a regular bell shape from 0 to 1 with a maximum at around 0.5. We can also notice that the distribution of the two variables is minimum at $\varepsilon_{ij}$ = 0 or 1.

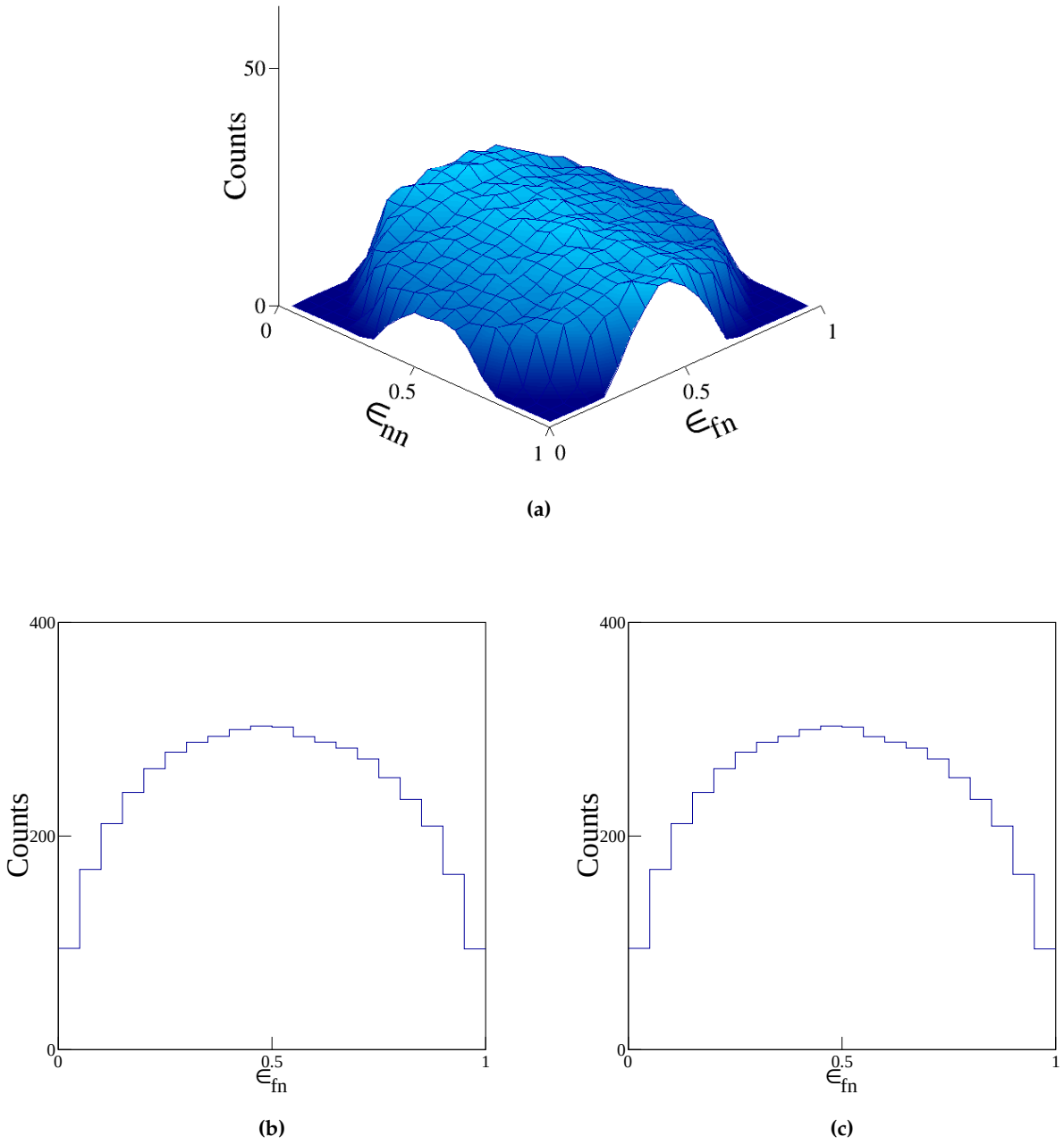


**Figure 3.14** – Simulated Dalitz plot of the $^{12}$Be+n+n phase-space decay (a), and its projections onto the reduced relative energies $\epsilon_{nn}$ (b) and $\epsilon_{fn}$ (c).

### 3.5.3 Final-state correlations

Physical correlations are seen as deviations from the phase space following a specific decay mechanism. Two decay mechanisms are possible: the direct decay, in which the two neutrons are emitted at the same time, and the sequential decay, in which one neutron is emitted first, populating a resonance in the intermediate nucleus that is decaying later (depending on the lifetime of the state) by emitting the second neutron. In either of the two decay modes, neutrons may interact with each other in the final state and give rise to characteristic correlation patterns. In order to identify $nn$ correlations in the final state, $nn$ FSI, a correlation function $C_{nn}$ can be defined from the ratio between the experimental data and the corresponding phase space:

$$C_{nn} = \frac{\sigma_{exp}(E_{nn})}{\sigma_{PS}(E_{nn})}, \tag{3.24}$$

where $\sigma_{exp}$ corresponds to the experimental distribution which contains all the interaction effects. The denominator $\sigma_{PS}$ can be obtained by the simulation of a phase-space decay. It contains all the other effects such as kinematics constraints and experimental filter. If the experimental distribution is fully described by the phase space, then $C_{nn} = 1$. On the contrary, if the interaction between particles leads to a deviation from phase space, the function will show a signal with $C_{nn} \geq 1$. We are going to look on the effect of these $nn$ FSI correlations for direct and sequential decays.

**Direct decay**

Starting with the direct decay in which the two neutrons $n_1$ and $n_2$ are emitted at the same time, the $nn$ FSI effects are added to the three-body phase-space decay simulation. To do so, we use the formalism from [97] which takes explicitly into account the influence of the distance between the two neutrons on the effects of their interaction. A simplified form of the two-particle cross-section can be expressed as

$$\sigma(E_{nn}) \sim \sigma_0(E_{nn}) \times C_{nn}(E_{nn}), \tag{3.25}$$

where $\sigma_0$ corresponds to the two-particle cross-section that the particles would exhibit if there were no influence between them and $C_{nn}$ is the correlation function that can be expressed as follows:

$$C_{nn}(E_{nn}) \sim \int W(r_{nn})F(r_{nn}, E_{nn})dr_{nn} \tag{3.26}$$

In this expression, W is the spatial distribution of the $2n$ source depending on the distance $r_{nn}$ between the neutrons and F is the correlation factor that contains the effect of the s-wave n-n FSI, as well as the effects of the Fermi statistics for identical particles (even if it is negligible in the case of nucleon pairs [97]). Here the source is considered as a Gaussian distribution. The correlation function can then be seen as a probability distribution P($E_{nn}$) to accept the event following the form of the correlation function $C_{nn}$, that depends on the space-time parameters of a Gaussian $2n$ source ($r_{nn}^{rms}$ and $\tau$). However, since in the case of a direct decay, the two neutrons are emitted at the same time, we have $\tau$=0 and therefore $C_{nn}$ only depends on the relative distance between the neutrons $r_{nn}^{rms}$. In this peculiar case, as discussed in Ref. [97], the correlation function of a Gaussian source becomes analytical. The validity of this assumption is discussed in Ref. [124] where it is shown that very different source distributions such as Gaussian, Yukawa-like, or spherical all lead roughly to similar Gaussian-like distributions for W($r_{nn}$). Moreover, in the model, internal momentum correlations in the source (W($r_{nn}$,$E_{nn}$)) are assumed to be small or to have minor impact on $C_{nn}$ after averaging over the whole source. They are therefore neglected in the present study. The fact that this formalism has been used successfully to describe in an accurate way the low energy peaks observed in the $nn$ FSI of previous works [93, 123–127] confirms the validity of the approximations made in the model.

We can now observe how the $nn$ FSI is affecting the three-body phase-space decay where the only free parameter in our simulation is the average size of the source $r_{nn}^{rms}$. We continue with the example of $^{12}$Be, i.e the $2n$ decay of $^{12}$Be into $^{10}$Be. The results for different $r_{nn}^{rms}$ on

the Dalitz plots are presented on Fig. 3.15. As we can observe, the effect of n-n FSI appears as a concentration of events at low $\epsilon_{nn}$ (<0.25), corresponding to small relative momenta between the two neutrons. We also notice that a smaller source size shows a signal with higher amplitude. On the contrary, the $\epsilon_{fn}$ variable does not seem to be affected significantly.

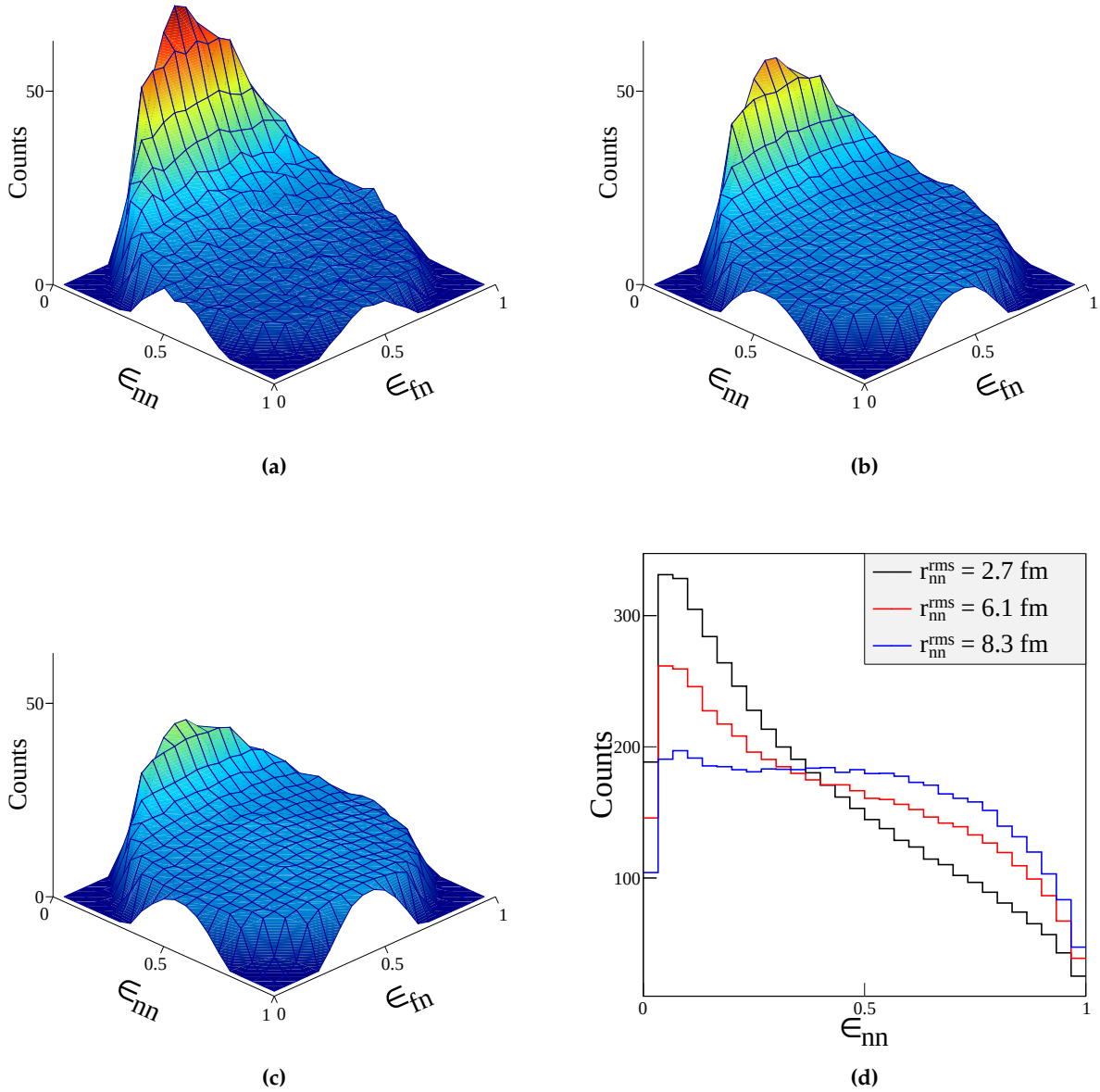


**Figure 3.15** – Simulation of the direct decay of $^{12}$Be into $^{10}$Be+n+n for 2 MeV < $E_d$ < 6 MeV. The effect of the distance between neutrons, $r^{rms}$, on the $nn$ interaction is visible at low $\varepsilon_{nn}$ in the Dalitz plot. Simulations are done for $r_{nn}^{rms}$= 2.7 fm (a), 6.1 fm (b) and 8.3 fm (c). The projections onto $\varepsilon_{nn}$ are also shown in (d).

### Sequential decay

The other decay mechanism considered is the n+n sequential decay, which corresponds to the case in which one neutron is emitted before the other. In order to simulate such a

mechanism, the events are generated following twice the two-body phase space through a fragment-n resonance of energy $E_r$ and width $\Gamma$ , followed by the interaction between the two emitted neutrons once the resonant state has decayed. In that case, the emission of the neutrons cannot be considered as simultaneous ($\tau \neq 0$) and therefore $nn$ FSI depends on the space-time parameters ($r_{nn}^{rms}$, $\tau$). As discussed in Ref. [97], this leads to the fact that $C_{nn}$ is not analytical anymore. We are then left with four parameters: $r_{nn}^{rms}$, $\tau$, $E_r$ and $\Gamma$. As it has been shown in Ref. [126], the number of parameters can be reduced to three by linking the emission time of the second neutron with the lifetime of the fragment-n intermediate resonance:

$$\tau = \frac{\hbar c}{\Gamma} \tag{3.27}$$

In this case, the only free parameters of the sequential decay are $r_{nn}^{rms}$, $E_r$ and $\Gamma$. The results of the sequential $2n$-decay simulation $^{12}$Be into $^{10}$Be+n+n for a resonance at $E_d$=6 MeV are presented in Fig. 3.16. We can observe that the sequential decay is characterized by ridges on the Dalitz plot and by double-humped structures in the projection over $\epsilon_{fn}$ (except when the centroid of the resonance is in the middle of the decay energy range (Fig. 3.16c)). Since we fill up two times the $\epsilon_{fn}$ histogram, one time for each neutron $n_1$ and $n_2$, we observe two symmetric wings in Fig. 3.16d as $\epsilon_{fn_1} \approx$ 1-$\varepsilon_{fn_2}$. The position of the wings is directly related to their energies, $E_{fn}$, compared to the maximum energy ($E_d$) available in the system.

The wings in the $\epsilon_{fn}$ variable are broad if the resonance is broad. In such a case, since $\Gamma \sim 1/\tau$, it means that the resonance lives for a short time before decaying, leaving the possibility for the two neutrons to interact in the final state. We can conclude by saying that $nn$ FSI are revealed by the $\epsilon_{nn}$ observable and that the $\epsilon_{fn}$ variable is sensitive to the sequential decay mechanism. Therefore, using a two-dimensional analysis, we can have access to information on the decay mechanism involved in the reaction. These Dalitz plots will be used in the following chapter, together with the fit of the fragment-neutron relative-energy spectra in order to study the structure of states in $^{12}$Be.

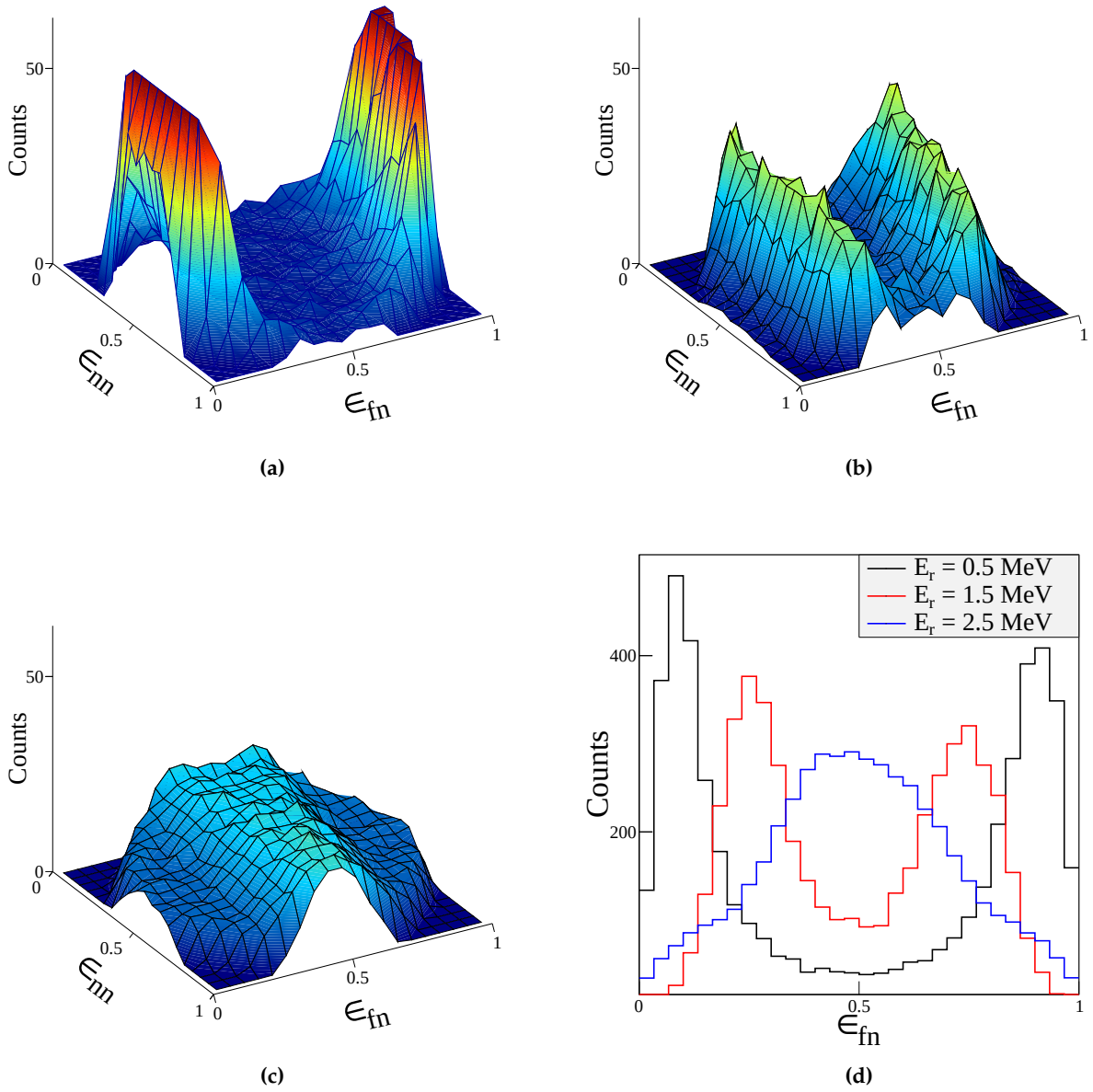


**Figure 3.16** – Dalitz plot of the sequential decay of $^{12}$Be ($E_d$ = 6 MeV) into $^{10}$Be+n+n through two different intermediate states: a low energy state at $E_r = 0.5$ MeV (a), at $E_r = 1.5$ MeV (b) and at $E_r = 2.5$ MeV (c). The projections onto $\varepsilon_{fn}$ (d) show the differences in shape depending on the energy of the intermediate state.

# Spectroscopy of $^{12}$Be



In this chapter, I present the results on $^{12}$Be spectroscopy from the $^{13}$B($-$1p)$^{12}$Be reaction. In this reaction, we expect to populate mainly $0^+$ and $2^+$ states, as we shall see below. Since $^{13}$B is a spherical nucleus ($N = 8$ shell is closed [56]), states in $^{12}$Be that have a spherical component will be preferentially populated. However, due to mixing, different states with various configurations are observed in this experiment, and their structure could be revealed from their population rates, cross-sections (or spectroscopic factors) and decay patterns. Thanks to the complete measurement of the kinematics, we can study bound and unbound states of $^{12}$Be via their $\gamma$, 1n and 2n decays. First, the expected states of $^{12}$Be from the $^{13}$B($-$1p)$^{12}$Be reaction will be presented. Then, we will see the populated bound and unbound states of $^{12}$Be by analysing $\gamma$, 2-body and 3-body energy spectra. I conclude with a discussion of the results obtained.

## 4.1 $^{12}$Be states populated by the $^{13}$B($-$1p) reaction

Let us first look at states that are expected to be populated in the $^{13}$B($-$1p)$^{12}$Be reaction. The 5 protons of $^{13}$B are distributed in the two first shells, $1s_{1/2}$ and $1p_{3/2}$, with the last one containing 3 of them (a closed $1p_{3/2}$ orbital would contain 4 nucleons). Removing one proton in the $p_{3/2}$ shell leads to the formation of $0^+$ and $2^+$ states (Fig. 4.1). These states will be of mostly spherical configuration since the neutron orbitals up to $N = 8$ ($1s_{1/2}$, $1p_{3/2}$ and $1p_{1/2}$) are normally filled in $^{13}$B. Intruder configurations with $0^+$ and $2^+$ can be obtained from the

weak components in which neutrons are filling the the upper orbitals ($2s_{1/2}$ and $1d_{5/2}$) in $^{13}$B. While the removal of the proton in the $1p_{3/2}$ orbital always leads to positive parity states, the removal of a proton from the deeply bound $1s_{1/2}$ orbital gives rise to negative parity states, $1^-$ and $2^-$. These states are expected to lie at very high excitation energy, since removing the proton in the inner shell costs more energy. Typically, broad states arising from the $1s_{1/2}$ proton removal seem to be identified around excitation energy E$^*$ = 19MeV in $^{11}$Be using the $^{12}$C(e,e'p) or (p,2p) reaction [128]. From the work of V. Panin in which the (p,2p) reaction was used (Ref. [100]), contributions from the $1s_{1/2}$ removal seem to start around E$^*$ = 15MeV

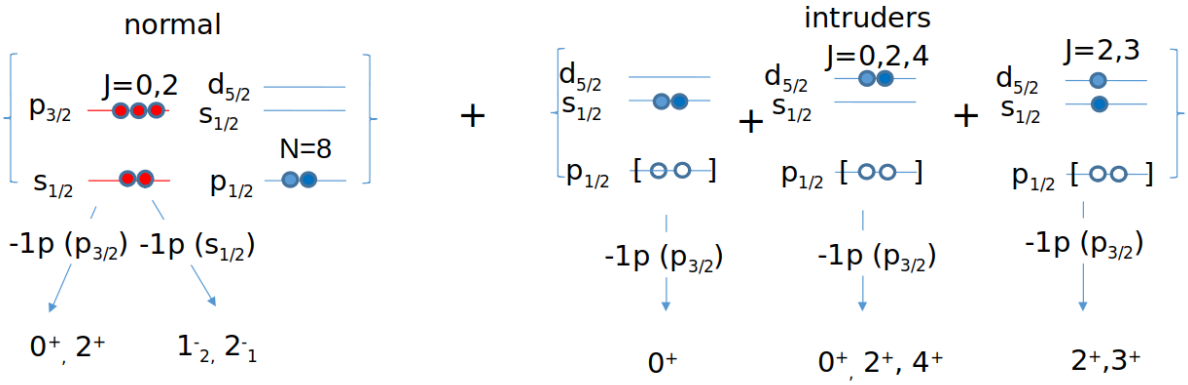


**Figure 4.1** – States of $^{12}$Be expected to be populated from the $^{13}$B$(-1p)^{12}$Be reaction. We see a predominance of $0^+$ and $2^+$ states. Normal configuration (closed $N = 8$ shell) of $^{13}$B leads to spherical states while intruder configurations lead to deformed ones. Negative parity states, $1^-$ and $2^-$, can also be populated at very high energy by knockout of deeply-bound proton in the $1s_{1/2}$ orbital.

In Ref. [56], the neutron configuration of $^{13}$B, i.e. the occupancy of the neutron *p*- and *sd*-orbitals, was determined by using the $^{13}$B$(-1n)^{12}$B reaction and by looking at the cross-sections to positive and negative-parity states of $^{12}$B. The results showed that the *sd*-orbitals contribute to 12 $\pm$ 1% of the ground state of $^{13}$B. The dominant configuration is then the *p*-shell closure, with contribution of 88 $\pm$ 4%. The proton-knockout reaction from $^{13}$B in normal configuration (*p*-shell closure) will lead to spherical states of $^{12}$Be, whereas the intruder configurations will lead to deformed states. The observed states of $^{12}$Be will be the results of the mixing of these spherical and deformed configurations.

Let us denote the spherical and deformed states before the mixing by $\phi_S$ and $\phi_D$, respectively, with D=1...N for N deformed states. The observed states in $^{12}$Be after mixing, $\psi$, can be written as a superposition of states with pure spherical and deformed configurations:

$$\psi = \alpha_S \times \phi_S + \sum_{D=1}^{N} \beta_D \times \phi_D \tag{4.1}$$

Where $\alpha_S$ and $\beta_D$ are coefficients fulfilling the condition $\alpha_S^2 + \sum_D \beta_D^2 = 1$.

Depending on the structure of the deformed components, we might observe spherical, cluster or halo states, giving rise to shape coexistence. In this context, a theoretical study of

states in $^{12}$Be using the Anti-symmetrized Molecular Dynamics (AMD) calculations [63] predicted coexistence of spherical and cluster states. In the following sections we are going to study all states that were populated, bound and unbound.

Bound states are studied by fitting the $\gamma$-ray spectrum and counting the $^{12}$Be fragments, while 1n and 2n unbound states are studied by fitting the $E_d$($^{11}$Be+1n) and $E_d$($^{10}$Be+2n) spectra, respectively. Thereafter, we will deduce the cross-section and spectroscopic factors of these states and compare them with theoretical predictions.

## 4.2 Bound states of $^{12}$Be

Let us begin this spectroscopic study of $^{12}$Be by its bound states. The ground state $0^+_1$ has been thoroughly studied, both theoretically [63] and experimentally [69, 137–141]. It was shown that its configuration involves neutron excitation to the 2$s$-1$d$ orbitals. Its study by one neutron knockout [69] showed a mixing of the spherical configuration (closed $N = 8$ shell), with only 25% of the strength, and intruder configurations $2s_{1/2}$ and $1d_{5/2}$ of about 25 % and 50% respectively. The second known state is the $2^+_1$ at 2.1 MeV, which was studied by the $^{10}$Be(t,p)$^{12}$Be reaction [142] and inelastic scattering [67, 78]. In Ref. [142], this state was also shown to be dominated by the intruder 2$s$-1$d$ configuration. Another $0^+$ state, at 2.25 MeV, was found to be an isomeric state [170] with a lifetime of $\tau$ = 331 $\pm$ 12 ns. Its configuration was theoretically predicted [144] and experimentally determined to be a mixture of 1$p$-2$s$-1$d$ shells, with 60 %, 39 % and 2 % of the strength, respectively.

From the present work, we expect to populate the ground state of $^{12}$Be and the two first excited states, $2^+_1$ and $0^+_2$, as they contain some fraction of the spherical configuration. The $2^+_1$ state, if populated, would be identified by the detection of its deexcitation $\gamma$-rays. However, the delayed $\gamma$-ray decay from the $0^+_2$ would not be observed because our experimental apparatus was not designed to distinctly detect isomeric states. In fact, due to the relatively long lifetime of an isomeric state, the $\gamma$-ray decay rarely occurs around the target but much further away. It results in a much reduced efficiency and, if detected, a wrong Doppler energy correction. Therefore, if the two $0^+$ states are populated through the reaction $^{13}$B($-$1p)$^{12}$Be, we will not be able to distinguish them by $\gamma$-ray detection. The last known bound state of $^{12}$Be is the $1^-$ state [67,68,77,145]. This state is a pure intruder, resulting from the excitation of a neutron in the $1p_{1/2}$ shell leading to a particle-hole configuration $(1s_{1/2})^1(0p_{1/2})^{-1}$. The fact that this state is not observed in the $^{13}$B(p,2p)$^{12}$Be reaction is in line with the very weak fraction of $(2s_{1/2})^2$ intruder(less than 1%) extracted from the analysis of the $^{13}$B(p,pn)$^{12}$B reaction [56].

**Table 4.1** – Known bound states of $^{12}$Be that are listed in Ref. [128]. Only the three first states are expected to be populated from the $^{13}$B$(-1p)^{12}$Be reaction. The two $0^+$ states will be seen as one since the $0^+_2$ is an isomeric state. The $1^-$ state is not expected to be populated from spherical $^{13}$B since it is of purely neutron intruder configuration.

| $J^\pi$ | $E^*$ (keV) | $T_{1/2}$ |
|---|---|---|
| $0^+$ | 0 | 21.46 (5) ms |
| $2^+$ | 2109 (1) | 0.957 (19) ps |
| $0^+$ | 2250 (1) | 331 (12) ns |
| $1^-$ | 2715 (15) | 1.3 (4) fs |

I present the fit of the $\gamma$-spectrum (see the fit procedure in Sect. 3.3) for the two targets, $CH_2$ and C, separately (Fig. 4.2) so that we can use them to deduce the reaction rate on a H target. Both spectra show one photopeak that we fit by a Gaussian function (in red in Fig. 4.2) whose width is fixed by the resolution of the XB detector (Sect. 3.3.2). The results show that the photopeak is centered at 2.08±0.03 MeV, corresponding to the first excited state of $^{12}$Be, $2^+_1$. The counting of events for this state is done by integrating the Gaussian function and correcting the counts by $\gamma$-ray efficiency ($\epsilon_\gamma$(2080 keV) = 29±9 %, see Sect. 3.3.3). The summed population of the $0^+_1$ and $0^+_2$ states from the reaction is determined by subtracting the $2^+_1$ events from the inclusive bound states cross-section. The latter is identified by the detection of the fragment of $^{12}$Be in TFW, a detection of two protons in XB (with a simulated efficiency of $\epsilon_{2p}$ = 56±2%, from Refs. [99, 100]) and without any condition on the $\gamma$-ray detection. The condition of detecting 2p reduces the counts and we need to take this into account by correcting by the 2p-efficiency. Tab. 4.2 reports the number of events corresponding to bound states. As expected, the purely intruder state $1^-$ was not observed within the statistical significance from the $\gamma$-ray spectra in Fig. 4.2.

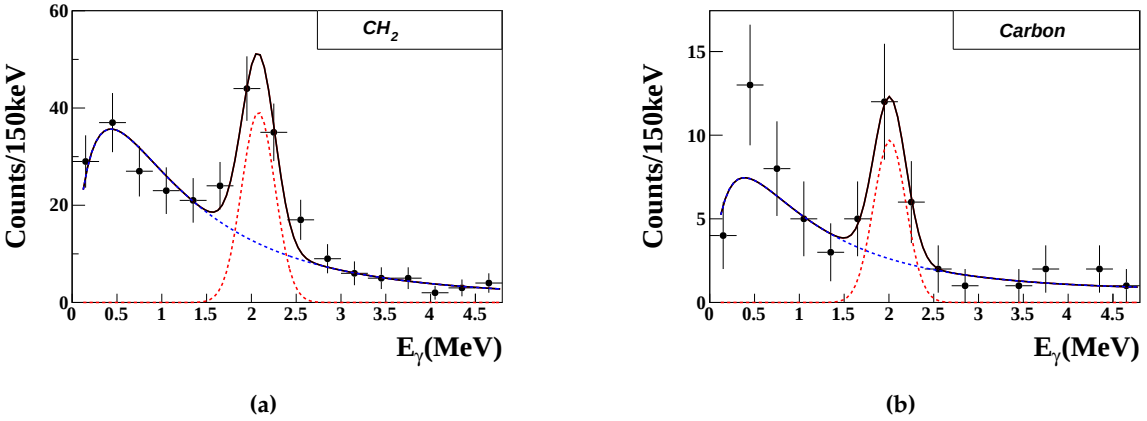


**Figure 4.2** – Spectra of $\gamma$-rays emitted in coincidence with the fragment of $^{12}$Be. For both $CH_2$ (a) and Carbon (b) targets, we observe an excited state of $^{12}$Be at 2.08 MeV corresponding to the $2^+_1$ state.

**Table 4.2** – Number of events for the bound states of $^{12}$Be given in the $1^{st}$ column. The $2^{nd}$ and $3^{rd}$ columns represent the number of events after correction by $\gamma$- and 2p-efficiencies for the $CH_2$ and C targets, respectively.

| States | $CH_2$ | C |
|---|---|---|
| Inclusive | $3552 \pm 59$ | $1088 \pm 33$ |
| $0^+_{g.s}$ and $0^+_2$ | $3394 \pm 21$ | $1030 \pm 20$ |
| $2^+_1$ | $158 \pm 12$ | $58 \pm 8$ |

The number of detected $^{12}$Be, in the ground or excited states (Tab. 4.2), will be used later when calculating cross-sections. The uncertainties come from an error propagation from statistical errors and uncertainty on the $\gamma$-efficiency, when applicable (as for the $2^+_1$ state).

## 4.3 Study of 1n resonant states

Unbound states of $^{12}$Be are seen at relatively low excitation energy because the one and two-neutron emission thresholds are low, 3170 keV and 3670 keV respectively. We notice also that these thresholds are close to each other, only separated by 500 keV. While all known unbound states of $^{12}$Be are above not only the 1n-emission threshold but also the 2n-emission threshold, one resonance at 4412 keV was previously seen to decay to $^{11}$Be by emitting one neutron [95]. In that study, they used the $^{13}$B$(-1p)^{12}$Be reaction to populate this state and the invariant-mass method to study its decay. For this purpose, only neutrons were detected in coincidence with $^{11}$Be and $^{10}$Be fragments. Decay branches suggested an upper limit of 5% decay to the ground state of $^{10}$Be by two-neutron emission. As we shall demonstrate in the following, this state corresponds to the previously observed resonance at 4559 keV [145] and at 4580 keV [77], at variance with the discussion made in Ref. [95] to argue that they were different. In fact, the disagreement in the observed centroid-energy between Refs. [77, 145] and [95] is because, as we shall demonstrate, the decay occurs both to the ground and excited states of $^{11}$Be. In the following we are going to study states of $^{12}$Be populated by the $^{13}$B$(-1p)^{12}$Be reaction (same as in Ref. [95]) using neutron, $\gamma$ and $^{11}$Be fragment detection. We will then be able to determine the branching ratios to both ground and excited states of $^{11}$Be.

The $E_d(^{11}\text{Be}+1n)$ and $\gamma$-ray spectra will be fitted in order to determine energy, width and decay channels of the resonance that was populated in $^{12}$Be. The $\gamma$-ray spectrum shows a photopeak at 320 keV, indicating the decay on the excited state of $^{11}$Be. The energy of the resonant state in $^{12}$Be is determined by looking at the $E_d(^{11}\text{Be}+1n)$ spectrum in coincidence with $\gamma$-rays, i.e. by gating around the photopeak ($250 < E_\gamma < 450$ keV). In this $\gamma$-energy range, the photopeak lays on top of a background, and therefore the $E_d(^{11}\text{Be}+1n)$ spectrum gated on this range includes a background contamination that has to be removed. We estimate it by gating on the right part of the $\gamma$-ray spectrum after the photopeak, $700 < E_\gamma < 3000$ keV (blue dots in Fig. 4.3b). The subtraction of these two spectra leads to the actual $\gamma$-gated $E_d(^{11}\text{Be}+1n)$ spectrum (Fig. 4.3c) which is fitted by an $\ell$-dependent Breit-Wigner function, as described in Sect. 3.4.2.

The result of the fit gives a decay energy and a width of the resonance $E_d$ = 1100 keV and $\Gamma_r$ = 400 keV. This energy is shifted towards lower energies by $E_\gamma$=320 keV, hence the energy

of the resonance in $^{12}$Be is given by:

$$E_r = E_d + E_\gamma = 1100 + 320 = 1420 \text{ keV}$$

The uncertainties on the values of energy and width are due to the fit method. We estimate them by making different gates around the photopeak and also drawing the $\chi^2$ graph (Fig. 4.3d) which shows the goodness of the fit. The best fit corresponds to the minimum value $\chi^2_{best}$, and the uncertainties on the energy and width are obtained by making the condition $\chi^2_{best}$ - $\Delta\chi^2 < \chi^2 < \chi^2_{best} + \Delta\chi^2$. The value of $\Delta\chi^2$ is a function of the confidence interval and the number of degrees of freedom (4 parameters in our case). With these uncertainties taken into account we get $E_r$ = 1420 $\pm$ 50 keV and $\Gamma_r = 400^{+100}_{-50}$ keV for the energy and width of the resonance.

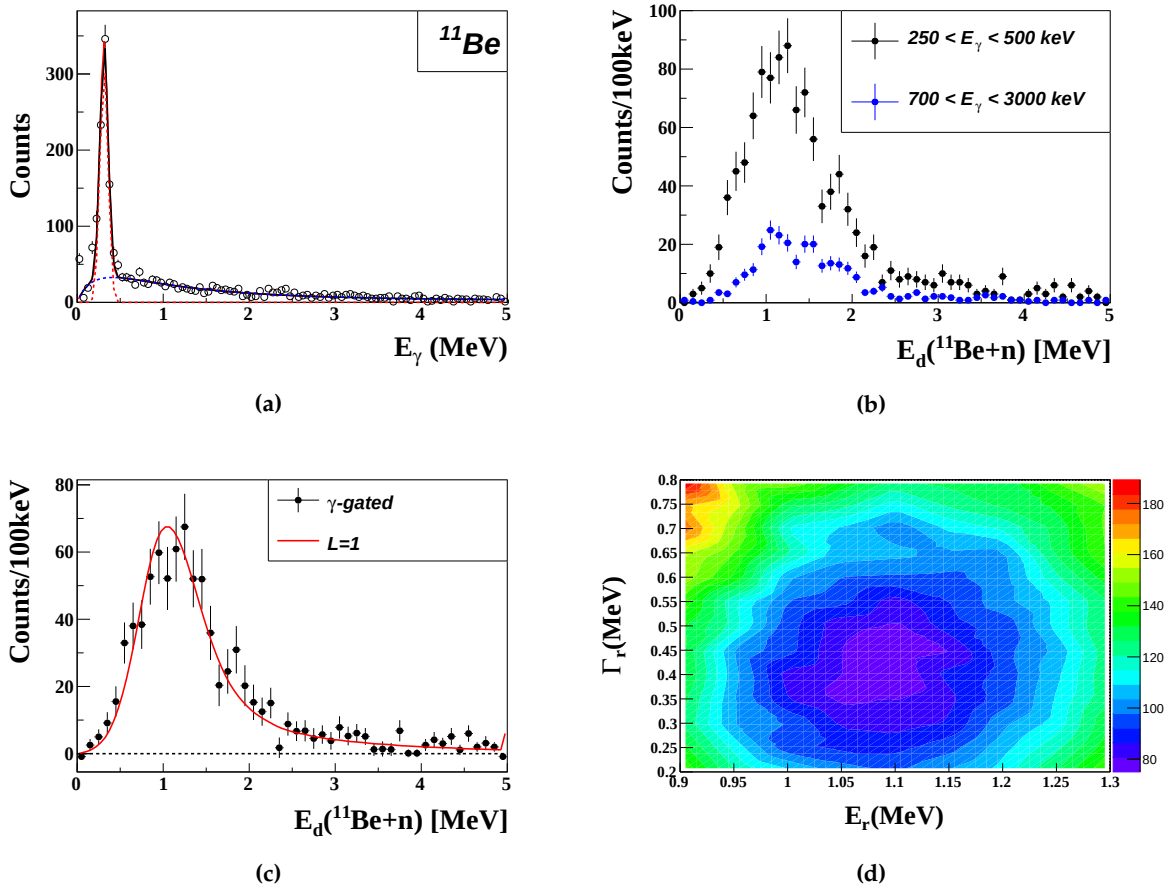


**Figure 4.3** – (a): Fit of the $\gamma$-ray spectrum (at multiplicity M=1) showing a photopeak at 320 keV, which corresponds to the known excited state of $^{11}$Be. (b): $E_d$($^{11}$Be+1n) spectra gated on 250 < $E_\gamma$ < 450 keV (black) and 700 < $E_\gamma$ < 3000 keV (blue). The latter is used for background estimation. (c): $\gamma$-gated $E_d$($^{11}$Be+1n) spectrum after background subtraction fitted by an $\ell$=1 Breit-Wigner function. (d): 2-dimensional $\chi^2$ graph from the fits of the energy and width of the resonance.

As mentioned before, the fit function is an $\ell$-dependent Breit-Wigner. This property can allow us to estimate the parity and/or spin of the initial resonance before decay. The best fit is given by $\ell$ = 1 (Fig. 4.3c, $\chi^2_{norm}$ = 1.29), as compared to the fits with $\ell$ = 0 (4.4a) and $\ell$ = 2 (4.4b). By looking at the normalised $\chi^2$ value, we can only rule out $\ell$ = 2 ($\chi^2_{norm}$ = 2.2) as $\ell$ = 0

fits also reasonably well ($\chi^2_{norm}$ = 1.35) the data. However, we propose to keep the value of $\ell$ = 1 (rather than $\ell$ = 0) for the following reasons:

1. $\ell$ = 0 would imply, when considering a dominating decay to the $1/2^-$ state of $^{11}$Be a negative parity of the 1420 keV resonance. As said earlier (see also Fig. 4.1), this would imply a proton $1s_{1/2}$ removal, which is very unlikely at such low excitation energy.

2. The energy of this resonance, obtained by adding the $\gamma$-ray energy to the decay energy, $E_r$ = 1420(50) keV (Eq. (4.2)) matches within the uncertainties, the one obtained in Ref. [77], $E_r$ = 1410(5) keV which was assigned to spin-parity $2^+$.

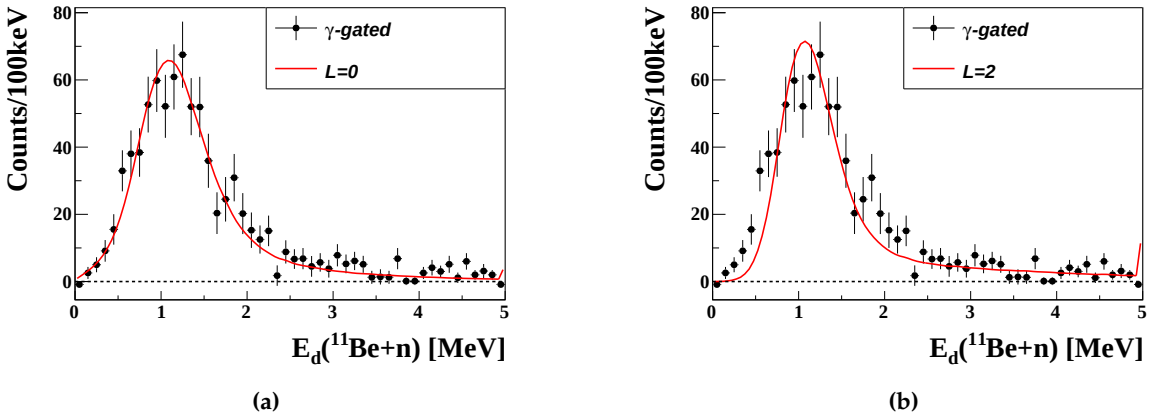


**Figure 4.4** – Fit of the $\gamma$-gated $E_d(^{11}Be+1n)$ spectrum with $\ell$=0 (a) and $\ell$=2 (b) Breit-Wigner functions.

We can then conclude from the above arguments that the two resonances observed previously at 4412(16) keV [95] and at 4580(5) keV [77] indeed correspond to the same state in $^{12}$Be. Indeed, from our work, the excitation energy of this state is given by:

$$E_{exc} = S_n + E_r = (3170 \pm 19) + (1420 \pm 50) = 4590 \pm 160 \text{ keV}$$

This resonance can also decay to the ground state of $^{11}$Be with a decay energy of $E_d$=1420 keV and $\ell$ = 2. We determine the branching ratios for the decay to ground and excited states of $^{11}$Be by fitting the total $E_d(^{11}Be+1n)$ spectrum. The fit function is a sum of two Breit-Wigner having the same width ($\Gamma_r$=400 keV) as coming from the same resonance, with the following parameters: BW1 (E=1100 keV and $\ell$ = 1) and BW2 (E=1420 keV and $\ell$ = 2). In the fit procedure only the amplitudes are variable with the shift between the two centroid energies set at 320 keV. The result of the fit shows that the resonance decays by 62 $\pm$ 2% on the excited state and 38 $\pm$ 2% on the ground state.

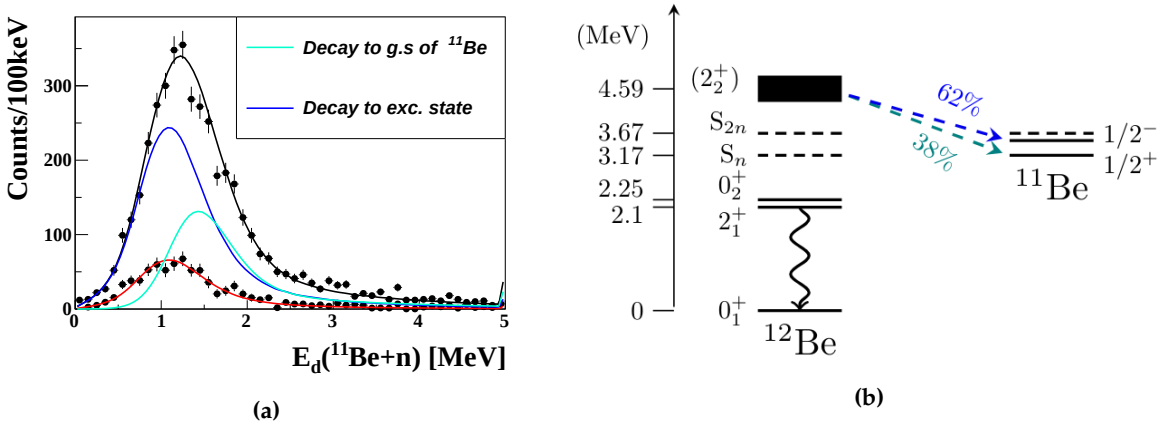


**Figure 4.5** – (a): Fit of the total $E_d(^{11}Be + 1n)$ spectrum with a sum of two Breit-Wigner functions. Cyan and blue lines correspond to the decay to the ground and excited states of $^{11}$Be, respectively. The $\gamma$-gated spectrum and its fit (red line) are also shown. (b): A level scheme illustrates the deduced decay patterns.

Remembering that the $\gamma$-gated spectra are reduced by a factor which corresponds to the $\gamma$-ray efficiency, we can deduce it at 320 keV by comparing the amplitude of BW1 (blue line in Fig. 4.5a) to the $\gamma$-gated spectrum (red line in Fig. 4.5a). In order to estimate the uncertainties of the $\gamma$-efficiency obtained by this method, we gate on different ranges around the photopeak and for different background estimations. In Tab. 4.3 we report the results obtained using different gates. The efficiency of 29.0 $\pm$ 3.6% corresponds to the mean value, which has been used to determine the scaling factor of the $\gamma$-efficiency curve in Sect. 3.3.3.

**Table 4.3** – Values of $\gamma$-efficiency using different cut ranges in the $^{11}$Be+n energy spectrum.

| Range (MeV) | 0.250 - 0.400 | 0.250 - 0.500 | 0.150 - 0.400 | 0.150 - 0.500 |
|---|---|---|---|---|
| $\epsilon_\gamma$ ( % ) | 24.0 $\pm$ 3.7 | 29.0 $\pm$ 3.0 | 30.0 $\pm$ 3.5 | 34.0 $\pm$ 4.0 |

The number of events corresponding to this $2_2^+$ state is obtained by integrating the $E_d(^{11}Be+1n)$ spectrum and correcting it by the neutron efficiency (93 $\pm$ 6%, Sect. 3.4.3). The values for the two targets are listed in Tab. 4.4. We notice that this state is much more populated compared to the $2_1^+$ state (see Tab. 4.2), which gives a hint on the predominance of the spherical component in it.

**Table 4.4** – Number of events corresponding to the $2_2^+$ state obtained by integrating the $E_d(^{11}Be+1n)$ spectrum and corrected by the neutron efficiency.

| | $CH_2$ | C |
|---|---|---|
| $2_2^+$ | 3413 $\pm$ 58 | 1696 $\pm$ 41 |

As this state is 920 keV above the 2n emission threshold, it can in principle also decay to $^{10}$Be by 2n emission. To determine the branching to this channel we are going to analyse the $E_d(^{10}Be+2n)$ spectrum in the next section. Beyond the $2_2^+$ state, no other resonance has been observed by 1n decay despite the good acceptance of the neutron detector (see Fig. 3.11). Since all the known unbound states of $^{12}$Be are above the 2n-emission threshold, they could all be 3-body systems that decay by emitting two neutrons and a fragment of $^{10}$Be.

## 4.4 Study of 2n resonant states and their decay

The detection of two neutrons in coincidence with a fragment of $^{10}$Be allows us to reconstruct the 3-body energy spectrum $E_d(^{10}Be+2n)$ (Fig. 4.6a) by the invariant-mass method described in Sect. 3.4.1. It contains contributions from resonances in the continuum that are usually intrinsically broad, and appear even broader given the energy resolution of the detectors (see Sect. 3.4.3). Their contributions must be separated, which will be achieved using the strategy described below.

### 4.4.1 Fitting procedure for the 2n-decay spectrum

We will fit the fragment-1n energy spectrum $E_d(^{10}Be+1n)$ rather than the 3-body one, $E_d(^{10}Be+2n)$. This choice is made because the $E_d(^{10}Be+1n)$ spectrum may have more structures, due to the decay channels involved, that we can fit by assuming the population of the known states of $^{12}$Be, especially those identified as $0^+$ and $2^+$ in the literature. To complete the information contained in the $E_d(^{10}Be+1n)$ spectrum, we also use the spectrum of $\gamma$-rays (Fig. 4.6b) detected in coincidence with two neutrons and a $^{10}$Be fragment. The fit of the total $\gamma$-ray spectrum shows two $\gamma$-transitions at 3368 and 2590 keV, corresponding to the two first excited states in $^{10}$Be, $2_1^+$ and $2_2^+$ respectively. In fact, the $2_2^+$ in $^{10}$Be decays by a cascade of two $\gamma$-rays of energies 2590 keV (transition to $2_1^+$) and 3368 (transition from $2_1^+$ to the ground state $0_1^+$). The detection of these $\gamma$-rays suggests that high-energy resonances in $^{12}$Be decay via excited states of $^{10}$Be and are seen at lower energies in the $E_d(^{10}Be+2n)$ spectrum, where only the energy of the neutrons is considered.

When the two neutrons are emitted simultaneously, the $E_d(^{10}Be+1n)$ spectrum has a bell-like shape from 0 to the resonance energy, and the latter cannot be deduced so precisely. On the contrary, when the two neutrons are emitted sequentially, one sees two structures in the $E_d(^{10}Be+1n)$ spectrum which correspond to:

- The first neutron emitted between the resonant state in $^{12}$Be and the intermediate resonance in $^{11}$Be, with relative energy $E_{n1}$.
- The second one, with relative energy $E_{n2}$, emitted between the intermediate resonance in $^{11}$Be and either the ground state or an excited state of $^{10}$Be.

The sum of the relative energies of the two neutrons corresponds to the total energy of the resonance in $^{12}$Be, $E_r(^{12}Be) \sim E_{n1}+E_{n2}$ if the decay occurs to the ground state of $^{10}$Be. Conversely, if the decay passes through an excited state of $^{10}$Be, we also add the corresponding $\gamma$-ray energy to get the resonance energy, $E_r \sim E_{n1}+E_{n2}+E_\gamma$. We will also deduce the proportion of direct and sequential decay in each range of decay energy, and eventually for each resonant state of $^{12}$Be.

In the following we are going to cut the $E_d(^{10}Be+2n)$ spectrum in different ranges and fit the corresponding $E_d(^{10}Be+1n)$ spectra by simulations. A difference in structures of the $E_d(^{10}Be+1n)$ can be seen between different ranges (Fig. 4.7). From the fit we will deduce the energy and width of populated resonances together with the proportions of sequential and simultaneous emission of the two neutrons, which will be then used when studying n-n correlations using Dalitz plots.

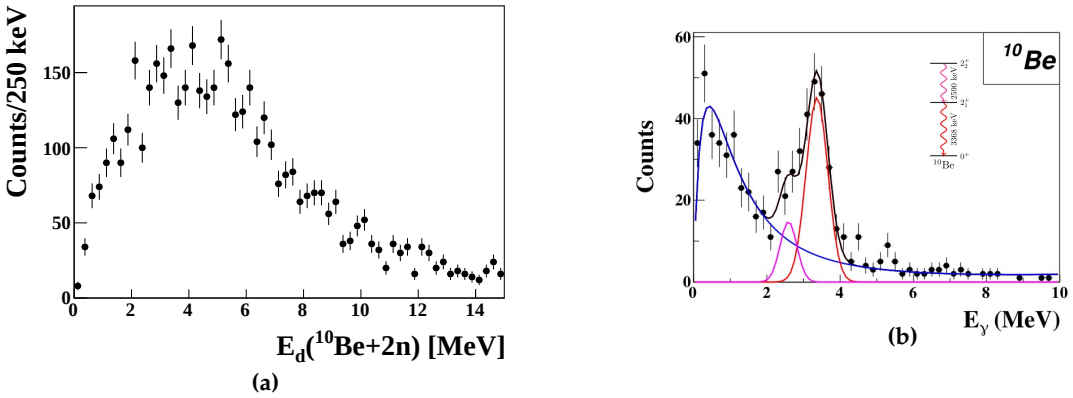


**Figure 4.6** – The $E_d(^{10}Be+2n)$ spectrum (a) cannot be fitted directly as it exhibits no obvious structure. The $\gamma$-ray spectrum (b) indicates that some resonances decay via the first excited $2^+$ states of $^{10}$Be.

The selection of the 3-body energy ranges is guided by possible decay channels, i.e. available intermediate resonances in $^{11}$Be for a given range in $E_d(^{10}Be+2n)$, and also by making sure that we have enough statistics in each range. For example, the ranges from 2 to 3 MeV and from 8 to 15 MeV will have comparable statistics (see Fig. 4.7b and 4.7d) due to the decrease of efficiency at high energies. We also make use of the $\gamma$-ray spectrum to determine and constrain the proportions of the decay to excited states of $^{10}$Be.

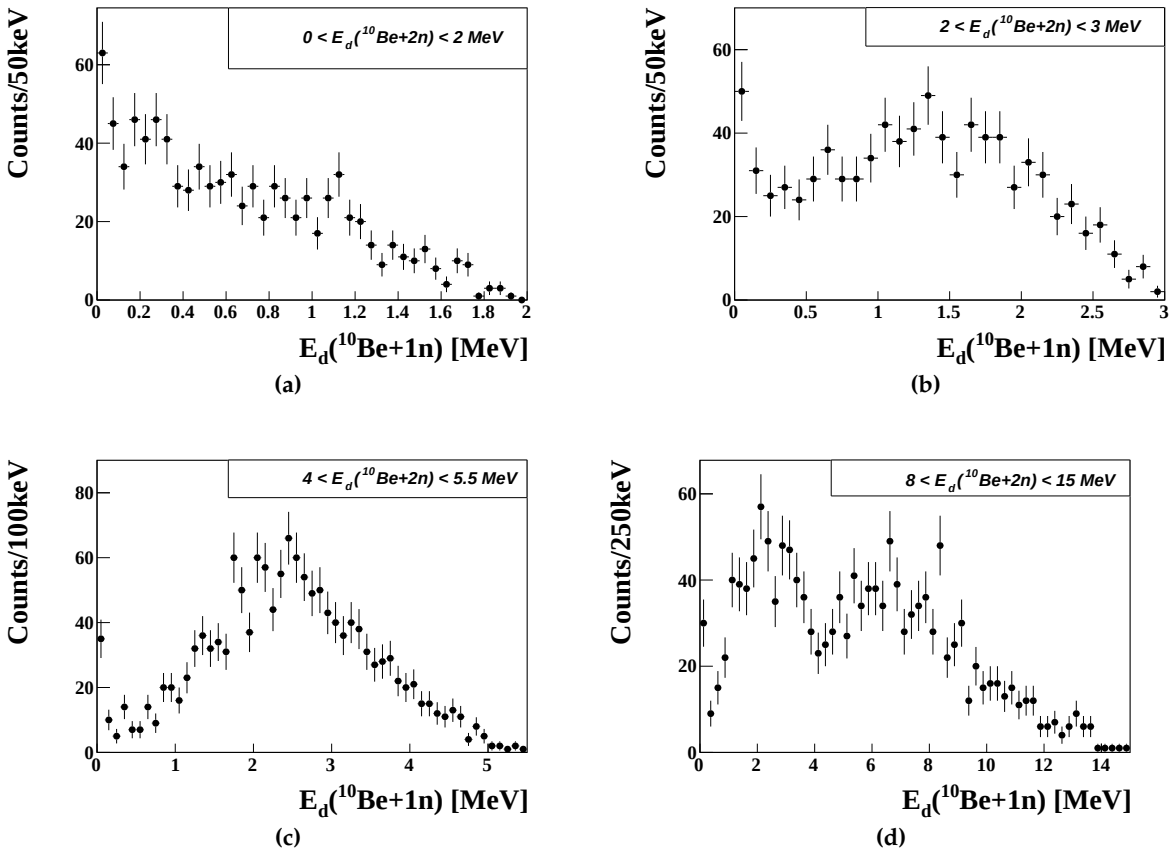


**Figure 4.7** – $E_d(^{10}Be+1n)$ spectra corresponding to the ranges in $E_d(^{10}Be+2n)$ from 0 to 2 MeV (a), 2 to 4 MeV (b), 4 to 5.5 MeV (c) and 8 to 15 MeV (d).

There exist known states in $^{11}$Be and $^{12}$Be, which we propose to review first briefly. The first unbound state of $^{11}$Be is the $5/2^+$ at 1783 keV excitation energy [128], i.e. 1283 keV above the ground state of $^{10}$Be. This opens up the possibility for high-energy resonances in $^{12}$Be to decay sequentially through this intermediate state in $^{11}$Be. Other unbound states of $^{11}$Be were studied in Refs. [130, 154–159]. Among these, the doublet of states $3/2^-$ and $5/2^-$ at $E^*$= 3889 and 3949 keV may decay to the excited $2_1^+$ state of $^{10}$Be by emitting a neutron of relative energy of 20 and 80 keV, respectively. The latter channel has been identified in Ref. [130]. The $5/2^-$ could as well decay through the same state by emitting a neutron of relative energy of 20 keV. The $\gamma$-ray coincidence will be used to identify which resonance decay to the excited states in $^{10}$Be. We summarize in Tab. 4.5 the known states of $^{12}$Be that will be used in the fit procedure.

**Table 4.5** – A non exhaustive list of known unbound states of $^{12}$Be [128] and their possible decay channels to $^{10}$Be. From left to right, the spin-parity, the excitation energy, the decay energy towards the given state in $^{10}$Be, and the width. When the width is not known (which is the case for many of them), it will be set as a free parameter in the fit of the $E_d$($^{10}$Be+2n) spectrum.

| $J^\pi$ | $E^*$ (keV) | $E_d$ (keV) | state in $^{10}$Be | $\Gamma_r$ (keV) |
|---|---|---|---|---|
| $2_2^+$ | 4590 ±50 | 920 | $0^+$(g.s) | 400 |
| - | 6275 ± 50 | 2605 | $0^+$(g.s) | - |
| $(2^+)$ | 7200 ± 1 | 3530 | $0^+$(g.s) | - |
| - | 8230 | 4560 | $0^+$(g.s) | - |
| | | 1192 | $2_1^+$ | |
| - | 9300 | 5630 | $0^+$(g.s) | 2000 |
| | | 2262 | $2_1^+$ | |
| $0^+$ | 10800 | 7130 | $0^+$(g.s) | - |
| | | 3762 | $2_1^+$ | - |
| $2^+$ | 11800 | 8130 | $0^+$(g.s) | 1000 |
| | | 4762 | $2_1^+$ | - |
| | | 2172 | $2_2^+$ | - |
| - | 14800 | 11130 | $0^+$(g.s) | - |
| | | 7762 | $2_1^+$ | - |
| | | 5172 | $2_2^+$ | - |
| - | 17800 | 14130 | $0^+$(g.s) | - |
| | | 10762 | $2_1^+$ | - |
| | | 8172 | $2_2^+$ | - |

**Table 4.6** – Same as Tab. 4.5 but for unbound states of $^{11}$Be [128] and their decay patterns to $^{10}$Be.

| $J^\pi$ | $E^*$ (keV) | $E_r$ (keV) | state in $^{10}$Be | $\Gamma_r$ (keV) |
|---|---|---|---|---|
| $5/2^+$ | 1783 ±4 | 1283 | $0^+$(g.s) | 100 |
| $3/2^-$ | 2654 ± 10 | 2154 | $0^+$(g.s) | 206 |
| $3/2^-$ | 3400 ± 6 | 2900 | $0^+$(g.s) | 122 |
| $5/2^-$ | 3889 ± 1 | 3389 | $0^+$(g.s) | <8 |
| | | 20 | $2_1^+$ | |
| $3/2^-$ | 3949 | 3449 | $0^+$(g.s) | <8 |
| | | 80 | $2_1^+$ | |
| $7/2^-$ | 6705 ± 21 | 6200 | $0^+$ | 40 ± 20 |
| | | 2830 | $2_1^+$ | 40 ± 20 |
| | | 250 | $2_2^+$ | 40 ± 20 |
| $5/2^-$ | 7030 ± 50 | 6530 | $0^+$ | 300 |
| | | 3160 | $2_1^+$ | 300 |
| | | 570 | $2_2^+$ | 300 |

**Fitting the Dalitz plots**

For these resonances that are 2n emitters, we can also study n-n correlations by analysing how the two neutrons interact in the final state via Dalitz plots, as described in Sect. 3.5. The axes of a Dalitz plot are the reduced relative energies between fragment-n ($\varepsilon_{fn}$) and n-n ($\varepsilon_{nn}$). The former will then reflect the decay patterns and the latter will show the strength of the interaction between the two neutrons in the final state. In order to understand experimental Dalitz plots we will compare them with simulations of a source emitting two neutrons.

In Ref. [133] the wave functions of the state were calculated and used as the source, but in the current study the task would be hectic because, as we will see, we have many states involved and sometimes they overlap. We therefore use a simple model [97, 123, 124] that takes into account the n-n FSI (see Sect. 3.5), and where the source emitting two independent neutrons is assumed to be a Gaussian distribution that only depends on their relative distance, $W(r_{nn})$, and not on their momenta. This approximation was proven to fairly describe the FSI in previous works [125, 160–164]. Hence, we choose the Gaussian approximation without pretension of probing microscopic geometrical configurations of the states in $^{12}$Be, but only trying to describe qualitatively the kinematics of the observed correlation signal.

The simulation is made for direct and sequential decays with the following inputs:

- Decay energy and width of the unbound state in $^{12}$Be.
- Decay energy and width of the intermediate resonance in $^{11}$Be, in case of sequential decay.
- Two space-time parameters, $r_0$ and $\tau_0$ that quantify the strength of the n-n FSI [124].

In Ref. [124] it was shown that the sequential decay of $^{8}$He through the ground state of $^{7}$He leads to a weakening of the correlation signal at low $\varepsilon_{nn}$, which was attributed to the delay induced by the intermediate resonance, consistent with the lifetime of the narrow ($\Gamma_r$ = 150 keV) $^{7}$He ground state. It is then judicious to assume that, in the case of a sequential decay, the parameter $\tau_0$ is related to the lifetime of the intermediate resonance in $^{11}$Be ($\tau_0 = \tau/\sqrt{2}$ [124]), and accounts for the delay induced by the latter. The lifetime $\tau$ is given by the Heisenberg relation :

$$\tau = \frac{\hbar c}{\Gamma_r} \tag{4.2}$$

The parameter $r_0$ describes the spacial correlation and can be related to the root-mean-square n-n distance, $r_{nn}^{rms}$. In Ref. [162] the values of $r_{nn}^{rms}$ were found to be constant for a given nucleus, independently of the excitation energy of the resonance. Hence, for this parameter, we will use a fixed value that we deduce from the radius of an atomic nucleus $^{A}$X in the liquid drop model, $R = 1.2 \times A^{1/3}$. Assuming that the two neutrons are independently moving inside a sphere of that radius, the n-n relative distance is given by $r_{nn}^{rms} = 3 \times \frac{\sqrt{8}}{7} \times 1.2 \times A^{1/3}$, and comparing this to the one given in the model of Ref. [97], $r_{nn}^{rms} = r_0 \times \sqrt{6}$, we get the parameter $r_0$ used in the simulations:

$$r_0 = \frac{1}{\sqrt{6}} \times 3 \times \frac{\sqrt{8}}{7} \times 1.2 \times A^{1/3} \text{ fm} \tag{4.3}$$

For our nucleus of interest, $^{12}$Be, we find $r_0$ = 1.36 fm. This value is slightly below the suggested lower limit in the model, which is $r_0$ = 1.5 fm [97], but the correlation function is

still mathematically defined down to $r_0$ = 1.1 fm. Since we are only going to use this model for a qualitative comparison to the data, we will use (unless specified) $r_0$ = 1.36 fm for direct decay and ($r_0$, $\tau_0$) = (1.36 fm, $\hbar c/(\sqrt{2} \times \Gamma_r)$ ) for sequential decay.

### 4.4.2 Scan from 0 to 2 MeV

In this first 3-body energy range we are looking at low-lying resonances, just above the 2n-emission threshold that decay to the ground state of $^{10}$Be, or higher resonances that emit a low-energy neutron by decaying to excited states of $^{10}$Be. The latter is checked by observing $\gamma$-rays emitted in coincidence with a $^{10}$Be fragment (see Fig. 4.8b). The first candidate for low-lying resonances is the $2^+_2$ state observed previously by its decay to $^{11}$Be. This resonance, that is 920 keV above the 2n-emission threshold, can only decay to $^{10}$Be by a simultaneous emission of 2n since no intermediate resonance in $^{11}$Be is available in this energy range. There are hints of other possible candidates from higher resonances that decay sequentially to the two excited $2^+$ states of $^{10}$Be via:

1. Intermediate resonance in $^{11}$Be, $3/2^-$ or $5/2^-$, at 20 or 80 keV (see Tab. 4.6). This signal is seen at very low energy (Fig. 4.8a) which likely corresponds to the resonance observed in Ref. [130]. Due to the resolution of our neutron detector, these two resonances cannot be distinguished by the fit. Since in the two cases, a decay from a $2^+$ state would emit a neutron that carries an orbital momentum of $\ell$=1, we cannot favor either of the two resonances. The rigorous approach would be to make simulations with both resonances, and superimpose them to fit the data. This would be cumbersome and would not bring any additional information. Hence, for simplicity, we choose to use only the 20 keV resonance for the fit, reducing the number of simulations and degrees of freedom. We can see in Tab. 4.5 that the resonance at 8230 keV excitation energy is in this decay energy range (see also the highlighted region in Fig. 4.8c) and it has thus used to fit the data.

2. Intermediate resonances at 250 and 570 keV that correspond to two resonances in $^{11}$Be, $7/2^-$ and $5/2^-$, decaying to the $2^+_2$ state of $^{10}$Be. The latter emits two deexcitation $\gamma$-rays in cascade, which are seen at 2590 and 3368 keV respectively (Fig. 4.8b). The resonance in $^{12}$Be at 11800 keV is in this energy range (Tab. 4.5 and Fig. 4.8c) and will also be used to fit the data.

We use simulations with the above ingredients and the fit method described in Sect. 3.3 to fit the $E_d$($^{10}$Be+1n) spectrum. The results show that in this range 47$\pm$6 % of the events are from the decay of the $2^+_2$ state to the ground state of $^{10}$Be. The sequential decay via the $2^+_1$ state of $^{10}$Be contributes to 29$\pm$2 % and can be clearly identified by the resonance at low energy, $E_{n2}$ = 20 keV. The contributions of the resonant state at 11800 keV (Tab. 4.5), decaying sequentially via the two resonances at 250 and 500 keV above the $2^+_2$ state of $^{10}$Be, are 10 $\pm$ 2 % and 14 $\pm$ 3 %, respectively. We introduce these contributions to fit the structure around 250 keV and to compensate the abrupt decrease of the direct component at around 800 keV. The measured centroid energy of this resonance is 2170 keV. It is seen in this scan as having a width of about 1 MeV.

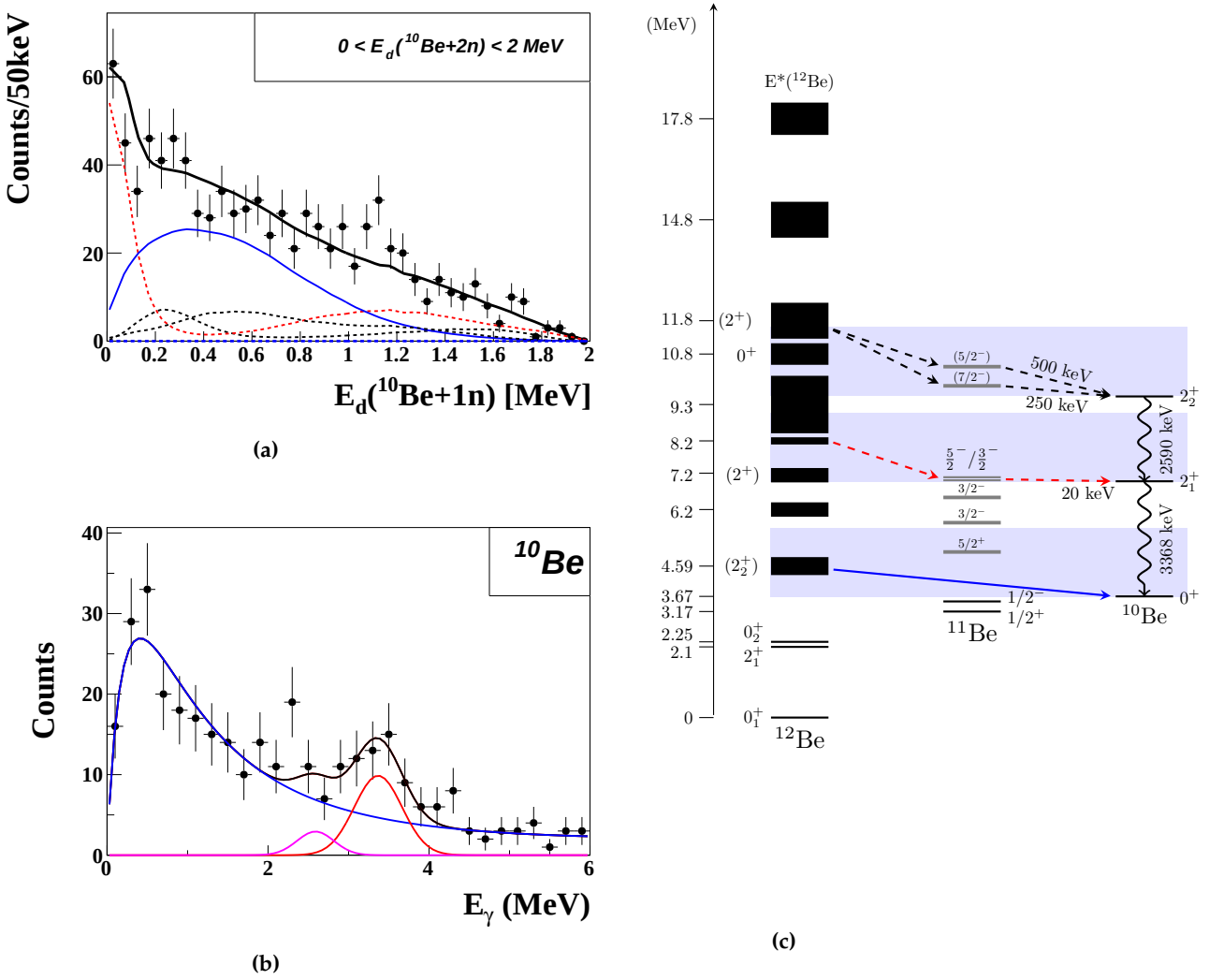


**Figure 4.8** – (a): Fit of the $E_d$($^{10}$Be+1n) spectrum for 0 < $E_d$($^{10}$Be+2n) < 2 MeV showing three resonances decaying on the ground and excited states of $^{10}$Be. (b): The proportion of decay to excited states is double checked using the fit of the $\gamma$-ray spectrum. (c): Level scheme summarizing the different decay patterns involved in this energy range.

**Table 4.7** – Results of the fit in the 3-body energy range from 0 to 2 MeV. The $1^{st}$ and $2^{nd}$ columns represent the excitation energy of the resonant states in $^{12}$Be and the measured centroid energy of the resonance, $E_r(^{10}Be+2n)$, respectively. In case of a sequential decay the relative energies of the first and second neutrons, $E_{n1}$ and $E_{n2}$, are given in the $3^{rd}$ and $4^{th}$ columns. The $5^{th}$ column shows the proportions of each component in this 3-body energy range. The last column shows the number of events corrected by the neutron efficiency (93%).

| $E^*(^{12}Be)$ (keV) | $E_r(^{10}Be+2n)$ (keV) | $E_{n1}$ (keV) | $E_{n2}$ (keV) | ratio (%) | $N_{events}$ |
|---|---|---|---|---|---|
| 4590 | 920 | - | - | $47 \pm 6$ | $211 \pm 28$ |
| 8230 | 1190 | 1170 | 20 | $29 \pm 2$ | $130 \pm 13$ |
| 11800 | 2170 | 1920 | 250 | $10 \pm 2$ | $45 \pm 10$ |
| | | 1600 | 570 | $14 \pm 3$ | $63 \pm 14$ |

The fit of the $\gamma$-ray spectrum (Fig. 4.8b) shows the presence of the first excited state of $^{10}$Be, $2_1^+$. The second one, $2_2^+$, is not clearly seen but suggested by the decay through the 250 and 500 keV resonances. The number of detected $\gamma$-rays at 3300 keV, obtained by integrating the Gaussian function (red, Fig. 4.8b), is a sum of the direct feeding of the $2_1^+$ state and cascade from the $2_2^+$ state. The former is obtained by subtracting the counts at 3300 and 2590 keV. It can be compared to the measured number of events in the 20 keV resonance, and their ratio is the $\gamma$-ray efficiency at 3300 keV:

$$N_\gamma(2_1^+) = 36 - 8 = 28 \pm 9$$
$$\epsilon_\gamma(3300\ \text{keV}) = 28/130 = 21 \pm 7\ \%.$$

**Table 4.8** – The $1^{st}$ column shows the populated states of $^{10}$Be. In the $2^{nd}$ column we give the number of detected $\gamma$-rays.

| States of $^{10}$Be | $N_\gamma$ |
|---|---|
| $2_1^+$ | $36 \pm 8$ |
| $2_2^+$ | $8 \pm 2$ |

In Ref. [95] an upper limit for the 2n-decay branching ratio of the $2_2^+$ state of $^{12}$Be was theoretically predicted to be 5%. In this work, thanks to a high 2n-detection efficiency, we can deduce this branching ratio. In fact, the state is well identified by its 2n direct decay to the ground state of $^{10}$Be, and its contribution well constrained, as shown in the fitting procedure. The number of events corresponding to this decay channel is $211 \pm 28$ (Tab. 4.7), and we can compare it to the total number of events given by the decay channels to $^{11}$Be and $^{10}$Be. The 2n branching ratio of the $2_2^+$ state is given by:

$$Br_{2n} = \frac{N(2_2^+ \rightarrow^{10} Be)}{N(2_2^+ \rightarrow^{10} Be) + N(2_2^+ \rightarrow^{11} Be)} = \frac{211}{211 + 5100} \tag{4.4}$$
$$= 0.039 \tag{4.5}$$

After error propagation we obtain a 2n branching ratio of $3.9 \pm 0.5$ %, which is in agreement with the upper limit of 5% given in [95].

### n-n correlations

Now that we have identified the decay channels present in this energy range, we can study the n-n correlations using the Dalitz plot method described in Sect. 3.5. We recall that direct decay will manifest by an increase at $\varepsilon_{nn} \sim 0$ and sequential decays by wings in the $\varepsilon_{fn}$ spectrum. On Fig. 4.9, we show simulations corresponding to the four decay channels identified by fitting the $E_d(^{10}Be+1n)$ spectrum. For all these simulations the space-time parameters ($r_0$, $\tau_0$) are fixed at the values (1.36 fm, 0) and (1.36 fm, $\hbar c/(\sqrt{2} \times \Gamma_r)$) for direct and sequential decays, respectively.

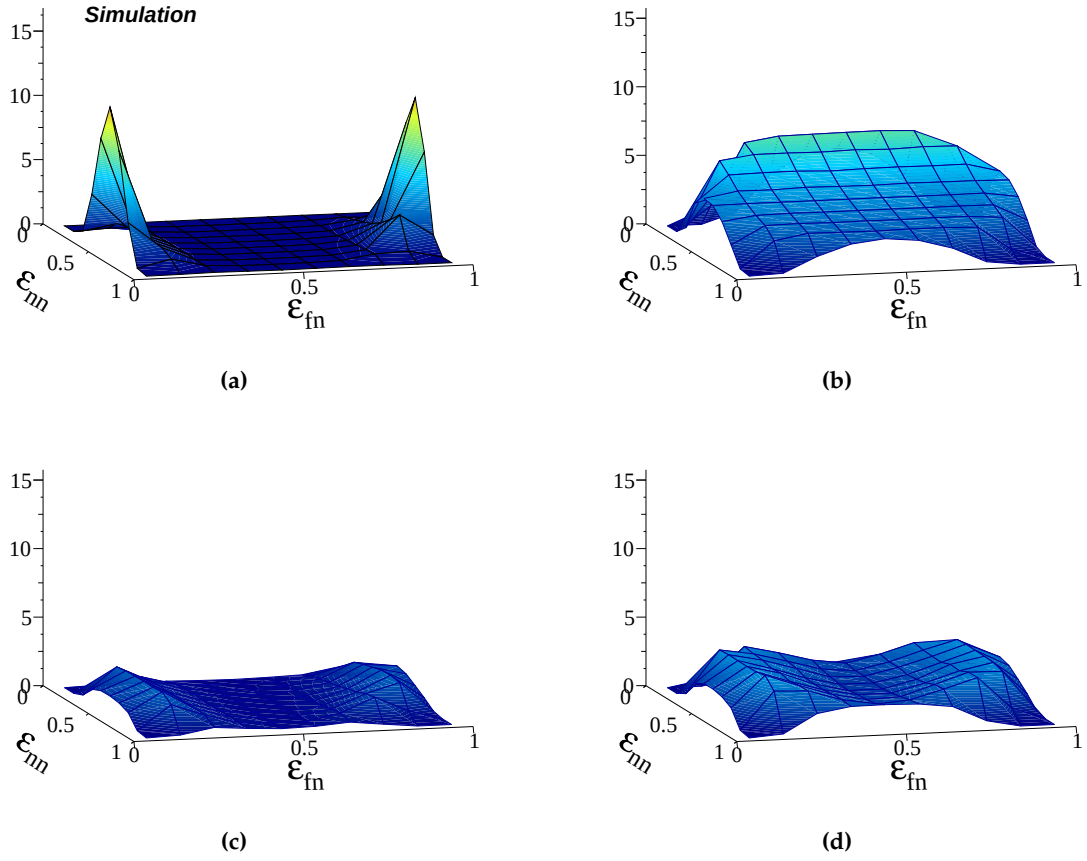


**Figure 4.9** – Simulated Dalitz plots corresponding to each of the four decay channels identified by fitting the $E_d(^{10}Be+1n)$ spectrum, with their respective proportions listed in Tab. 4.7. (b): Contribution of the direct decay of the resonance at 920 keV. (a), (c) and (d): Sequential decay contributions at 20, 250 and 500 keV, respectively (see text for simulation parameters).

The experimental Dalitz plot in this energy range is then compared to the one from simulation which is a combination of the four plots in Fig. 4.9, keeping the proportions of Tab. 4.7. If we name $SEQ_i$ the $i^{th}$ sequential channel, and $DIR_j$ the $j^{th}$ direct channel in the range, the total simulated Dalitz plot will be given by:

$$DAL_{tot} = \sum_j \alpha_j \times DIR_j + \sum_i \beta_i \times SEQ_i \tag{4.6}$$

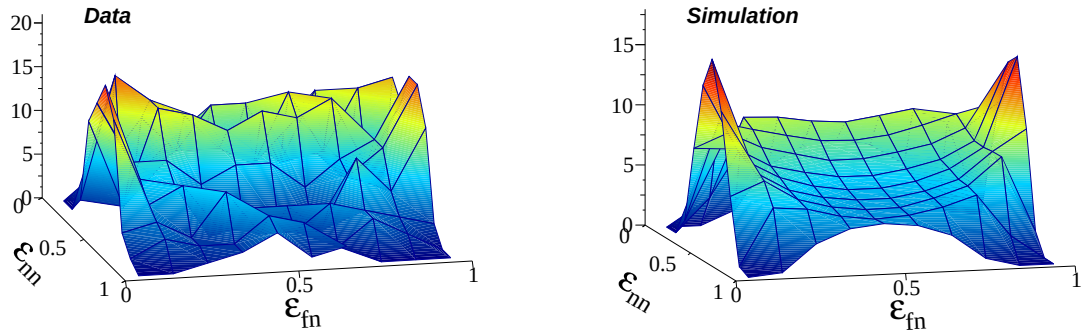


**Figure 4.10** – Dalitz plot for $E_d$($^{10}$Be+2n) from 0 to 2 MeV (a) is compared to the simulated one (b), giving $\chi^2_{Norm}$= 2.14. The simulated Dalitz plot is a sum of the four decay channels identified by fitting $E_d$($^{10}$Be+1n), and shown in Fig. 4.9.

From the fit using the resonances of Tab. 4.7, the direct decay from the $2^+_2$ state contributes with the coefficient $\alpha$ =47 $\pm$ 6% and the sequential components are added with coefficients $\beta_{1,2,3}$ = 29 $\pm$ 2%, 10 $\pm$ 2% and 14 $\pm$ 3% . The resulting simulated Dalitz plot is shown on Fig. 4.10b in comparison with the experimental one of Fig. 4.10a. We compared the simulated and experimental Dalitz plots bin by bin and deduced a normalised $\chi^2$ value of 2.14. This tells us that the simulation fits relatively well the data, although visually the increase at low $\varepsilon_{nn}$ is a bit higher in the data than in the simulation. This may be due to the statistical fluctuations in this energy range. Moreover, we can see that the ridge as well as the wings on the $\varepsilon_{fn}$ axis are well reproduced by the simulation. This confirms the results of the fit obtained using the $E_d$($^{10}$Be+1n) spectrum.

### 4.4.3 Scan from 2 to 3 MeV

We will now consider the 3-body energy range from 2 to 3 MeV. The highlighted region on the level scheme in Fig. 4.11c shows all the possible contributions to this energy range. An easy guess is to first try to fit the $E_d$($^{10}$Be+1n) spectrum with only the direct decay from the resonance at 6200 keV in $^{12}$Be, plus the one at 9300 keV decaying through the same low-energy intermediate resonance 20 keV above the $2^+_1$ state of $^{10}$Be . This simple ingredient is not enough, and we have to add other contributions from the previously observed decays to the $2^+_2$ state of $^{10}$Be through 250 and 570 keV resonances in $^{11}$Be. These contributions correspond to the $2^+$ resonance at 11800 keV in $^{12}$Be. The state at 6200 keV also decays sequentially through the $5/2^+$ state in $^{11}$Be located at 1283 keV above the ground state of $^{10}$Be. The results of the fits are reported in the Tab. 4.10. The contributions of the decay though excited states of $^{10}$Be are constrained by the number of detected $\gamma$-rays.

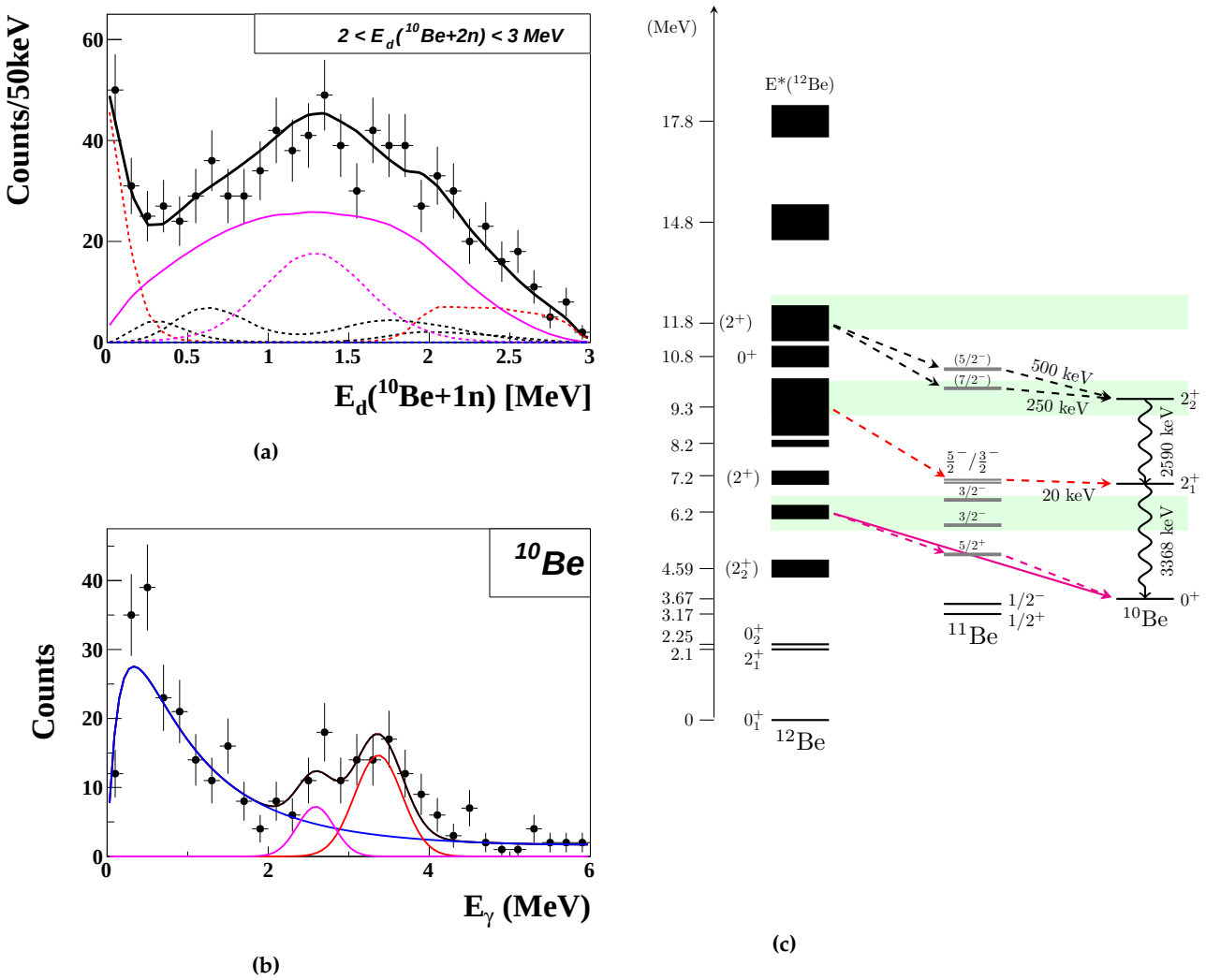


**Figure 4.11** – (a): Fit of the $E_d(^{10}Be+1n)$ spectrum in the 3-body energy range from 2 to 3 MeV, which shows the various decay patterns including the ones to the excited states of $^{10}$Be through intermediate resonances in $^{11}$Be. (b): Fit of $\gamma$-ray spectrum showing the presence of the two $2^+$ states of $^{10}$Be. (c): The level scheme summarizes the decay patterns found in this energy range.

**Table 4.9** – The number of detected events for the two excited states of $^{10}$Be is deduced from the fit of the $\gamma$-spectrum (Fig. 4.11b). $N_{events}$ corresponds to the counts corrected by the $\gamma$-ray efficiency.

| States of $^{10}$Be | $N_\gamma$ |
|---|---|
| $2^+_1$ | $48 \pm 9$ |
| $2^+_2$ | $30 \pm 7$ |

**Table 4.10** – Results of the fit in the 3-body energy range from 2 to 3 MeV. The $1^{st}$ and $2^{nd}$ columns represent the excitation energy of the resonant states in $^{12}$Be and the measured centroid energy of the resonance, $E_r(^{10}Be+2n)$, respectively. In case of a sequential decay the relative energies of the first and second neutrons, $E_{n1}$ and $E_{n2}$, are given in the $3^{rd}$ and $4^{th}$ columns. The $5^{th}$ column shows the proportions of each component in this 3-body energy range. The last column shows the number of events corrected by the neutron efficiency.

| $E^*(^{12}Be)$ (keV) | $E_d(^{10}Be+2n)$ (keV) | $E_{n1}$ (keV) | $E_{n2}$ (keV) | ratio (%) | $N_{events}$ |
|---|---|---|---|---|---|
| 11800 | 2170 | 1920 | 250 | 4±2 | 17 ± 8 |
| | | 1600 | 570 | 9±4 | 38 ± 17 |
| 6200 | 2600 | - | - | 55 ± 13 | 238 ± 57 |
| | | 1320 | 1283 | 17±4 | 74 ± 17 |
| 9300 | 2260 | 2240 | 20 | 15±2 | 65 ± 9 |

We can also deduce the $\gamma$-ray efficiency at 3300 keV in the same way we did in the previous 3-body energy range. For this we use the number of detected $\gamma$-rays in Tab. 4.9 and compare it to the 20 keV events. We obtain the value of $\epsilon_\gamma$ = 27 ± 8 % which can be combined with the one obtained in the previous energy range to get $\epsilon_\gamma$(3300 keV) = 24 ± 10 %. The large uncertainty is due to the small number of events involved in the calculations. The $\gamma$-efficiency obtained here is used to determine the scaling factor for the $\gamma$-ray efficiency curve (Sect. 3.3.3).

**n-n correlations**

We compare experimental Dalitz plots with the simulation using the model described above and taking the results from the fit as entries for the simulation. Hence the simulated Dalitz plot (Fig. 4.11b) is a combination of the five decay channels, replacing the coefficients in Eq. (4.6) by the proportions listed in Tab. 4.5. In this range also the simulation reproduces well the data, as we can see on Fig. 4.11. The wings at $\varepsilon_{fn} \sim 0$ and 1 represent the sequential decay through the low-energy resonance at 20 keV above the $2_1^+$ of $^{10}$Be. The increase at low $\varepsilon_{nn}$ is due to direct decay (55%) combined to the sequential decay through the $5/2^+$ resonance at 1283 keV (17%). In fact, the decay energy of the resonance at 6200 keV in $^{12}$Be is almost equally shared between the two neutrons leading to two close wings around $\varepsilon_{fn}$ = 0.5. The signal at low $\varepsilon_{nn}$ is slightly weaker in the simulation with the parameters $r_0$=1.36 fm and $\tau_0$=$\hbar c/(\sqrt{2} \times \Gamma_r)$, but still compatible with the experiment.

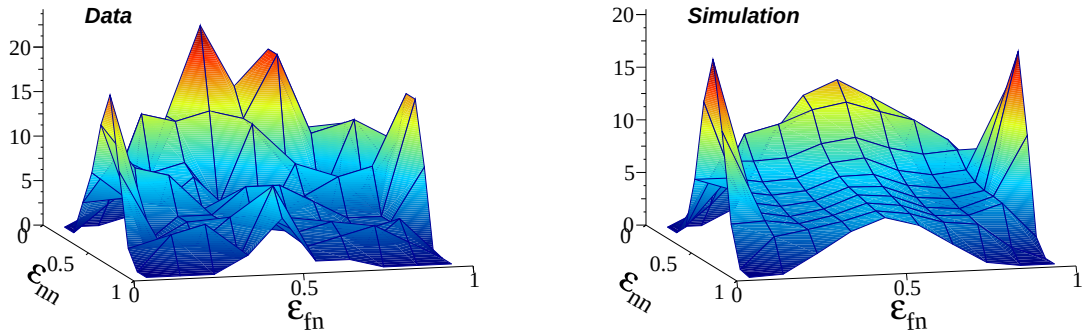


**Figure 4.12** – Comparison of the experimental (a) and simulated (b) Dalitz plots for $E_d(^{10}Be+2n)$ from 2 to 3 MeV. The simulated Dalitz plot is a sum of the five decay channels identified by fitting $E_d(^{10}Be+1n)$.

### 4.4.4 Scan from 3 to 4 MeV

We continue with a narrow 3-body energy range so that we can isolate contributions from only two resonant states in $^{12}$Be (Fig. 4.13c) with enough statistics. These are the two known $2^+$ and $0^+$ resonances in $^{12}$Be at 7200 keV and 10800 keV, decaying to the ground and first excited states of $^{10}$Be, respectively. The $\gamma$-ray spectrum (Fig. 4.13b) corroborates the fact that no higher resonance in $^{12}$Be decays through the excited $2_2^+$ state of $^{10}$Be. We only see one photopeak corresponding to the $2_1^+$ state of $^{10}$Be at 3300 keV. The $E_d(^{10}Be+1n)$ spectrum in this range is fitted by a combination of sequential and direct decays from these two resonances (Fig. 4.13a). The amount of direct decay is limited by the low amplitude at around 500 keV. The results of the fit in this range are listed in Tab. 4.11. The direct-decay contribution from the resonance at $E^*$ = 10800 keV is constrained by the number of $\gamma$-rays corrected by the efficiency (Tab. 4.12). Another direct-decay contribution from the resonance at $E^*$ = 7200 keV is added to the fit. Note that the decay energies of the two are very similar (3600 and 3760 keV) and the combined analysis of the $\gamma$ and $E_d(^{10}Be+1n)$ spectra is crucial to disentangle them.

**Table 4.11** – Results of the fit in the 3-body energy range from 3 to 4 MeV. The $1^{st}$ and $2^{nd}$ columns represent the excitation energy of the resonant states in $^{12}$Be and the measured centroid energy of the resonance, $E_r(^{10}Be+2n)$, respectively. In case of a sequential decay the relative energies of the first and second neutrons, $E_{n1}$ and $E_{n2}$ are given in the $3^{rd}$ and $4^{th}$ columns. The $5^{th}$ column shows the proportions of each component in this 3-body energy range. The last column shows the number of events corrected by the neutron efficiency.

| $E^*(^{12}Be)$ (keV) | $E_d(^{10}Be+2n)$ (keV) | $E_{n1}$ (keV) | $E_{n2}$ (keV) | ratio (%) | $N_{events}$ |
|---|---|---|---|---|---|
| 7200 | 3600 | 1446 | 2154 | 52 ± 10 | 242 ± 48 |
| | 3600 | - | - | 21 ± 7 | 97 ± 19 |
| 10800 | 3760 | 3740 | 20 | 14± 1 | 65 ± 5 |
| | 3760 | - | - | 13± 3 | 60 ± 11 |

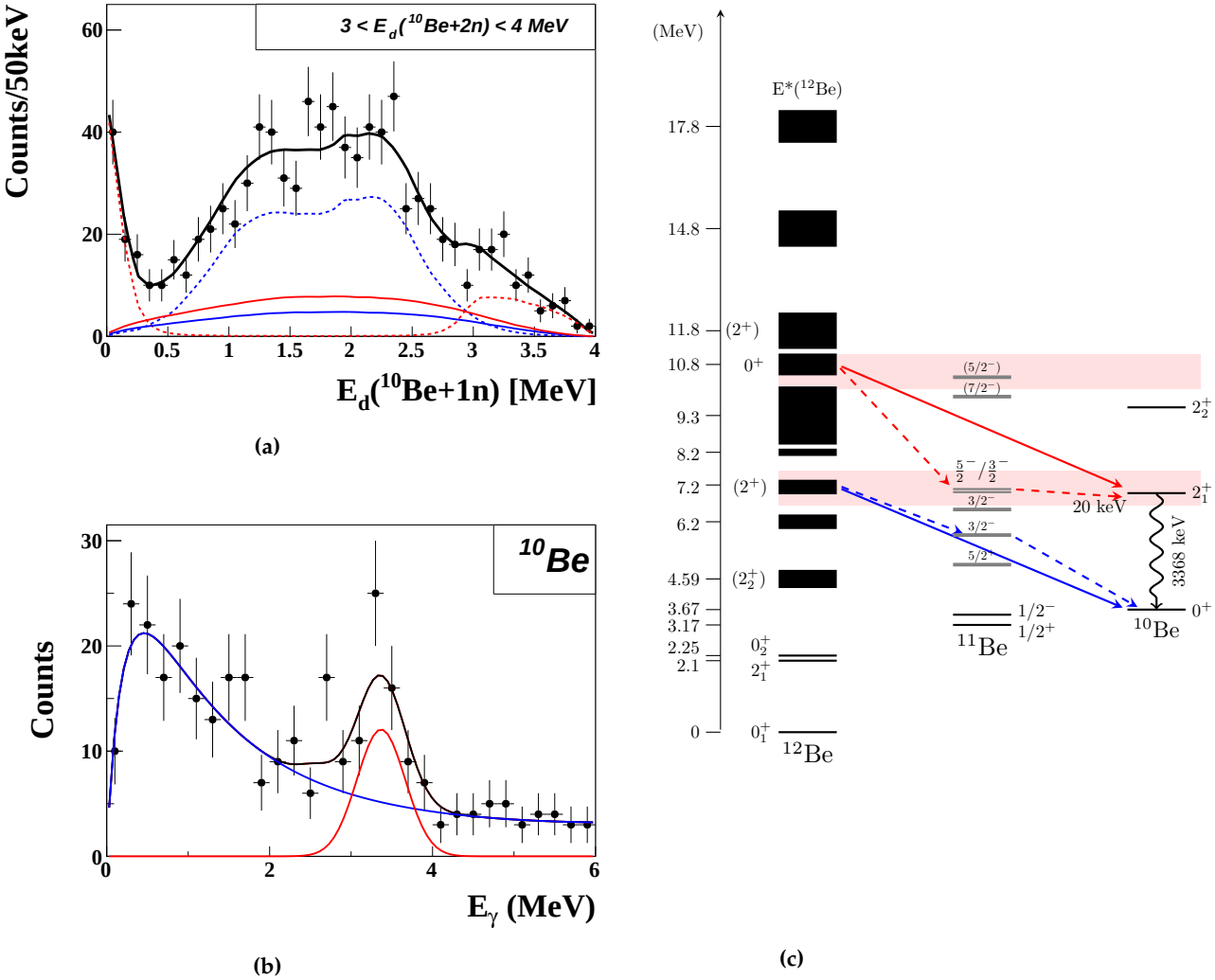


**Figure 4.13** – (a): Fit of the $E_d$($^{10}$Be+1n) spectrum for 3 < $E_d$($^{10}$Be+2n) < 4 MeV showing four contributions from direct and sequential decays of two resonances in $^{12}$Be decaying to the ground and excited states of $^{10}$Be. (b): Fit of the $\gamma$-ray spectrum showing the presence of only the $2^+_1$ state of $^{10}$Be. The number of detected $\gamma$-rays is used to constrain the contribution from decay through the excited state of $^{10}$Be. (c): Summary of the different decay patterns.

**Table 4.12** – The number of detected events for the $2^+_1$ state of $^{10}$Be is deduced from the fit of the $\gamma$-spectrum (Fig. 4.13b). $N_{events}$ corresponds to the counts corrected by the $\gamma$-efficiency.

| States of $^{10}$Be | $N_\gamma$ | $N_{events}$ |
|---|---|---|
| $2^+_1$ | $40 \pm 9$ | $166 \pm 55$ |

**n-n correlations**

The n-n correlations in this 3-body energy range are revealed by comparing the experimental Dalitz plot and simulation as described in other ranges above. What is special in this range is that, looking at the signal at low $\varepsilon_{nn}$ in the Dalitz plot (Fig. 4.14a), we have the impression that the direct decay is dominant whereas in the result of the fit the direct decay contributes only to about 34% against 66% for the sequential decay. Contrary to the previous 3-body energy ranges, the simulated Dalitz plot with the parameter $\tau_0 = \hbar c/\Gamma_r$ does not reproduce correctly the data (Fig. 4.14b, $\chi^2_{Norm}$=2.88 ). The decay through the intermediate resonance at 2154 keV (52±10 % ) is seen as two wings in the middle of the Dalitz plot. It seems that the two neutrons are strongly correlated even when they are emitted sequentially through a relatively narrow resonance ($\Gamma_r$= 200 keV, Tab. 4.5). This could be attributed to initial n-n correlations, that would be more important in the $^{12}$Be states we are studying than in previous works (e.g. $^{8}$He in Ref. [124]), leading to stronger correlation signals even in the case of sequential decays. When we turn off the parameter $\tau_0$ ($\tau_0$ = 0), we see an improvement in the fit (Fig. 4.14c, $\chi^2_{Norm}$=1.35). Setting the parameter $\tau_0$ = 0 is then necessary to qualitatively describe the signal at low $\varepsilon_{nn}$ within the simple FSI model.

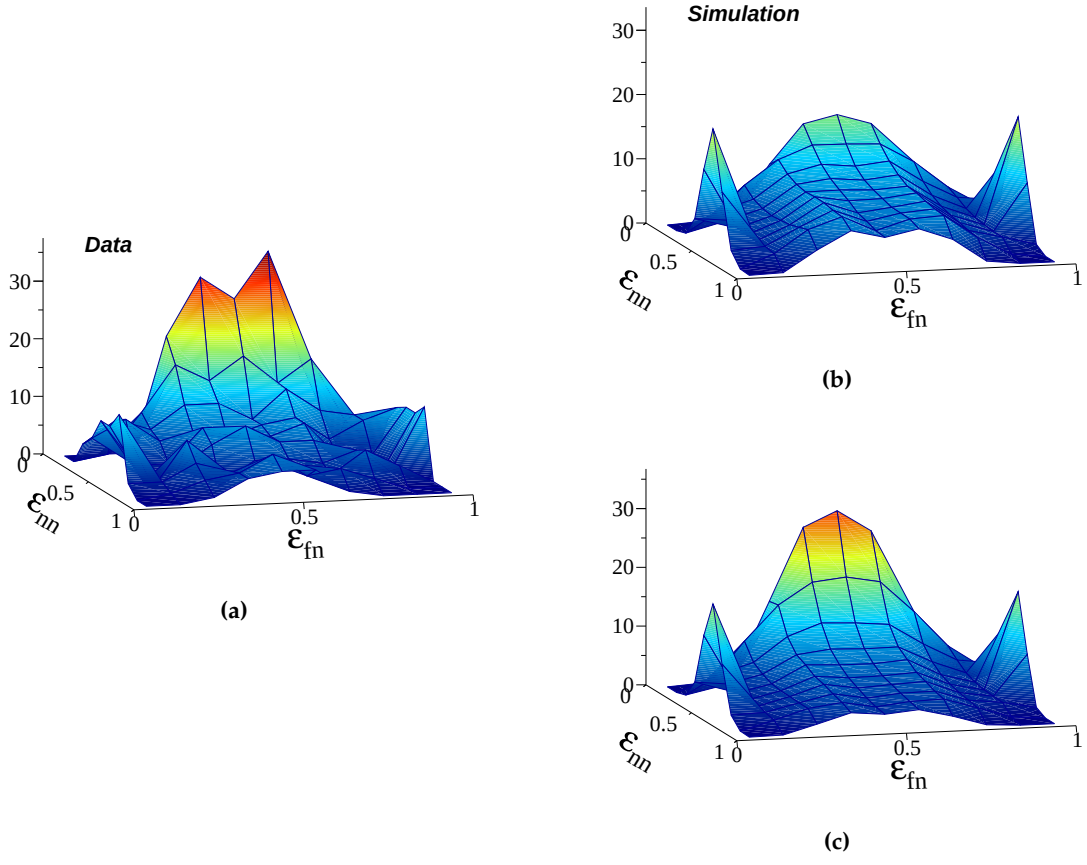


**Figure 4.14** – Comparison of the experimental (a) and simulated (b) Dalitz plots in the 3-body energy range from 3 to 4 MeV. The simulated Dalitz plot is a sum of the four decay channels identified by fitting the $E_d(^{10}Be+1n)$ spectrum. The wings on the sides represent the sequential decay through the 20 keV resonance, and the signal at $\varepsilon_{nn} \sim 0$ is explained by a combination of the direct and sequential decays through the resonance at 2154 keV. (b): Simulation with the parameters ($r_0$,$\tau_0$) = (1.36 fm, $\hbar c/\Gamma_r$). (c): Simulation with (1.36 fm, 0), which reproduces better the data (see text).

### 4.4.5 Scan from 4 to 5.5 MeV

In this 3-body energy the contributions may come from the decay of the previously observed high-energy resonances to the ground state of $^{10}$Be. The fit of the $\gamma$-ray spectrum shows that only the $2_1^+$ state of $^{10}$Be is populated. Hence, this range is chosen to only include the decay to ground state for the resonance at E$^*$=8230 keV and the decay of the resonance at E$^*$=11800 keV to the $2_1^+$ state of $^{10}$Be (region in red, Fig. 4.15c). The fit of the E$_d$($^{10}$Be+1n) spectrum shows that the resonance at 8200 keV in $^{12}$Be decays sequentially through resonances in $^{11}$Be, E$_{n2}$ = 1284 and 2154 keV, and directly to the ground state of $^{10}$Be with a decay energy E$_d$= 4560 keV. In the same way, the resonance at 11800 keV decays sequentially via the resonance E$_{n2}$ = 20 keV in $^{11}$Be and directly to the excited $2_1^+$ state of $^{10}$Be. The results of the fit are reported in Tab. 4.13.

The direct decay contributes to 53% of the total fit and is constrained by the low amplitude at around 500 keV in the E$_d$($^{10}$Be+1n) spectrum. The two direct-decay components at E$_d$= 4762 and 4560 keV are disentangled by the number of detected $\gamma$-rays (Tab. 4.14). In fact, the 20 keV component of the fit is well constrained by the low-energy structure in E$_d$($^{10}$Be+1n) spectrum (Fig. 4.15a), then the direct decay to the excited state is added to match the number of $\gamma$-rays. The sequential decay through the intermediate resonance at 2154 keV contributes to 29 % and is necessary to fit the E$_d$($^{10}$Be+1n) spectrum at around 2 MeV.

**Table 4.13** – Results of the fit in the 3-body energy range from 4 to 5.5 MeV. The $1^{st}$ and $2^{nd}$ columns represent the excitation energy of the resonant states in $^{12}$Be and the centroid energy of the resonance, E$_r$($^{10}$Be+2n), respectively. In case of a sequential decay the relative energies of the first and second neutrons, E$_{n1}$ and E$_{n2}$ are given in the $3^{rd}$ and $4^{th}$ columns. The $5^{th}$ column shows the proportions of each component in this 3-body energy range. The last column shows the number of events corrected by the neutron efficiency.

| E$^*$($^{12}$Be) (keV) | E$_d$($^{10}$Be+2n) (keV) | E$_{n1}$ (keV) | E$_{n2}$ (keV) | ratio (%) | N$_{events}$ |
|---|---|---|---|---|---|
| 8230 | 4560 | - | - | 28 $\pm$ 4 | 204 $\pm$ 28 |
| | 4560 | 2406 | 2154 | 29 $\pm$ 3 | 212 $\pm$23 |
| | 4560 | 3277 | 1283 | 13 $\pm$ 2 | 95 $\pm$ 15 |
| 11800 | 4760 | 4740 | 20 | 5 $\pm$ 1 | 36 $\pm$ 7 |
| | 4760 | - | - | 25 $\pm$ 3 | 183 $\pm$ 25 |

**Table 4.14** – The $2^{nd}$ column shows the number of detected events for the $2_1^+$ state of $^{10}$Be. The last column represents the number of events after correction by the $\gamma$-efficiency.

| State of $^{10}$Be | N$_\gamma$ | N$_{events}$ |
|---|---|---|
| $2_1^+$ | 53 $\pm$ 7 | 220 $\pm$ 68 |

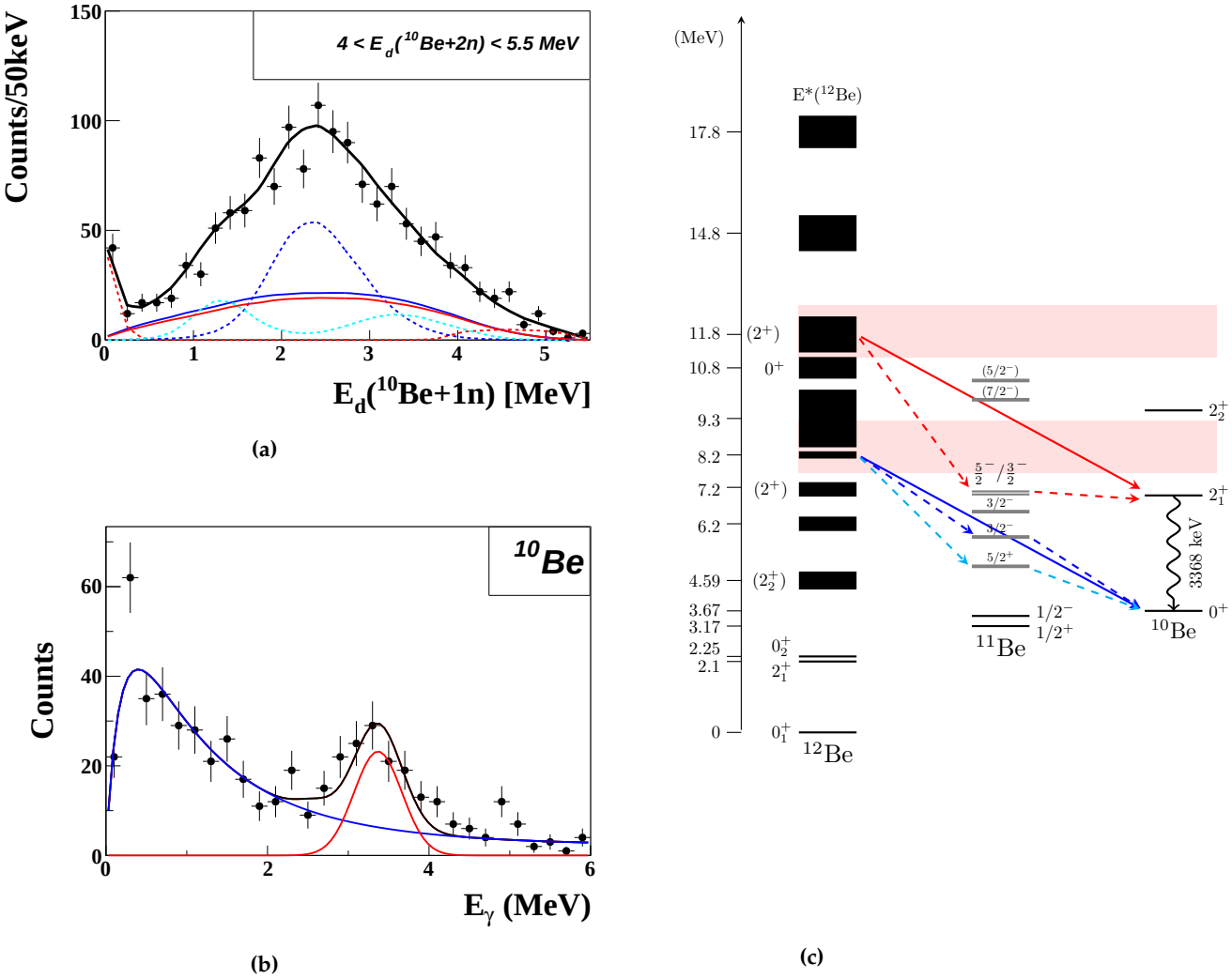


**Figure 4.15** – (a): Fit of the $E_d(^{10}Be+1n)$ spectrum for 4 < $E_d(^{10}Be+2n)$ < 5.5 MeV showing five contributions, both sequential and direct, from two resonant states in $^{12}Be$ decaying to the ground and excited states of $^{10}Be$. (b): Fit of the $\gamma$-ray spectrum showing the presence of only the $2^+_1$ state of $^{10}Be$. The number of $\gamma$-rays is used to constrain the component from decay through the $2^+_1$ state. (c): The different decay patterns are shown on the level scheme.

### n-n correlations

The n-n correlations studied by the Dalitz plots in this energy range are similar to the previous 3-body energy range. We see events at low $\varepsilon_{nn}$ that look like direct decay but are found to be a combination of direct and sequential decays. In this energy range, we have 53 % of direct decay and 47 % of sequential decay. The ingredients for the simulated Dalitz plot are taken from the fit results in Tab. 4.13 following Eq. (4.6). As we can see in Fig. 4.16b, especially the signal at low $\varepsilon_{nn}$, the simulated Dalitz plot with parameter $\tau_0 = \hbar c/\Gamma_r$ does not fit well the data ($\chi^2$ = 2.5). This signal at low $\varepsilon_{nn}$ is an indication of strong n-n correlations, which may be due to initial correlations in the $^{12}Be$ or an alignment of the momenta of the neutrons in the final state. We proceed as we did in the energy range from 3 to 4 MeV, i.e.

set the parameter $\tau_0 = 0$. The Dalitz plot from simulations with this value reproduces better ($\chi^2 = 1.05$) the data as it can be seen in Fig. 4.16c. For the time being we fit these data with an unphysical $\tau$ parameter. We will address the reason for having sequential decays through a narrow resonance while assuming the simultaneous emission of both neutrons in Sect. 4.5.2.

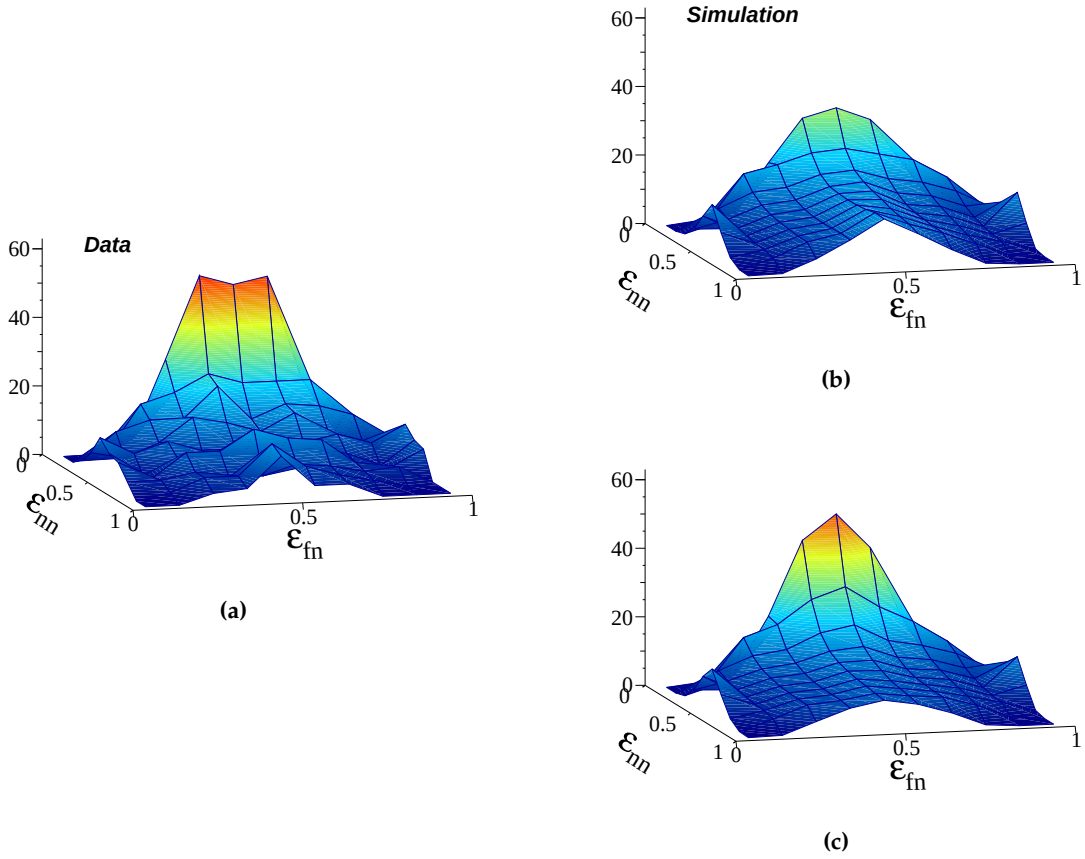


**Figure 4.16** – The experimental Dalitz plot (a) is compared to the simulated ones with parameters ($r_0$,$\tau_0$) = (1.36 fm, $\hbar c/\Gamma_r$) (b) and (1.36 fm, 0) (c). The simulated plot is a sum of all decay channels identified in this 3-body energy range by fitting the $E_d$($^{10}$Be+1n) spectrum. The plot in (c) reproduces the data better ($\chi^2 = 1.05$) than the plot in (b) ($\chi^2 = 2.5$).

### 4.4.6 Scan from 5.5 to 8 MeV

At high 3-body energies, above $E_d$($^{10}$Be+2n) $\sim$ 5 MeV, the number of detected events drops due to the acceptance of the neutron detector as explained in Sect. 3.4.3 (also see Fig. 4.5a). Therefore, we have chosen a broader 3-body energy range in order to have sufficient statistics, comparable to those obtained in the previous scans. The drawback of choosing a broad energy range is that it contains many resonances that may overlap. Luckily, the possible contributions to this energy range are from the resonances that we identified before by their decay to lower energies, except two high-energy resonances at 14800 and 17800 keV. Moreover, the fit shows the predominance of the $0^+$ state at 10800 keV in $^{12}$Be decaying to the ground state of $^{10}$Be. The decay is direct or sequential through the resonances in $^{11}$Be, $E_{n2}$ = 2900 and 2154 keV.

Another contribution coming from the $2^+$ resonance at 11800 keV is introduced in order to fit the structure at around 1300 keV in the $E_d$($^{10}$Be+1n) spectrum, which corresponds to the $5/2^+$ resonance in $^{11}$Be. Indeed, a $0^+$ state would have to overcome a high centrifugal barrier,

$\ell \geq 2$, to pass through the resonance with spin $5/2^+$ making it less favorable as compared to the $2^+$ state. The resonance at very low energy in the $E_d(^{10}Be+1n)$ spectrum is fitted by the resonance at 14800 keV decaying through the intermediate resonance at $E_{n2}$ = 20 keV. The direct decay to the $2_1^+$ state in $^{10}Be$ is introduced to match the number of $\gamma$-rays (Tab. 4.16) that cannot be accounted for with only the sequential decay (3%). Similarly to the previous range, the direct component is a sum of the two direct decays, $E_d$ = 7130 and 7760 keV, and is constrained by the decrease of the amplitude around 500 keV. Tab. 4.15 summarizes the fit results.

A negligible contribution ($2 \pm 1$ %) from sequential decay through 570 keV is also possible. This contribution is from the resonance at 17800 keV and is constrained by the number of events which decay to the $2_2^+$ state of $^{10}Be$ ( $15 \pm 9$, Tab. 4.16).

**Table 4.15** – Results of the fit in the range from 5.5 to 8 MeV. The $1^{st}$ and $2^{nd}$ columns represent the excitation energy of the resonant states in $^{12}Be$ and the centroid energy of the resonance, $E_r(^{10}Be+2n)$, respectively. In case of a sequential decay the relative energies of the first and second neutrons, $E_{n1}$ and $E_{n2}$ are given in the $3^{rd}$ and $4^{th}$ columns. The $5^{th}$ column shows the proportions of each component in this 3-body energy range. The last column shows the number of events corrected by the neutron efficiency.

| $E^*(^{12}Be)$ (keV) | $E_d(^{10}Be+2n)$ (keV) | $E_{n1}$ (keV) | $E_{n2}$ (keV) | ratio (%) | $N_{events}$ |
|---|---|---|---|---|---|
| 10800 | 7130 | - | - | $18 \pm 8$ | $142 \pm 56$ |
| | | 4230 | 2900 | $21 \pm 7$ | $166 \pm 30$ |
| | | 4970 | 2154 | $19 \pm 4$ | $150 \pm 35$ |
| 11800 | 8130 | 6850 | 1283 | $11 \pm 3$ | $87 \pm 24$ |
| 14800 | 7760 | 7740 | 20 | $4 \pm 1$ | $31 \pm 8$ |
| | 7760 | - | - | $25 \pm 8$ | $198 \pm 40$ |
| 17800 | 8240 | 7670 | 570 | $2 \pm 1$ | $16 \pm 8$ |

**Table 4.16** – The $1^{st}$ column shows the populated states of $^{10}Be$. The $2^{nd}$ column shows the number of detected events for the $2_1^+$ state of $^{10}Be$. The last column represents the number of events after correction by the $\gamma$-ray efficiency.

| States of $^{10}Be$ | $N_\gamma$ | $N_{events}$ |
|---|---|---|
| $2_1^+$ | $69 \pm 7$ | $283 \pm 80$ |
| $2_2^+$ | $15 \pm 9$ | $58 \pm 25$ |

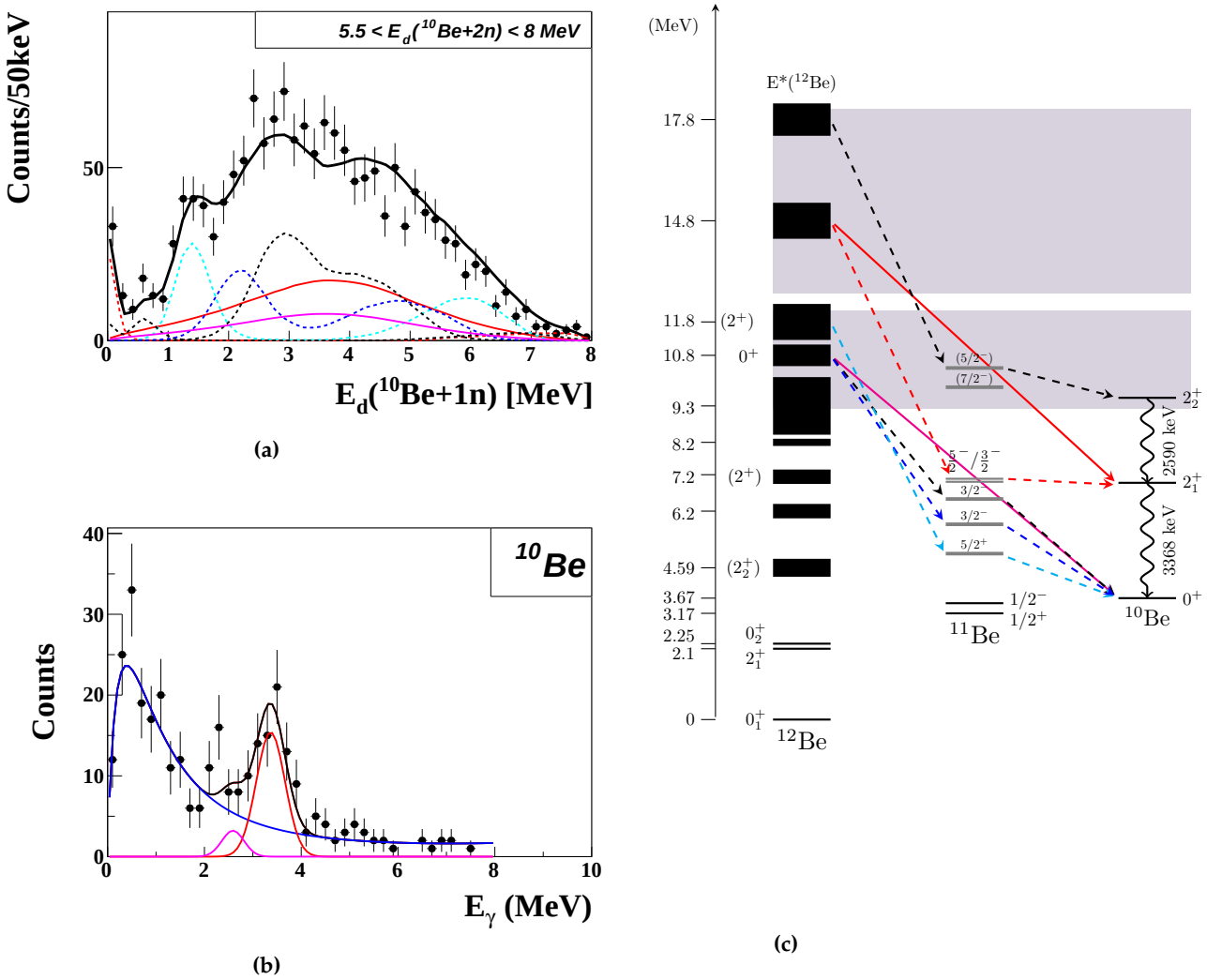


**Figure 4.17** – Results of the fit in the 3-body energy range from 5.5 to 8 MeV. (a): $E_d(^{10}Be+1n)$ spectrum fitted by a combination of direct and sequential decays, which is a sum of the two direct components (red and magenta in (c)), plus 5 sequential components. The proportion of decay to the excited states is double checked using the fit of $\gamma$-ray spectrum (b). All decay patterns are shown in (c).

### n-n correlations

The Dalitz plot in this energy range is also analysed in order to deduce the n-n correlations. As done in the previous 3-body energy range, the experimental and simulated plots are compared. We make simulations taking into account the fit results in Tab. 4.15 and the space-time parameters $r_0$=1.36 fm and $\tau_0 = \hbar c/\Gamma_r$. The latter is constrained by the widths $\Gamma_r$ of intermediate resonances in $^{11}$Be which are known (see Tab. 4.5). We notice in Fig. 4.18b that the signal at low $\varepsilon_{nn}$ in the data cannot be reproduced by the simulations with the parameter $\tau_0 = \hbar c/\Gamma_r$. We then set the parameter to 0 ($\tau_0 = 0$) in the simulation to qualitatively reproduce the data. We can see in Fig. 4.18c that the simulated Dalitz plot reproduces better the data, especially the increase at low $\varepsilon_{nn}$.

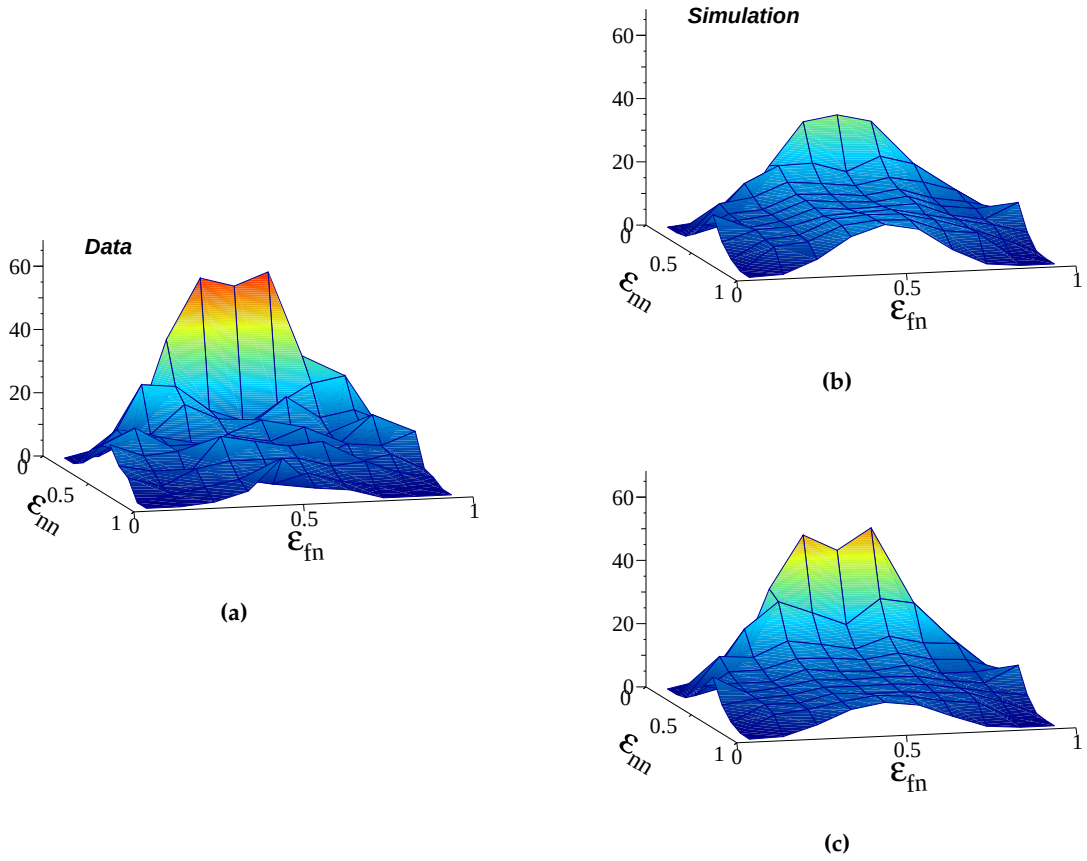


**Figure 4.18** – Dalitz plot for the 3-body energy from 5.5 to 8 MeV (a) compared to the simulated one with the parameters $r_0$ = 1.36 fm and $\tau_0 = \hbar c/\Gamma_r$ (b) or $\tau_0 = 0$ (c). The latter better fits the data.

### 4.4.7 Scan from 8 to 15 MeV

This high-energy range is the last we can select with enough statistics because of the decrease of the neutron detector acceptance. It contains two resonances, at 14800 and 17800 keV, previously observed by their decay at lower energies through excited states of $^{10}$Be. We choose to include both of them in the same range because, due to the acceptance, the last resonance is highly suppressed and could not be studied alone. We notice several decay channels visible in the $E_d(^{10}\text{Be+1n})$ spectrum, that may come from both resonances. At low fragment-n energies, $E_d(^{10}\text{Be+1n}) < 4$MeV, the structures are distinguishable and resemble the low-energy resonances in $^{11}$Be. The resonance at around 20 keV is the one we saw before decaying to the $2^+$ state of $^{12}$Be, that is constrained by the number of counts in the $\gamma$-ray spectrum corrected by the efficiency. Other structures are at around the 1284, 2154 and 2900 keV resonances in $^{11}$Be. These energies correspond to the second neutron emitted $E_{n2}$, and the corresponding $E_{n1}$ are determined from the fit. The sum of $E_{n1}$ and $E_{n2}$ determines which resonance among the two is involved in a given decay channel. Apart from the sequential decays, we also include the direct decay which is constrained by the low amplitude at around 4 MeV. A summary of all observed decay channels in this range is presented in Tab. 4.18.

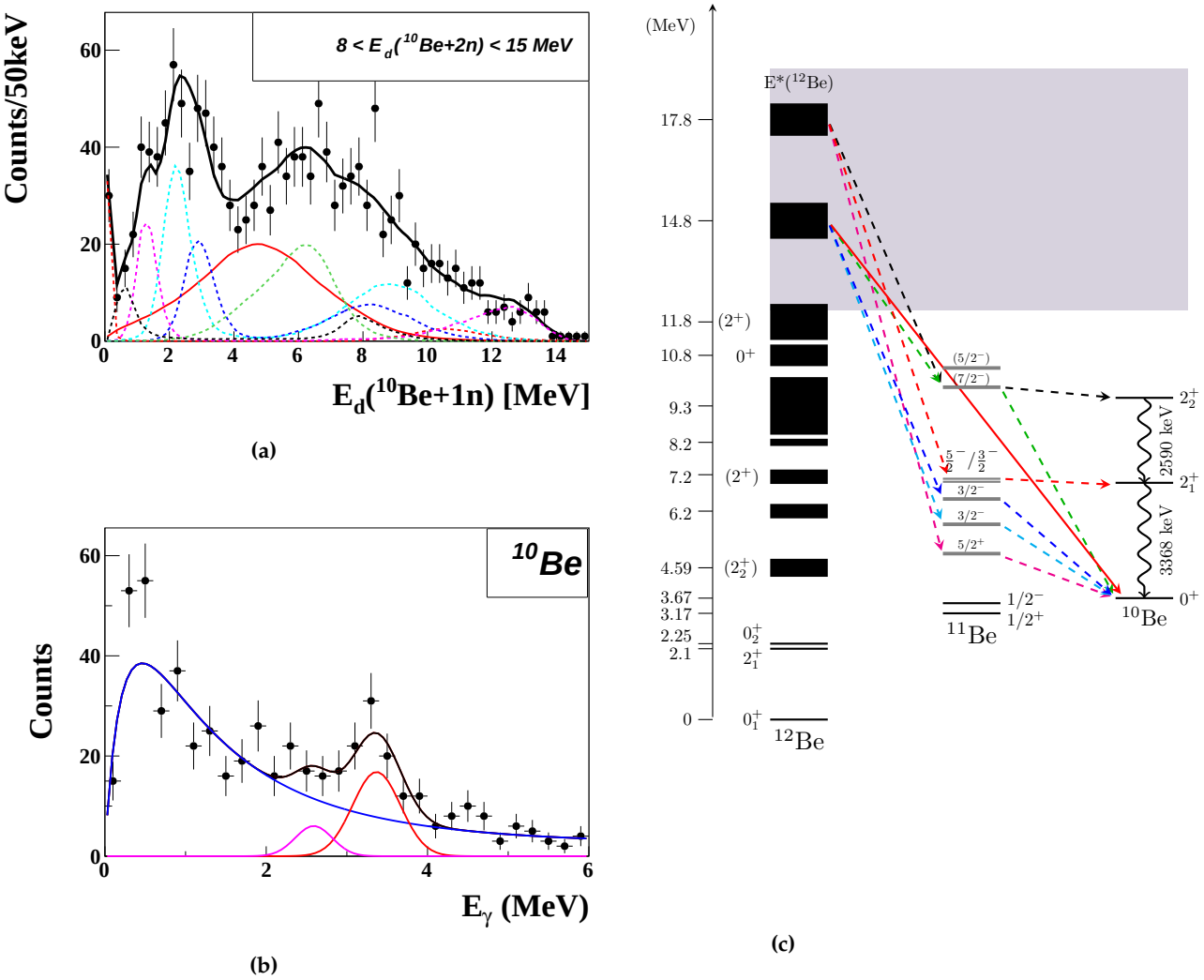


**Figure 4.19** – (a): Fit of the $E_d$($^{10}$Be+1n) for the 3-body energy from 8 to 15 MeV. We notice several sequential decays visible in the low-energy part of the spectrum and a direct decay which is constrained by the decrease around 4 MeV. (b): Fit of the $\gamma$-ray spectrum with two components corresponding to the first $2^+$ states of $^{10}$Be. (c): Level scheme with all decay channels identified in this 3-body energy range.

**Table 4.17** – Fit results of the $\gamma$-spectrum for the 3-body energy range from 8 to 15 MeV. The $1^{st}$ column shows the populated states of $^{10}$Be. The $2^{nd}$ column shows the number of detected events for the $2_1^+$ state of $^{10}$Be. The last column represents the number of events after correction by the $\gamma$-ray efficiency.

| States of $^{10}$Be | $N_\gamma$ | $N_{events}$ |
|---|---|---|
| $2_1^+$ | $61 \pm 9$ | $254 \pm 68$ |
| $2_2^+$ | $17 \pm 7$ | $71 \pm 29$ |

**Table 4.18** – Results of the fit in the range from 8 to 15 MeV. The $1^{st}$ and $2^{nd}$ columns represent the excitation energy of the resonant states in $^{12}$Be and the centroid energy of the resonance, $E_r(^{10}Be+2n)$, respectively. In case of a sequential decay the relative energies of the first and second neutrons, $E_{n1}$ and $E_{n2}$ are given in the $3^{rd}$ and $4^{th}$ columns. The $5^{th}$ column shows the proportions of each component in this 3-body energy range. The last column shows the number of events corrected by the neutron efficiency.

| $E^*(^{12}Be)$ (keV) | $E_d(^{10}Be+2n)$ (keV) | $E_{n1}$ (keV) | $E_{n2}$ (keV) | ratio (%) | $N_{events}$ |
|---|---|---|---|---|---|
| 14800 | 11130 | 8976 | 2154 | 20±3 | 147 ± 22 |
| | 11130 | - | - | 30 ± 1 | 220 ± 11 |
| | 11130 | 4630 | 6500 | 17± 2 | 125± 15 |
| 17800 | 10760 | 10740 | 20 | 3± 0.8 | 22± 6 |
| | 14130 | 12850 | 1283 | 11 ± 1 | 80± 8 |
| | 14130 | 11230 | 2900 | 15 ± 2 | 110 ± 15 |
| | 14130 | 13560 | 570 | 4 ± 1 | 29 ± 7 |

**n-n correlations**

We can also study n-n correlations by comparing the experimental (Fig. 4.20a) and simulated (Fig. 4.20b) Dalitz plots in this 3-body energy range. The inputs of the simulation are the results of the fits summarized in Tab. 4.18 and the two space-time parameters $r_0$ = 1.36 fm and $\tau_0 = \hbar c/\Gamma_r$. We notice that the signal at low $\varepsilon_{nn}$, which is a signature of n-n correlation, is not reproduced with these parameters either. In fact, we observe strong n-n correlations despite the predominance of the sequential decay ($\sim$ 70%) in this energy range. Keeping the proportions of sequential and direct decay as obtained from the fit results, we can make a variation in the space-time parameters in order to reproduce the data. As done previously, we set the parameter $\tau_0$ = 0. The Dalitz plot obtained with the new parameters $r_0$ = 1.36 fm and $\tau_0$ = 0 reproduces better the data.

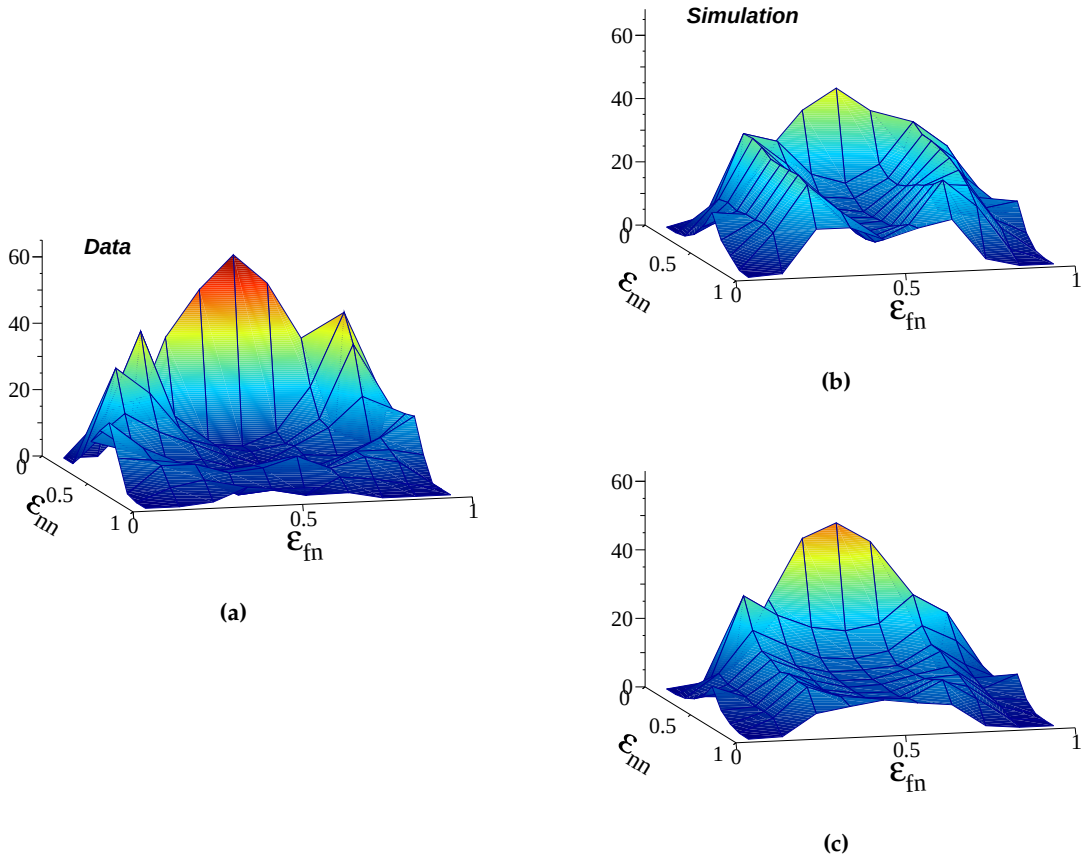


**Figure 4.20** – Comparison between Dalitz plots from data (a) and simulation (b) and (c) in the 3-body energy range from 8 to 15 MeV. The inputs of the simulation are the fit results in Tab. 4.18 with parameters $r_0$ = 1.36 fm and $\tau_0 = \hbar c/\Gamma_r$ in (b) or $\tau_0 = 0$ in (c).

### 4.4.8 Global fit of the $E_d(^{10}Be+2n)$ spectrum

We can now sum up all the fit results from the different ranges and make a global fit of the $E_d(^{10}Be+2n)$ spectrum shown in Fig. 4.6a. In total nine unbound states of $^{12}$Be, decaying via multiple channels, were identified by a thorough study of the $E_d(^{10}Be+n)$ and $\gamma$-ray spectra. It is the combination of all the decay channels identified that is used to fit $E_d(^{10}Be+2n)$ spectrum with the proportions obtained in different 3-body energy ranges. The level scheme in Fig. 4.21 summarizes all the decay patterns. Only the initial resonance in $^{12}$Be and the final state of $^{10}$Be it decays to are illustrated in Fig. 4.21, but all the components corresponding to all sequential paths through resonances in $^{11}$Be have been included in the fit of Fig. 4.21a. High-energy resonances can decay to ground or excited states of $^{10}$Be, whereas low-lying resonances only decay to the ground state.

The $\gamma$-ray spectrum of Fig. 4.21b shows that the $2_1^+$ and $2_2^+$ states are populated and this was used to unambiguously identify and constrain the contributions from the decay through excite states of $^{10}$Be. We then were able to identify all populated states of $^{12}$Be up to 18 MeV excitation energy, from the $^{13}$B$(-1p)^{12}$Be reaction. We also managed to describe its multiple decay channels.

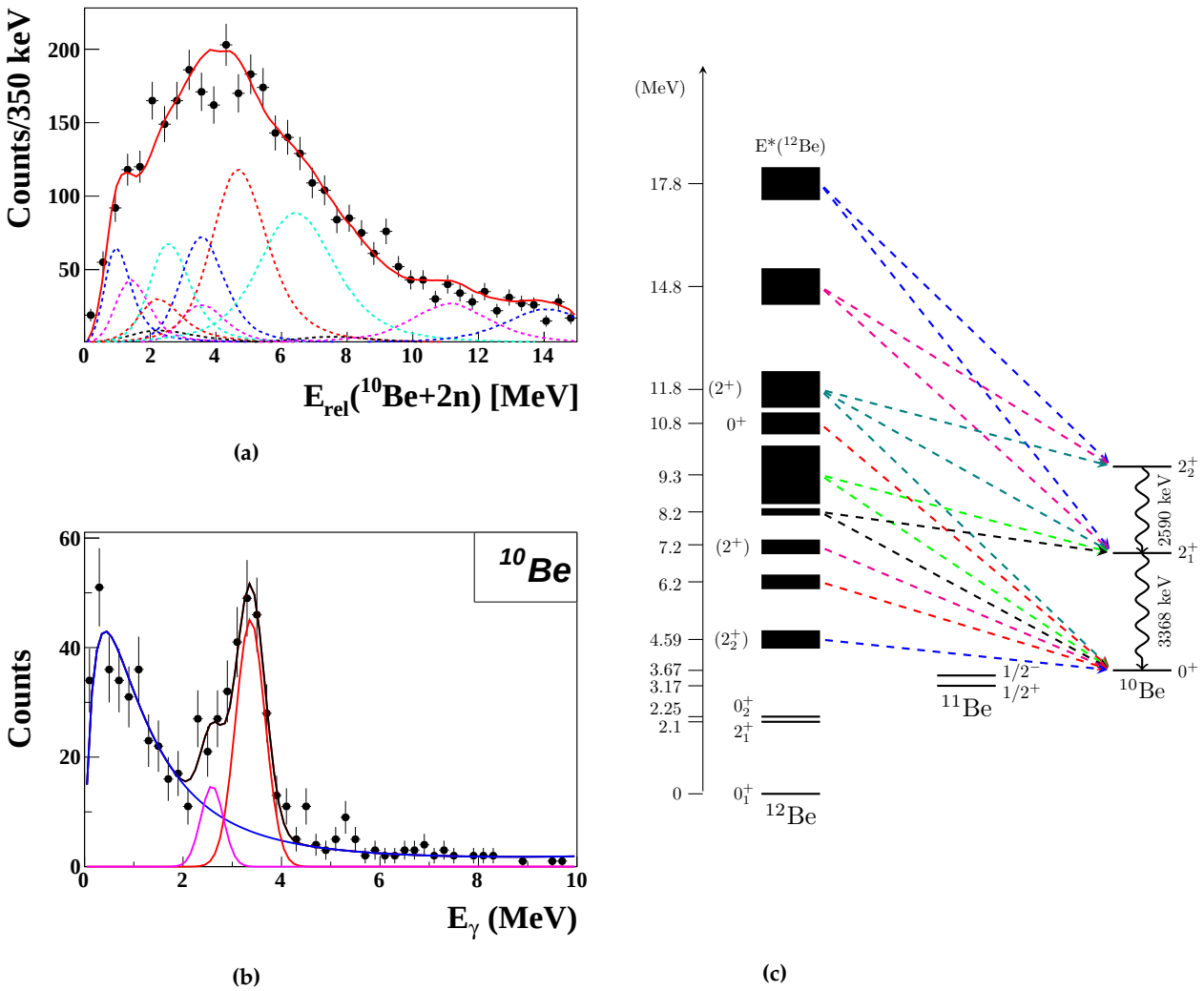


**Figure 4.21** – (a): Global fit of the $E_d(^{10}Be+2n)$ spectrum. (b): Fit of the $\gamma$-ray spectrum which determines the fraction of $2_2^+$ and $2_1^+$ states populated in $^{10}Be$. (c): Global picture of the populated 2n-unbound states of $^{12}Be$ and their decay channels. Each dashed line on this level scheme represents a decay from one resonant state of $^{12}Be$ to the ground or excited states of $^{10}Be$, independently of the eventual intermediate state in $^{11}Be$.

Tab. 4.19 summarizes the major results obtained from the global fit, i.e. the number of events, sequential and direct decay proportions, for each unbound state of $^{12}Be$ identified. In order to get the number of counts for each state, we sum every contribution from it observed in the different energy ranges analysed, and correct them by the 2n acceptance. The total number of all 2n-decay events is also obtained by integrating the $E_d(^{10}Be+2n)$ spectrum. The $0^+$ and $2^+$ states at 10800 and 11800 keV were the most populated 2n-unbound states, whereas the two states at 14800 and 17800 keV were the least populated.

**Table 4.19** – Results of the global fit of the $E_d$($^{12}$Be+2n) spectrum (from 0 to 15 MeV).

| $E^*$ | $N_{events}$ | SEQ (%) | DIR (%) |
|---|---|---|---|
| 4590 | 211 ± 28 | 0 | 100 |
| 6200 | 450 ± 21 | 33 | 77 |
| 7200 | 480 ± 22 | 15 | 85 |
| 8230 | 700 ± 26 | 100 | 0 |
| 9300 | 100 ± 10 | 100 | 0 |
| 10800 | 1150 ± 34 | 57 | 43 |
| 11800 | 800 ± 28 | 32 | 68 |
| 14800 | 350 ± 19 | 100 | 0 |
| 17800 | 200 ± 14 | 100 | 0 |

### Dalitz plots

Here we compare the Dalitz plots from data (Fig. 4.22a) and simulation (Fig. 4.22b) using the decay channels and proportions of sequential and direct decay obtain from the fit of $E_d$($^{10}$Be+2n). The fact that the simulated Dalitz plot reproduces well the experimental one is a double check of the fit results, and it shows that besides identifying all decay paths we have been able to describe the 3-body kinematics of the decays. However, one cannot pretend to get any information about n-n correlations from this, since it includes contributions from many resonances whose internal structure may differ. Instead, we are going to discuss the matter of n-n correlations in the next section, considering small energy ranges as done for the fit.

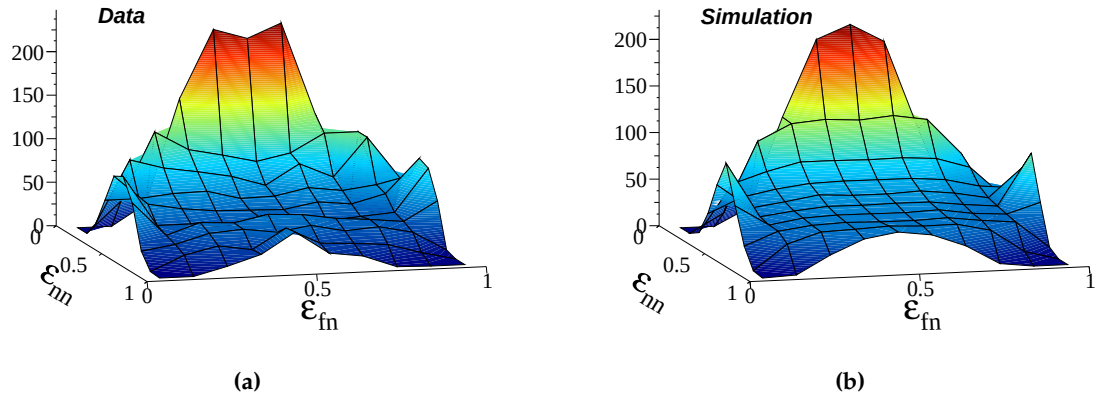


**Figure 4.22** – Comparison of the Dalitz plots from data (a) and simulation (b) for the global energy range from 0 to 15 MeV. The simulated Dalitz plot is the sum of all plots from the different 3-body energy ranges considered in the previous sections.

## 4.5 Discussion of the results

In this section, we will discuss the experimental results and see what we learn from them. First, we will discuss the structure of $^{12}$Be using the spectroscopic results presented above.

The experimental cross-sections are to be compared to the theoretical calculations, allowing us to deduce the spectroscopic factors. Second, we will discuss the n-n correlations observed via a complete 3-body decay analysis of the Dalitz plots.

### 4.5.1 Cross-sections and spectroscopic factors

The cross-section is a suitable observable to quantify the population rates of the states formed in a given reaction. We can then derive the spectroscopic factors by comparing the experimental cross-sections to the results of a theoretical calculation. The cross-section is defined as follows:

$$\sigma = \frac{1}{\alpha} \frac{N_{out}(^{12}Be)}{N_{inc}(^{13}B)}$$

where $\alpha$ is the density of scattering centers in the target, $N_{out}$ is the number of outgoing $^{12}$Be and $N_{inc}$ the number of incoming $^{13}$B. As shown in Sect. 2.4, the latter is deduced from the number of unreacted $^{13}$B beam particles reaching TFW. Its values for the two targets used, $CH_2$ and C, are given in the Tab. 4.21. The values of the parameter $\alpha$ for the two targets used are listed in Tab. 4.20.

We will deduce the cross-sections on the H target from the ones on C and $CH_2$ via the relation:

$$\sigma_H = \frac{1}{2}(\sigma_{CH2} - \sigma_C) \tag{4.7}$$

**Table 4.20** – Characteristics of the targets used in this experiment [99].

| Target | Thickness d(mm) | density $\rho$ (g/cm$^3$) | $\alpha$ (cm$^{-2}$) |
|---|---|---|---|
| $CH_2$ | 4.98 | 0.92 | 1.97(4)×10$^{22}$ |
| Carbon | 3.03 | 1.84 | 2.80(6)×10$^{22}$ |

**Table 4.21** – Number of events for incoming $^{13}$B particles.

| | $CH_2$ | Carbon |
|---|---|---|
| $N_{Inc}(^{13}B)$ (in units of $10^6$) | 13.380 ± 0.003 | 10.060 ± 0.003 |

Having the number of events from the fit obtained in previous sections for bound and unbound states of $^{12}$Be and the number of incoming events (Tab. 4.21) we can calculate the cross-sections. The inclusive cross section for bound states of $^{12}$Be is obtained by subtracting the cross sections obtained in the $CH_2$ and C targets, $\sigma_{incl}$(p,2p) = 2.57 ± 0.08 mb. The quasi-free events $^{13}$B(p,2p)$^{12}$Be were selected by the condition of detecting 2p in the XB in coincidence with $^{12}$Be fragments in TFW. We then make a correction by the 2p efficiency that was determined by simulation in the thesis of Ina Syndikus [99] and Valerii Panin [100], $\epsilon_{2p}$ = 56(3)%. Then, we determine the cross-section for the $2_1^+$ state with the number of events from the fit of the $\gamma$-ray spectrum, $\sigma_{exp}(2_1^+)$ = 0.22 ± 0.07 mb. Since the two bound

$0^+$ states of $^{12}$Be were indistinguishable in our experiment because the $0^+_2$ is isomeric, the summed cross-section for both is given by subtracting the $2^+_1$ cross-section to the inclusive one, $\sigma_{exp}(0^+_{1,2}) = 2.30 \pm 0.13$ mb.

The individual cross-sections for the $0^+_1$ and $0^+_2$ states can be estimated from their summed value and the overlaps between their wave functions and the one of the $3/2^-$ ground state of $^{13}$B, from which a proton has been knocked out. If we denote the one-proton removal operator as $a^-_p$, the individual cross-sections of the $0^+_1$ and $0^+_2$ states are proportional to the quantities $|\langle 0^+_1|a^-_p|3/2^-\rangle|^2$ and $|\langle 0^+_2|a^-_p|3/2^-\rangle|^2$, respectively. It was found in Ref. [56] that the $3/2^-$ g.s of $^{13}$B was given by $|3/2\rangle = \sqrt{0.01}|2s^2_{1/2}\rangle + \sqrt{0.12}|1d^2_{5/2}\rangle + \sqrt{0.87}|1p^2_{1/2}\rangle$, which, combined with the $|0^+_1\rangle$ and $|0^+_2\rangle$ wave functions given in Sect. 4.2 leads to overlaps of 0.579 and 0.695, respectively. We obtain individual cross-sections of $1.04 \pm 0.14$ and $1.25 \pm 0.16$ mb for the $0^+_1$ and $0^+_2$ states, respectively. The cross-sections for all bound states of $^{12}$Be are given in Tab. 4.22.

**Table 4.22** – In the upper part we present the cross-sections for the $2^+_1$ and the combined two $0^+$ bound states of $^{12}$Be from this work. In the lower part, we present the individual cross-sections of the $0^+_1$ and $0^+_2$ states(see text for details). The third column represents theoretical cross-sections from Ref. [167].

| $J^\pi$ | $E^*$ (MeV) | $\sigma_{th}$ (mb) | $\sigma_{exp}$ (mb) |
|---|---|---|---|
| $0^+_1 + 0^+_2$ | – | – | $2.30 \pm 0.13$ |
| $2^+_1$ | 2.1 | 6.03 | $0.22 \pm 0.07$ |
| $0^+_1$ | 0 | 6.30 | $1.04 \pm 0.14$ |
| $0^+_2$ | 2.2 | 6.01 | $1.25 \pm 0.16$ |

From these cross-sections we can determine the spectroscopic factors that are the real measure of the overlap between a theoretical pure state and experimentally observed states in $^{12}$Be. In fact, the theoretical cross-section can be written as the product of the single-particle ones $\sigma_{s.p,j}$ for the states j [165]:

$$\sigma_{th} = \sum_j C^2S_j \times \sigma_{s.p,j} \tag{4.8}$$

where the coefficients $C^2S_j$, with the normalisation condition, $\sum_j C^2S_j = 1$, correspond to the spectroscopic factors. Hence, the latter can be deduced by comparing the experimental cross-sections to the theoretical ones:

$$C^2S_j = \frac{\sigma_{exp}}{\sigma_{th}} \tag{4.9}$$

which measures the purity of the wave function of the measured state. For the current work, theoretical cross-sections were provided by Carlos Bertulani in a private communication (see Ref. [166] for details about the model used). The calculations were done for some states up to 14 MeV excitation energy, and we deduce others by assuming a linear trend for the reduction in cross-section as the excitation energy increases. The values are reported in the third column of Tab. 4.23.

The experimental $C^2S$ values are corrected by a quenching factor $R_S$ of $0.65 \pm 0.04$ [168], so that the obtained normalized spectroscopic factor $C^2S_{Norm}$ can be directly compared the

calculated ones $C^2S_{th}$. The latter are the shell model calculations preformed in the *psd*-shell with the YSOX interaction [173]. We obtain $C^2S_{Norm}$ of 0.25 ± 0.03 and 0.32 ± 0.03 for the $0^+_1$ and $0^+_2$ states, respectively.

The fact that the $0^+_1$ state and the isomeric $0^+_2$ state are relatively equally populated is an indication that they are highly mixed. On the contrary, comparing the population rates of the two $2^+$ states, we see that the $2^+_2$ is about 6 times more populated than the $2^+_1$, which shows that they are less mixed than the $0^+$ states and that the $2^+_2$ can be regarded as a spherical state.

**Table 4.23** – Cross-sections and normalized spectroscopic factors ($C^2S_{Norm}$) for all populated states by the $^{13}$B(p,2p)$^{12}$Be reaction. The theoretical cross-section $\sigma_{th}$ is the single-particle calculated assuming one proton removal in the $p_{3/2}$ shell [167]. The last column represent the calculated spectroscopic factors [173].

| $J^\pi$ | $E^*$ | $\sigma_{th}$ | $\sigma_{exp}$ | $C^2S_{Norm}$ | $C^2S_{th}$ |
|---|---|---|---|---|---|
| $0^+_1$ | 0 | 6.30 | 1.04 ± 0.03 | 0.25 ± 0.03 | 0.2824 |
| $2^+_1$ | 2109 | 6.03 | 0.22 ± 0.07 | 0.056 ± 0.020 | 0.2756 |
| $0^+_2$ | 2250 | 6.01 | 1.25 ± 0.09 | 0.32 ± 0.03 | 0.1747 |
| $2^+_2$ | 4590 | 5.77 | 1.41 ± 0.14 | 0.38 ± 0.04 | 1.739 |
| - | 6200 | 5.43 | 0.12 ± 0.02 | 0.033 ± 0.006 | 0.0444 |
| $2^+$ | 7200 | 5.30 | 0.13 ± 0.02 | 0.036 ± 0.006 | 0.0254 |
| - | 8230 | 5.20 | 0.18 ± 0.02 | 0.055 ± 0.006 | 0.0172 |
| - | 9300 | 5.10 | 0.03 ± 0.01 | 0.009 ± 0.003 | 0.0771 |
| $0^+$ | 10800 | 4.98 | 0.30 ±0.06 | 0.09 ± 0.02 | 0.0119 |
| $2^+$ | 11800 | 4.88 | 0.21 ±0.05 | 0.06 ± 0.02 | |
| - | 14800 | 4.81 | 0.09 ±0.01 | 0.027 ± 0.003 | |
| - | 17800 | 4.58 | 0.05 ±0.02 | 0.017 ± 0.007 | |

Removing one of the three protons in the $p_{3/2}$ shell by the $^{13}$B(p,2p)$^{12}$Be reaction, we expect the sum of the spectroscopic factors to be equal to 3 at maximum, and can be distributed along the excitation energies. In Tab. 4.23, we report the experimental spectroscopic factors together with the theoretical ones. We notice that the states $0^+_2$ and $2^+_2$ take most of the strength, but they don't match the predicted distribution (last column in Tab. 4.23). The second $2^+$ is predicted to take most of the strength. However, we notice that it takes much less than predicted.

Ref. [172] described the wave function of the first $2^+$ state of $^{12}$Be with 3 components: the spherical p-shell closed, the $^{10}$Be-core(g.s)$\times\nu(sd)^2_2$, and an excited $^{10}$Be-core( $2^+$)$\times\nu(sd)^2_2$, with the strength of 0.15, 0.66 and 0.19, respectively. The predominance of the two $^{10}$Be-core components in the wave function is in agreement with the observed decay channels of unbound states of $^{12}$Be to ground and excited states of $^{10}$Be. We also notice that the sum of the normalized experimental spectroscopic factors $C^2S_{Norm}$ is 1.466 which is about half of the

expected one. This discrepancy can be attributed to missing higher excited states above the 3n-emission threshold that can decay to $^{9}$Be. In fact, the state at 10800 keV is already above this threshold which is $S_{3n}$=10.482 MeV.

### 4.5.2 n-n correlations in $^{12}$Be

The n-n correlations were studied by analysing the Dalitz plots of the previous sections. They showed an alignment of the two neutrons increasing as a function of decay energy, as it is seen by the signal at low $\varepsilon_{nn}$ (see Fig. 4.23). These correlations are even stronger than the ones observed in Ref. [93], which were the strongest observed to date.

The alignment of the two neutrons, i.e. strong signal at low $\varepsilon_{nn}$, was previously attributed to a simultaneous emission of a pair of neutrons [93, 124, 133], in which case the final state interaction (FSI) aligns the momenta of the two neutrons. The most intriguing observation derived from the results of Sect. 4.4 is the fact that these correlations are present, even after going through an intermediate resonance in a sequential decay. In fact, given the Heisenberg uncertainty principle and known width of the intermediate resonances in $^{11}$Be, the time scale between the emission of the first and second neutrons should be long enough to weaken the effect of the FSI. In Ref. [124], they observed a suppression of the signal at low $\varepsilon_{nn}$ for a sequential decay of $^{8}$He through an intermediate resonance in $^{7}$He.

A resonant state in $^{12}$Be with a decay energy $E_d$ above the 2n-emission threshold ($S_{2n}$ =3670 keV), may decay sequentially through an intermediate resonance in $^{11}$Be by the emission of two neutrons labelled as $n_1$ and $n_2$. In the three-body centre-of-mass frame, the momentum of the first neutron $n_1$ is equal in value but opposite in direction to the momentum of the unbound system $^{10}$Be+$n_2$.

$$\overrightarrow{p}_{n_1} = -\overrightarrow{p}_{^{10}Be+n_2}$$

The unbound state in $^{11}$Be in turn decays into $^{10}$Be+1n. This two-step process (see Fig. 4.24) may lead to angular correlations between the second neutron emitted and the propagation direction of the intermediate resonance, governed by the quantum numbers of the latter [174]. The angular correlations are defined as the distribution of $\cos(\theta_{fn})$, where $\theta_{fn}$ is the angle between the total and relative momenta of the fragment-$n_2$ system:

$$\overrightarrow{P} = \overrightarrow{p}_{^{10}Be} + \overrightarrow{p}_{n} \tag{4.10}$$

$$\overrightarrow{Q} = \frac{m_n m_{^{10}Be}}{m_n + m_{^{10}Be}}\left(\frac{\overrightarrow{p}_{n}}{m_n} - \frac{\overrightarrow{p}_{^{10}Be}}{m_{^{10}Be}}\right) \tag{4.11}$$

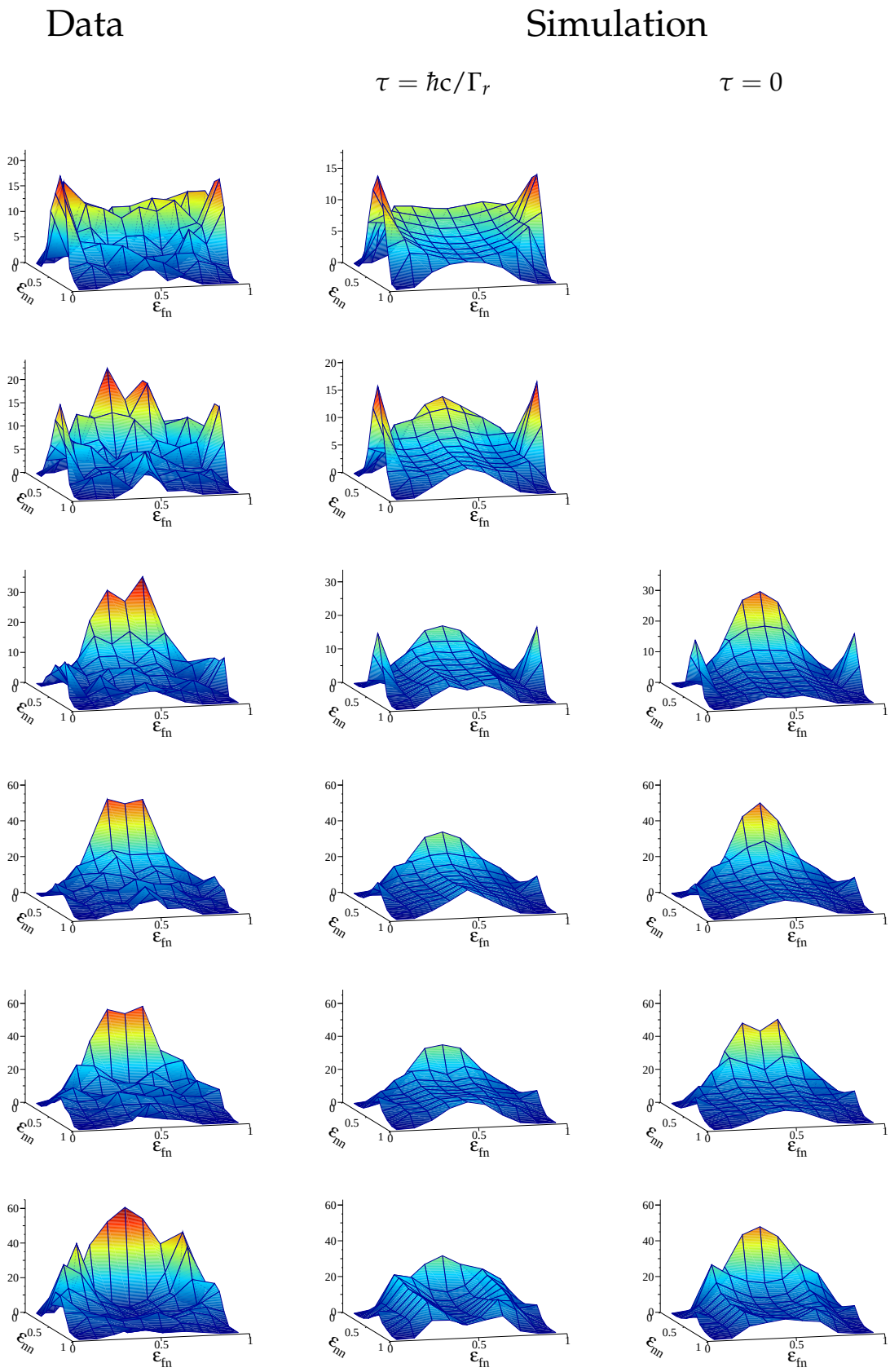


**Figure 4.23** – Summary of the Dalitz plots for the 3-body decay-energy ranges from 0 to 2, 2 to 3, 3 to 4, 4 to 5.5, 5.5 to 8 and 8 to 15 MeV, respectively from top to bottom. The signal at low $\varepsilon_{nn}$ shows an evolution pattern from low to high decay energies.

$$cos(\theta_{fn}) = \frac{\overrightarrow{P}.\overrightarrow{Q}}{P.Q} \tag{4.12}$$

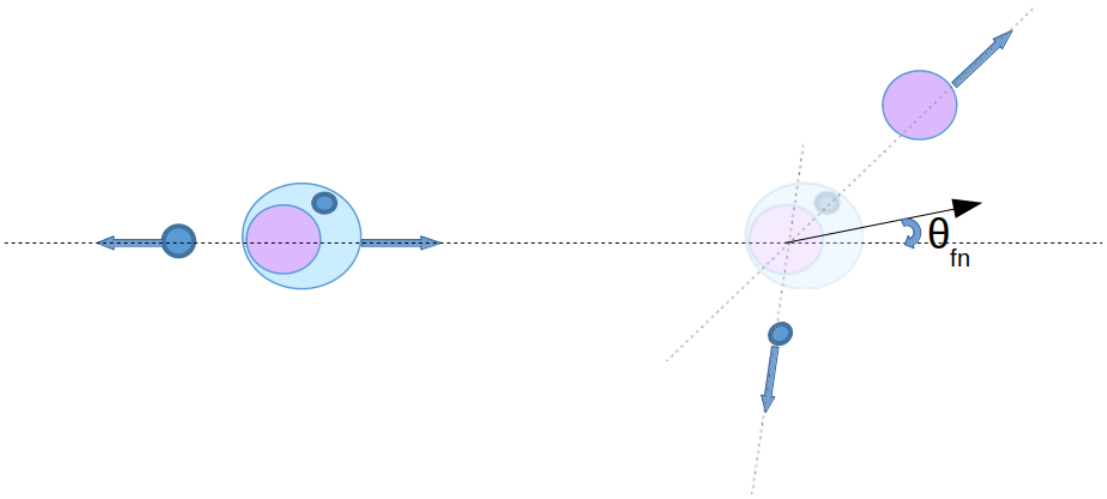


**Figure 4.24** – Kinematics of 2×2-body decay of resonant state in $^{12}$Be. The angle $\theta_{fn}$ is defined as the angle between the total and relative momenta of the system fragment+n$_2$.

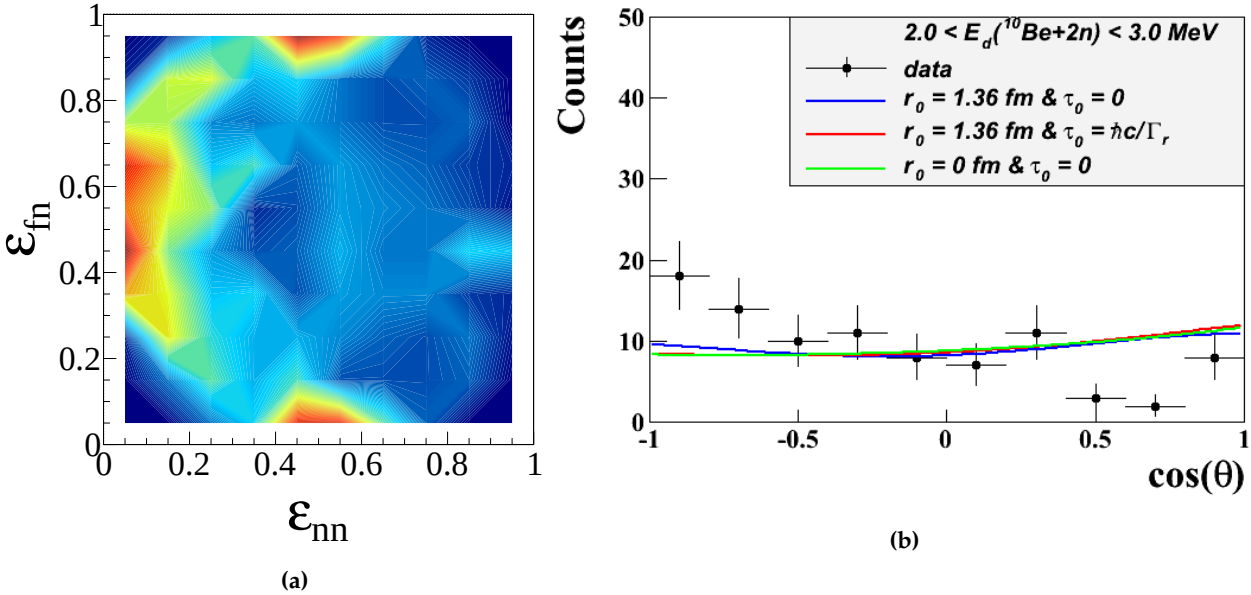


**Figure 4.25** – (a): 2-dimensional Dalitz plot for the 3-body energy range from 2 to 3 MeV. (b): angular distribution corresponding to the condition $\varepsilon_{fn} < 0.1$. The lines represent simulations with the values of the parameters as indicated in the insert.

The angle $\theta_{fn}$ defined in Eq. 4.12 shows the direction of emission of the second neutron with respect to the first one. In the case of an isotropic emission, the distribution should be flat. So, any deviation from a flat distribution would point to a preferred direction between

the two neutrons. Practically, the aim is to select the events corresponding to the second neutron emitted $n_2$, and use the momenta defined in Eqs. 4.10 and 4.11 to calculate the angle $\theta_{fn}$.

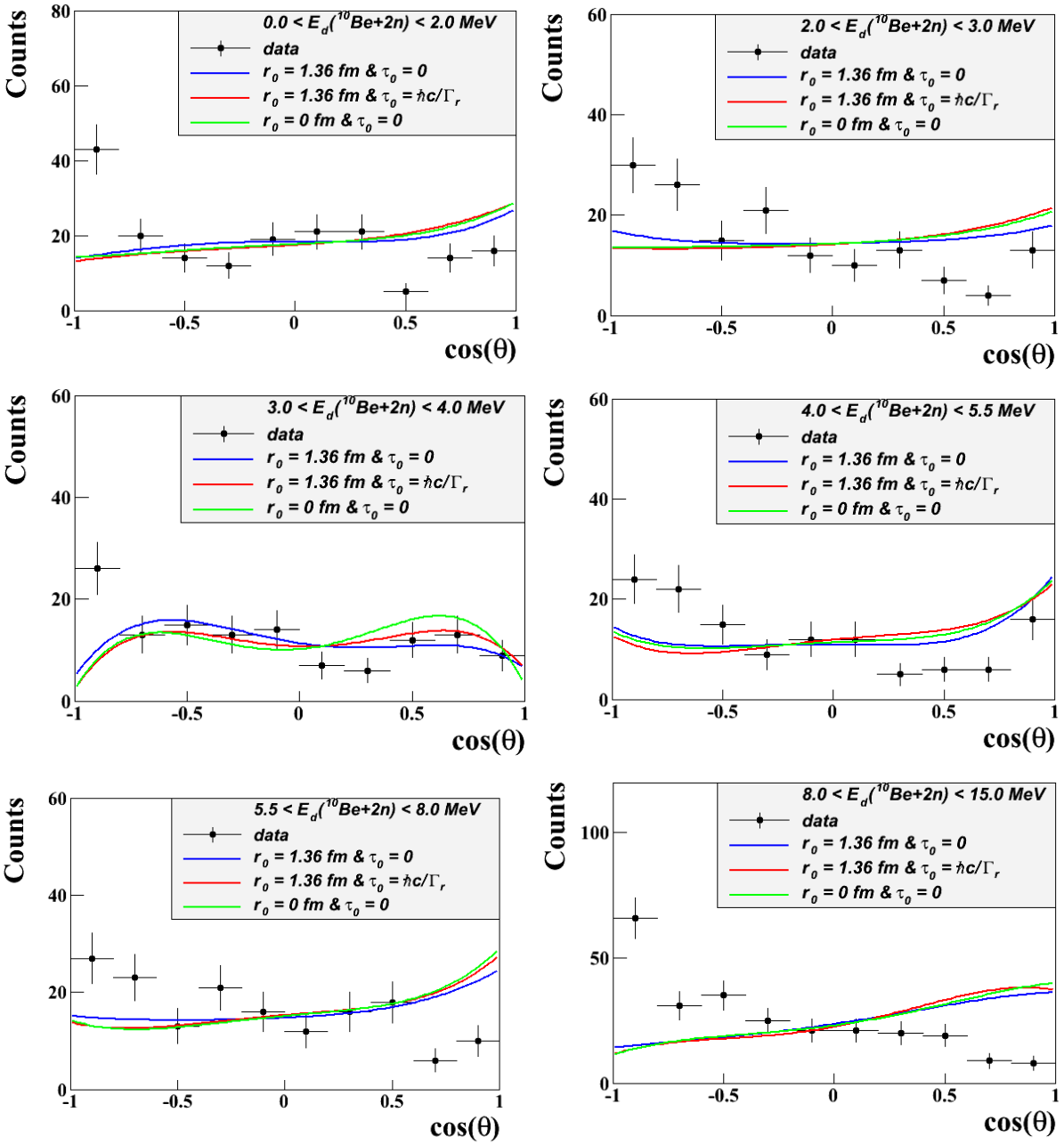


**Figure 4.26** – The experimental angular correlations in the different energy-ranges is compared to the simulations with different values of the parameters $r_0$ and $\tau_0$.

The challenge here is how we distinguish the first and second neutron emitted, because the events are not stored in a chronological order but rather as a function of increasing energies. Hence, we start by looking at the 3-body energy ranges where we have information on the relative energies of the two neutrons from the fit results of Sect. 4.4. The best example of such a range is the one from 2 to 3 MeV, in which we clearly identify the 20 keV resonance corresponding to the relative energy of the second neutron emitted. We then select events that correspond to $E_{n2} \approx 20$ keV, i.e. low $\varepsilon_{fn}$ in the Dalitz plot ($\varepsilon_{fn} < 0.1$, Fig. 4.25a). We

then deduce the experimental angular distribution in this energy range, which is compared to the simulations with different values of the parameters $r_0$ and $\tau_0$ (Fig. 4.25b). We observe a discrepancy between simulations and data which sustain the fact that the Dalitz plots are not well reproduced by the simulations.

The discrepancy between the simulations and data becomes even more visible when we select events corresponding to $\varepsilon_{fn} \leq 0.2$, and increases as a function of the decay energy. It is characterised by the peak at around $-1$ in the experimental distribution that is unmatched by the simulations (Fig. 4.26). This is a sign of anisotropy of the neutron-emission direction and an indication that their momenta are correlated. In the 3-body energy range from 8 to 15 MeV, we observe the largest difference between data and simulation, despite the fact that $\varepsilon_{fn} \leq 0.2$ corresponds to a region with more sequential decay. In summary, experimental angular distributions show a signal at around $-1$, which is an indication of the alignment of the momenta of both neutrons, even when they are emitted sequentially. A better understanding of this anisotropy should be needed in order to include this effect in the simulations.

# Conclusion and outlook

This PhD work came as the continuation of previous works done in order to understand the structure and the superfluid behavior of nuclei close to the neutron dripline. The main focus of this work was to study the structure of bound and unbound states of $^{12}$Be and their n-n correlations from their 2n-emission pattern. This nucleus was chosen because it is at the crossroad of nuclei with different configurations in the chart of nuclei. Moreover, the previous studies on this nucleus and more generally on nuclei around N=8 magic number, pointed out the need to look for states with different configurations in $^{12}$Be and to study the pairing regime in it.

For this purpose, the s393 experiment was performed at GSI with the R3B-LAND setup and the dedicated detection system. The latter comprised $\gamma$-ray, neutron and fragment detectors together with a tracking system for position and energy reconstruction for the outgoing reaction products. Knockout reactions are suitable to study these loosely-bound nuclei, thus we chose to use the $^{13}$B$(-1p)$ reaction to populate states of $^{12}$Be, for which we have measured the feedings and studied the decay modes. Bound states were observed by detecting $^{12}$Be and deexcitation $\gamma$-rays for the $2_1^+$ excited state, while unbound states were studied in inverse kinematics by reconstructing the decay energy of the 2- and 3-body systems from momenta and energies of the decay products, the neutron(s) and residual nucleus.

Prior to proper data analysis, in the second chapter, I have described the experimental setup including beam production, reaction targets and the detector system. The data were recorded under specific conditions of a trigger system, which I also describe in detail in the second chapter. A combination of these triggers allowed us to record the data event by event, which are then converted and calibrated in order to give physical quantities such as distances, energy loss, momenta, angles, etc.

In the third chapter, I present the analysis techniques, starting from the identification of the incoming beam to the relevant parameters of the outgoing reaction products. Then, I describe in details the method used for fitting the $\gamma$-ray spectra, together with the estimation of the $\gamma$-ray efficiency and resolution of the detector. The former was done using simulation of $\gamma$ sources combined with results from the analysis of $\gamma$-neutron coincidences for the resonances in $^{12}$Be decaying to $^{11}$Be and $^{10}$Be. For the 1n- and 2n-unbound states, the decay energy is reconstructed by using the invariant-mass method. The obtained spectra are fitted by simulations taking into account the resolution and efficiency of the detectors. The Dalitz-plots method used for studying the n-n correlations in the 3-body decays are also presented.

Once all the methods and tools needed to analyse the data are described, we proceed to the study of the states in $^{12}$Be populated by the $^{13}$B$(-1p)$ reaction. We observe mainly $2^+$ and $0^+$ states populated from this reaction. These states are of two different types: spherical and deformed. Due to state mixing, all observed states in $^{12}$Be may contain a certain amount of spherical and deformed configurations. The ones with dominant spherical component will

be more populated since they are populated from $^{13}$B which has 88(41)% of the spherical configuration, against 11(11)% of the deformed one as shown in Ref. [56]. The ground ($0^+_1$) and the isomeric $0^+_2$ states were indistinguishable and their total population rate was deduced by counting the fragments of $^{12}$Be detected in the TFW without $\gamma$ coincidence. We have obtained a combined cross-section of 2.30$\pm$ 0.13 mb for the two states, whose individual contributions were estimated by using results of previous studies on these states populated through Gamow-Teller transitions in charge exchange reaction from $^{12}$B. We have found 0.67 $\pm$ 0.14 and 1.63 $\pm$ 0.16 mb for the $0^+_1$ and $0^+_2$, respectively. Being produced from the spherical nucleus $^{13}$B, it is deduced here that the second $0^+$ state has more spherical component than the ground state does. Among the known bound states of $^{12}$Be, only the $2^+_1$ at 2.09 MeV was observed to decay by $\gamma$-ray deexcitation. The cross-section to this state is 0.22 $\pm$ 0.07 mb, that is about 8 times smaller than that of the $0^+_2$. This weak population confirms that the $2^+_1$ state is likely to be part of the deformed band based on the $^{12}$Be ground state, though having less mixing than the ground state does with the spherical $0^+$ component.

The first unbound state, the $2^+_2$, is observed to decay to $^{11}$Be despite being above the 2n-emission threshold. This state corresponds to a resonance previously observed by Smith *et al* [95]. We have been able to identify the decay modes of this state by using the $\gamma$-rays detected in coincidence with the fragment of $^{11}$Be and one neutron. The decay to the excited and ground states of $^{11}$Be contributed to 62$\pm$ 2 and 38$\pm$2 %, respectively. There is also a small contribution (3.9$\pm$0.5 %) of the 2n decay to $^{10}$Be. This state and the $0^+_2$ state were by far the most populated with a cross-section of 1.41$\pm$0.14 and 1.63$\pm$0.09 mb, respectively. We interpreted the high population rate as an indication of their sphericity, since they are populated from $^{13}$B, which has a predominantly spherical configuration. We have not seen any other resonance at higher excitation energy decaying to $^{11}$Be, despite having a good 1n-detection acceptance. This feature likely points to a dominating $^{10}$Be+2n configuration, with $^{10}$Be in the ground state or in its $2^+$ states, of all other populated resonances in $^{12}$Be, rather than halo configurations.

Indeed, other resonances above the 2n-emission threshold have been observed to decay to the ground or $2^+$ states in $^{10}$Be. Contrary to the $E_d$($^{11}$Be+1n) spectrum that had two components relatively easy to distinguish, the $E_d$($^{10}$Be+2n) spectrum contains several overlapping and indistinguishable contributions. In this thesis, we have used for the first time a method that consists in a combined analysis of the $E_d$($^{10}$Be+1n), $E_d$($^{10}$Be+2n) and $\gamma$-ray spectra together with the Dalitz plots formed by the 3-body components of the neutrons and residual nucleus. The former has the advantage of clearly showing resonant structures that are characteristic of the decay channels involved. More precisely, we have made cuts in the 3-body energy $E_d$($^{10}$Be+2n) and have fitted the corresponding $E_d$($^{10}$Be+1n) spectrum. The ranges were chosen to contain the minimum of decay channels and while having enough statistics. The obtained results are reported to the fit of $E_d$($^{10}$Be+2n) and Dalitz plots for a double check.

With the use of this pioneering method, we have been able to identify nine $^{12}$Be resonances up to 18 MeV excitation energy, decaying to $^{10}$Be by 2n-emission. In the fitting procedure of the $E_d$($^{10}$Be+1n) spectrum, we have used the known states of $^{12}$Be and intermediate resonances in $^{11}$Be as input for the simulations. The resonances in $^{12}$Be that are below the first excited state of $^{10}$Be ($2^+_1$ at 3.3 MeV), could only decay to the ground state either by simultaneous emission of the 2n or sequentially through intermediate resonances in $^{11}$Be. Apart from the $2^+_2$ state, we have identified other states at 6.2 and 7.2 MeV by their decay channels seen in the low-energy 3-body ranges. On the contrary, the high-energy resonances could sometimes decay through the excited states of $^{10}$Be. One particular decay channel was observed in most 3-body energy ranges, that is the decay through an intermediate resonance(s) less than 80 keV above the $2^+_1$

state of $^{10}$Be (20 keV, 80 keV or a superposition of the two; in the fitting procedure I used 20 keV for simplicity). The occurrence of this decay channel has been interpreted as the signature of the $^{10}\mathrm{Be}(2_1^+) \times \nu(sd)_2^2$ component of the $2^+$ states in $^{12}$Be. The cross-sections for all observed resonances were calculated using their population rates obtained from the fit.

The proportions of sequential and simultaneous decays from the results of the fit were used as inputs for the simulations of the Dalitz plots that were compared to the experimental ones. The systematic strong enhancement observed at low n-n relative energies has been described within a simple phenomenological model, which generates such a signal through the final-state interaction between independent neutrons emitted from a Gaussian source and has only two parameters, the space-time extent ($r_0$, $\tau_0$) of the latter. The parameter $r_0$ was estimated to 1.36 fm, assuming that the 2n emitted are independently moving inside a sphere of size $R = 1.2 \times A^{1/3}$. The parameter $\tau_0$ is related to the lifetime of the intermediate resonance in $^{11}$Be and which, if long enough (typically $\sim$ 1000 fm/c), is expected to soften the n-n correlations. We have been able to reproduce the Dalitz plots with these parameters for low-energy 3-body energy ranges (up to 4 MeV), and for higher energy ranges, we have adjusted the $\tau_0$ parameter to 0 in order to reproduce the Dalitz plots. This presence of the strongest correlation observed to date, not only for the neutron pairs that decay simultaneously, but as well in the case of sequential decay, is an indication that the 2n are already strongly correlated in the initial state and/or that their momenta are aligned by the kinematics of momentum conservation. The second hypothesis has been investigated by analysing the angular correlation in the case of sequential decay.

In the future, one should study this interesting nucleus with an improved-resolution detectors, such as by the use of the NeuLAND detector at the FAIR GSI-R3B setup. Indeed, an experiment is being planned with this facility with a liquid hydrogen target ($LH_2$), leading to a better vertex reconstruction and improved momentum resolution. The momentum distribution of states in $^{12}$Be, before decaying can be deduced from the momenta of decay products, and leads to a determination of the orbital momentum of the orbital from which the protons were knocked out in the $^{13}\mathrm{B(p,2p)}^{12}$Be reaction. Furthermore, one could constrain the binding energy of the removed proton by detecting in the new $\gamma$ detector CALIFA the two protons produced by the reaction. The expected resolution derived from the kinematics of the two protons is about 4 MeV, which is sufficient to distinguish between the $s$ and $p$ orbitals for the states observed in $^{12}$Be with the highest excitation energy.

Regarding the n-n correlations, a study of heavier nuclei would be more suitable to unveil a possible transition from wide neutron pairs to more compact ones, i.e. from BCS to BEC regime. On the theoretical point of view, it would be worthwhile to use realistic wave functions to describe the neutrons inside the $^{12}$Be nucleus rather than the simplified assumption of a Gaussian distribution of neutrons.

# Annexe1: Understanding $\gamma$-multiplicity

In nuclei with more than one excited bound state, $\gamma-$ deexcitation can be direct or in cascade. In the first case one $\gamma-$ ray is emitted with the detected $\gamma-$ energy equal to the excitation energy. In the second case, two or more $\gamma$-rays are emitted in cascade and the sum of their energies is equal to the excitation energy. For nuclei with only one excited state, all events of interest will be at multiplicity $M = 1$ and events at $M > 1$ correspond to background (see Fig. A.1 for an example of $^{11}$Be).

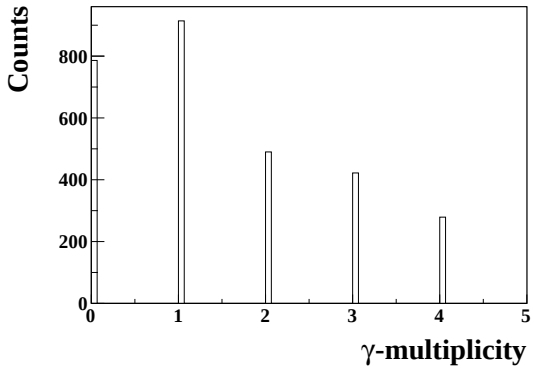


**Figure A.1** – Number of events counts at different $\gamma$-multiplicity for $^{11}$Be. We see that events at M = 1 are double those at M = 2. Since only one excited bound state exists in $^{11}$Be, all events at M > 1 correspond to the background

When a $\gamma$ is detected, it is important to know whether it was a direct deexcitation or if other $\gamma$-rays were emitted together , in which case we should identify them and sum the energies to get the actual excitation energy. The case of $^{14}B$ is an illustration of this matter as we observe, not a clear peak at 650 keV, but also shapes at low energy that could be other peaks.

Now that we know the resolution of Crystal-Ball, we can fit the the spectrum with restrictions on the width. A peak at low energy will not be as wide as one at high energy, and in that way we can tell how many peaks we observe. Three $\gamma-$ peaks are observed at $250 \pm 25$ keV, $400 \pm 20$ keV and $650 \pm 15$ keV. The sum of the two peaks at low energy is equal to 650 keV. This looks like an excited state at 650 keV with both direct and cascade deexcitations.

However, a rigorous method to confirm this guess is to define $\gamma$- multiplicity. Multiplicity indicates the number of $\gamma$-rays detected in Crystal-Ball. Thus, $\gamma$-rays emitted directly will be seen at multiplicity 1 and those in a cascade will be seen at higher multiplicity. In $^{14}B$, at M= 1 and M= 2, all three peaks are seen (see Fig. A.2). At this stage, we want to tell if they are in cascade or if they were emitted directly.

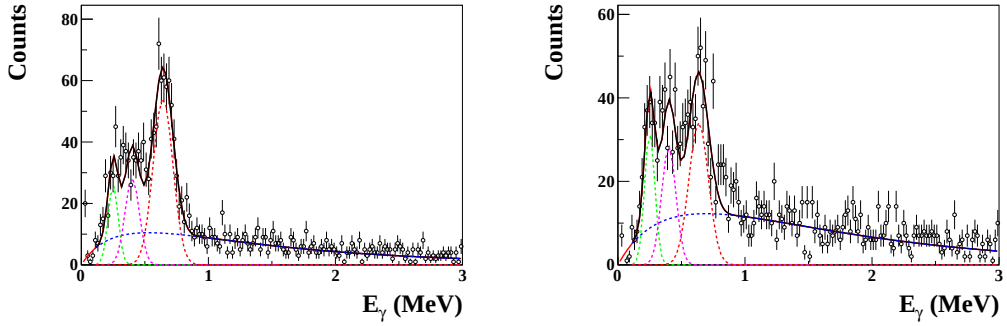


**Figure A.2** – Fit of the $\gamma$- spectrum of $^{14}B$: On the left side is $\gamma-$ spectrum at multiplicity 1 fitted by three peaks ($250 \pm 25$ keV, $400 \pm 20$ keV and $650 \pm 15$ keV) on top of the background of the form 3.10. On the right side is the spectrum at multiplicity 2 with the same peaks. The peak at 650 keV decreases at multiplicity 2.

Starting from the observation that the two low-energy peaks sum up to give the other one, we make an assumption that the peak at 650 keV is a direct deexcitation and the other two are a cascade deexcitation of the same state. Then we can give the following interpretation:

- At multiplicity 1, the peak at 650 keV which is seen corresponds to direct emission and the two other peaks are seen due to $\gamma$-ray efficiency. In fact, since $\gamma$-ray efficiency is not 100%, one of the two $\gamma$-rays in coincidence (cascade) will not be seen, making a M=2 event look like a M=1 event. The real number ($N_d$)of events in direct deexcitation will then be what we observe at 650 keV divided by the efficiency at that energy ( see efficiency curve Fig. 4.1).

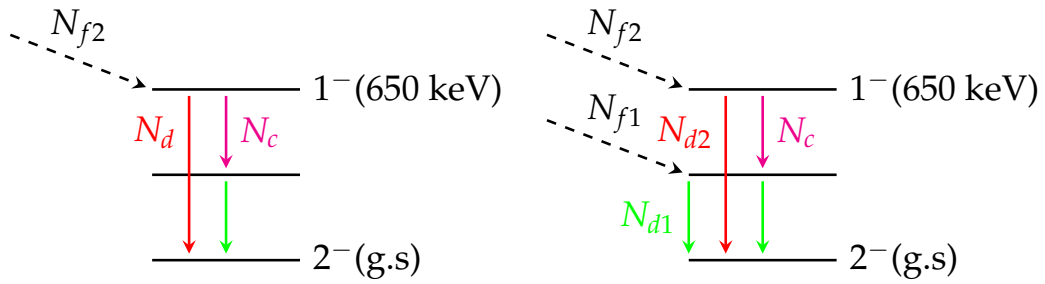


**Figure A.3** – Left : On $N_{f2}$ events populating the state at 650 keV, $N_d$ will undergo a direct deexcitation while $N_c$ are in a cascade. Right : The intermediate state could be populated independently by $N_{f1}$ events which will be seen as a direct deexcitation.

$$N_f = N_d + N_c \tag{A.1}$$
$$N_{650} = N_f \times B_d \times \epsilon_\gamma(650\ keV) \tag{A.2}$$
$$N_{250} = N_f \times B_c \times \epsilon_\gamma(250\ keV) \times [1 - \epsilon_\gamma(400\ keV)] \tag{A.3}$$
$$N_{400} = N_f \times B_c \times \epsilon_\gamma(400\ keV) \times [1 - \epsilon_\gamma(250\ keV)] \tag{A.4}$$
$$N_{BG} = N_0 \times \epsilon_{BG} \tag{A.5}$$

$$B_d = \frac{N_d}{N_f} \quad and \quad B_c = \frac{N_c}{N_f} \tag{A.6}$$

From equations A.20, and A.6 and using values in Tab. A.1, we can deduce branching ratios of direct and cascade deexcitation, $B_d$ and $B_c$. The number of detected events is calculated as the integral under each photopeak.

– 1st case: Only one excited state is populated and its deexcitation takes the two modes, i.e direct and cascade (figure . In this case the following equations hold:

$$N_d = N_f \times B_d = \frac{N_{650}}{\epsilon_\gamma(650\ keV)} \tag{A.7}$$

$$N_c = N_f \times B_c = \frac{N_{250}}{\epsilon_\gamma(250\ keV) \times [1 - \epsilon_\gamma(400\ keV)]} \tag{A.8}$$

$$= \frac{N_{400}}{\epsilon_\gamma(400\ keV) \times [1 - \epsilon_\gamma(250\ keV)]} \tag{A.9}$$

In this case $N_c$ can be deduced either from equation A.21 or A.9 yielding the same result.

– 2nd case: Two excited states are populated. One ($N_{f2}$) undergoes two modes of deexcitation, direct and cascade, the other one ($N_{f1}$) has a direct deexcitation. The intermediate state, i.e first excited stated, has two feeding modes, from the cascade of the state above $N_c$ and from a direct feeding $N_{f1}$. In this case there would be discrepancy in equations A.21 and A.9 due to the direct feeding of the intermediate state.

$$N_{250} = N_{f1} \times \epsilon_\gamma(250) + N_{f2} \times B_c \times \epsilon_\gamma(250) \times [1 - \epsilon_\gamma(400)] \tag{A.10}$$

$$\frac{N_{250}}{\epsilon_\gamma(250)} = N_{f1} + N_{f2} \times B_c \times [1 - \epsilon_\gamma(400)] \tag{A.11}$$

$$= N_{f1} + N_c \times [1 - \epsilon_\gamma(400)] \tag{A.12}$$

$$\tag{A.13}$$

| $\gamma-$ energy (MeV) | 0.250 | 0.400 | 0.650 | BG |
|---|---|---|---|---|
| Counts | 129.0 $\pm$11.3 | 200 $\pm$14 | 526 $\pm$30 | 424.0 $\pm$ 20.6 |

**Table A.1** – Number of counts under the photopeak for the three $\gamma$-peaks at $M = 1$

Applying the values in Tab. A.1 in equations A.21 and A.9, we get :

$$\frac{N_{250}}{\epsilon_\gamma(250\ keV) \times [1 - \epsilon_\gamma(400\ keV)]} = \frac{129}{0.20 \times (1 - 0.38)} = 1040 \tag{A.14}$$

$$\frac{N_{400}}{\epsilon_\gamma(400\ keV) \times [1 - \epsilon_\gamma(250\ keV)]} = \frac{200}{0.38 \times (1 - 0.20)} = 658 \tag{A.15}$$

From the results A.14 and A.15, we see a discrepancy which indicates that we are rather in presence of case 2 (Fig. A.3). The peak at 250 keV is then the intermediate excited state in $^{14}$B. The number of counts from cascade of the state at 650 keV is then given by $N_c = 658$ counts, while the number of direct feeding of the state at 250 keV is $N_{f1}$ is determined by

$$N_{f1} = \frac{N_{250} - N_c \times \epsilon_\gamma(250\ keV) \times [1 - \epsilon_\gamma(400\ keV)]}{\epsilon_\gamma(250\ keV)} = 237$$

The number of direct deexcitation from state at 650 keV is:

$$N_d = \frac{N_{650}}{\epsilon_\gamma(650\ keV)} = \frac{526}{0.48} = 1096$$

Hence, branching ratios of direct and cascade deexcitations from state $1^-$ are:

$$B_d = \frac{N_d}{N_{f2}} = \frac{N_d}{N_c + N_d} = \frac{1096}{1096 + 658} = 0.62$$
$$B_c = \frac{N_c}{N_{f2}} = \frac{N_c}{N_c + N_d} = \frac{658}{1096 + 658} = 0.38$$

And

$$\frac{N_{f1}}{N_{f2}} = \frac{237}{1096 + 658} = 0.135$$

- At multiplicity 2: The peak at 650 keV can still be seen at multiplicity 2 if it is in coincidence with the background. This explains why the peak decrease but can still be seen at multiplicity 2.

$$N_{650} = N_d \times \epsilon_\gamma(650\ keV) \times \epsilon_{BG} \tag{A.16}$$
$$N_{250} = \epsilon_\gamma(250\ keV) \times [N_c \times \epsilon_\gamma(400\ keV) + N_{f1} \times \epsilon_{BG} + N_0 \times \epsilon_{BG}] \tag{A.17}$$
$$N_{400} = \epsilon_\gamma(400\ keV) \times [N_c \times \epsilon_\gamma(250\ keV) + N_0 \times \epsilon_{BG}] \tag{A.18}$$
$$N_{BG} = 2 \times N_0 \times \epsilon_{BG}^2 \tag{A.19}$$

| $\gamma-$ energy (MeV) | 0.250 | 0.400 | 0.650 | BG |
|---|---|---|---|---|
| Counts | 160.0 $\pm$12.6 | 200 $\pm$14 | 328 $\pm$18 | 485 $\pm$22 |

**Table A.2** – Number of counts under the photopeak for the three $\gamma$-peaks at $M = 2$

$$N_d = \frac{N_{650}}{\epsilon_\gamma(650\ keV) \times \epsilon_{BG}} \tag{A.20}$$

$$N_c = \frac{\frac{N_{250}}{\epsilon_\gamma(250\ keV)} - N_{f1} \times \epsilon_{BG} - N_0 \times \epsilon_{BG}}{\epsilon_\gamma(400\ keV)} \tag{A.21}$$

$$= \frac{\frac{N_{400}}{\epsilon_\gamma(400\ keV)} - N_0 \times \epsilon_{BG}}{\epsilon_\gamma(250keV)} \tag{A.22}$$

$$N_c = \frac{\frac{200}{0.38} - 424}{0.20} = 512$$

$$N_{f1} = \frac{\frac{N_{250}}{\epsilon_\gamma(250\ keV)} - N_c \times \epsilon_\gamma(400\ keV) - N_0 \times \epsilon_{BG}}{\epsilon_{BG}}$$

$$= \frac{\frac{160}{0.20} - 568 \times 0.38 - 424}{0.57} = 281$$

# Annexe2: Down-scale factors for triggers

As discussed in Sect. 2.4, only certain triggers are down-scaled so that the disk storage capacity is not overloaded and to reduces the dead time veto of writing to disk. The TBits relevant to the present analysis which are down-scaled are the Good Beam and Fragment (refer Tab. 2.1). In order to show how the down-scaling factor were obtained we reiterate the important working principles of the triggers and how a TPat is written for an event. Firstly, if two separate TBits are true for an event, with neither of them undergoing the down-scaling factor in that event, then the TPat value of that event is set as a combination of both those TBits. Secondly, each TBit set true for an event undergoes the down-scaling process separately thus, one TBit might be down-scaled while the other is not so only one will be written in the TPat of the Event.

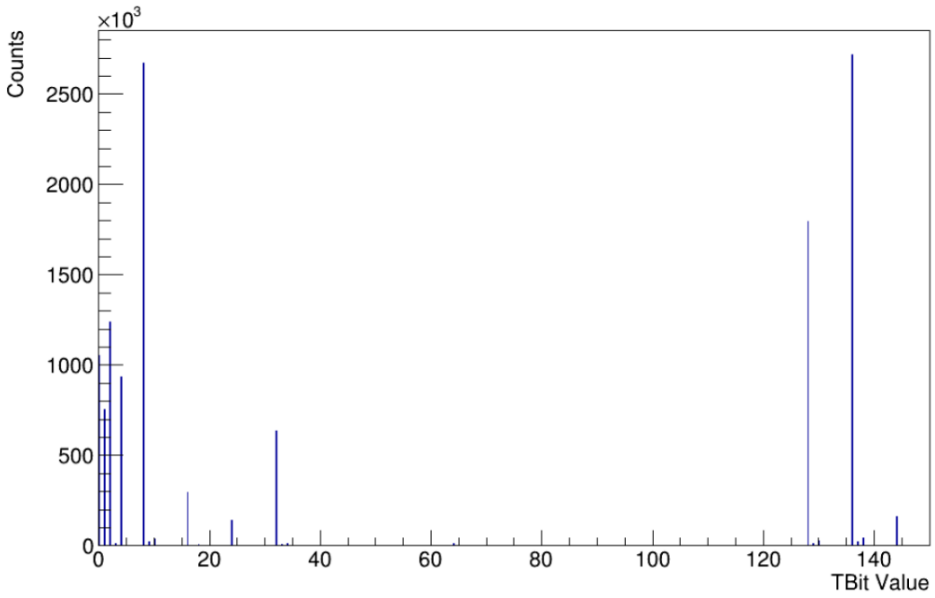


**Figure A.1** – Trigger pattern for CH 2 target with no external condition

Now referring to Tab. 2.1, we note something interesting: the TBits Good Beam and Fragment is already present in the logic of the reaction TBits Neutron and XB Sum. Thus, if these TBits were not down-scaled, they would always be present if the Neutron and XB Sum TBits were set. In other words, if there was no down-scaling in say the Fragment TBit and assume for an event the Neutron TBit was set true, this would consequently mean that the Fragment TBit is also set true and the TPat of the event instead of being 128 ($2^7$ ) (Table2.1) will always be set to 130 ($2^1$ + $2^7$ ). However, since the Fragment TBit is down-scaled, the value 130 will also be down-scaled by the same factor, and for events, in which it is down-scaled the TPat will be set to only 128 (see figure A for reference). Therefore, to get the down-scaling factor

for the Fragment TBit we divide all events whenever the Neutron TBit is set by the Number of events whenever both TBits are set (TPat Value 130).

# Annexe3: Final state interaction (FSI)

The annex is dedicated to the presentation of the model used to fit Dalitz plots ( adapted from the Appandix B in Ref. [133]).

## n-n correlations: presentation of the model

In the formalism of Ref. [97], the correlation function for neutrons of four-momenta $p_i$ emitted at a space-time relative distance $x = (\vec{r}, t)$ has two terms, originating respectively from Fermi statistics and the $s$-wave FSI, averaged over the distribution of distances:

$$C_{nn}(p_1, p_2) = 1 + \langle b_0 \rangle + \langle b_i \rangle \tag{A1}$$

$$\langle b_0 \rangle = -\frac{1}{2} \langle \cos(qx) \rangle \tag{A2}$$

$$\langle b_i \rangle = \frac{1}{2} \Big\{ |f(k^\star)|^2 \langle |\phi_{p_1 p_2}(x)|^2 \rangle + 2\, \Re \left[ f(k^\star) \langle \phi_{p_1 p_2}(x) \cos(qx/2) \rangle \right] \Big\} \tag{A3}$$

The metric is such that $p^2 = |\vec{p}|^2 - p_0^2$, the superscript $^\star$ refers to the $2n$ center of mass, $q = p_1 - p_2$ is the relative four-momentum, $k^\star = \sqrt{q^2}/2$ is the four-momentum of each neutron, and $f$ is their scattering amplitude:

$$f(k^\star) = \left( -1/a_{nn} + k^{\star 2} d_0/2 - i k^\star \right)^{-1} \tag{A4}$$

depending on the scattering length $a_{nn}$ and effective range $d_0$ (we use $-18.5$ and 2.8 fm, respectively). The $2n$ wave function is factorized assuming $r^\star \gtrsim d_0$ as $f(k^\star)\phi_{p_1 p_2}(x)$, with the exact form of $\phi_{p_1 p_2}(x)$ given in Ref. [97]. However, note that the final expression of $C_{nn}$ (A8) does not depend on the form of $\phi_{p_1 p_2}(x)$.

If we now assume a spherically symmetric source $W$ and neglect its momentum dependence:

$$\langle b_0 \rangle = -\frac{1}{2} \int W(x)\, \cos(qx)\, d^4x \tag{A5}$$

$$\langle b_i \rangle = \int 2\pi r_T dr_T dr_L dt\, W(x) \Big\{ |f(k^\star)\phi_{p_1 p_2}(x)|^2 + 2\Re[f(k^\star)\phi_{p_1 p_2}(x)] J_0\Big(\frac{q_T r_T}{2}\Big) \cos\Big(q_0 \frac{r_L - vt}{2v}\Big) \Big\} \tag{A6}$$

with $L/T$ the directions parallel/perpendicular to the velocity $v$ of the pair. For a Gaussian source of the form $W(x) = \exp(-r^2/4r_0^2 - t^2/4\tau_0^2)$ and small enough energies ($k^\star \ll m$), after

integration over $t^\star$:

$$\langle b_0 \rangle = -\frac{1}{2}\exp(-4k^{\star 2}r_0^2 - q_0^2\tau_0^2) \tag{A7}$$

$$\begin{aligned}\langle b_i \rangle &= \frac{1}{2\sqrt{\pi}r_0^2\gamma\rho}\int r_T dr_T dr_L^\star \exp(-r_T^2/4r_0^2 - r_L^{\star 2}/4\gamma^2\rho^2) \\ &\times\left\{\frac{|f|^2}{2r^{\star 2}} + \Re\left[f\frac{\exp(ik^\star r^\star)}{r^\star}\right]J_0\left(\frac{q_T r_T}{2}\right)\cos\left(\frac{q_0 r_L^\star}{2\gamma v}\right)\right\} \\ &-(1/8\sqrt{\pi})|f|^2 d_0/\gamma\rho r_0^2\end{aligned} \tag{A8}$$

with $\rho = \sqrt{r_0^2 + v^2\tau_0^2}$. The last term in (A8) is a first-order correction of the integration of the expression used for $\phi_{p_1p_2}(x)$ in the region $r^\star < d_0$.

In the case of simultaneous emission and/or very small velocities ($\gamma\rho \approx r_0$) the final expression becomes analytical, with only one free parameter ($r_0$):

$$\begin{aligned}C_{nn}(q_{nn}) &= 1 - \frac{1}{2}\exp(-q_{nn}^2 r_0^2) + \frac{|f|^2}{4r_0^2}\left(1 - \frac{d_0}{2\sqrt{\pi}r_0}\right) \\ &+\frac{\Re f}{\sqrt{\pi}r_0}F_1(q_{nn}r_0) - \frac{\Im f}{2r_0}F_2(q_{nn}r_0)\end{aligned} \tag{A9}$$

with $F_1(z) = e^{-z^2}/z\int_0^z e^{x^2}dx$ and $F_2(z) = (1 - e^{-z^2})/z$. Otherwise one should use (A7,A8), with two free parameters $(r_0, \tau_0)$ From the source parametrization used, one obtains $rms = \sqrt{6}r_0$ and $\tau = \sqrt{2}\tau_0$. Note that this model cannot be applied for $r_0 \lesssim 1fm$ ($rms \lesssim 2.5fm$), since then the result is completely determined by the short-distance behavior of $\phi_{p_1p_2}(x)$ in (A3), sensitive to the form of the $n$-$n$ potential.

# Bibliography


[1] https://www.nndc.bnl.gov.

[2] H. A. Bethe and R. F. Bacher, Rev. Mod. Phys. 8, 82 (1936).

[3] N. Bohr and J. A. Wheeler, Phys. Rev. 56, 426 (1939).

[4] N. Bohr, Phys. Rev. 55, 418 (1939).

[5] M. G. Mayer, Phys. Rev. 74, 235 (1948).

[6] M. G. Mayer, Phys. Rev. 75, 1969 (1949).

[7] M. G. Mayer, Phys. Rev. 78, 16 (1950).

[8] M. G. Mayer, Phys. Rev. 78, 22 (1950).

[9] K. Heyde, Basic ideas and concepts in nuclear physics (CRC Press, 2004).

[10] W. Greiner and J. A. Maruhn, Nuclear Models (Springer-Verlag Berlin Heidelberg Copyright Holder, 1996).

[11] A. Bohr and B. Mottelson, Nuclear Structure, Vol. 1, World Scientific Publishing, Singapore (1998).

[12] Shan-Gui Zhou, Jie Meng, and P. Ring, Phys. Rev. C 68 (2003) 034323.

[13] Lu-Lu Li, *et al*., Chin. Phys. Lett. 29 (2012) 042101.

[14] L. Li, *et al*., Phys. Rev. C 85 (2012) 024312.

[15] S. Zhou, *et al*., Phys. Rev. C 82 (2010) 011301(R).

[16] http://hyperphysics.phy-astr.gsu.edu/hbase/Nuclear/shell.html

[17] Ridha, Ali. (2016). Chapter Two (Binding Energy  Nuclear Models).

[18] A. Bohr and B. R. Mottelson, Nuclear Structure (World Scientific, 1998).

[19] D. J. Rowe, J. L. Wood, Fundamentals of Nuclear Models:  Foundational Models (World Scientific, 2010).

[20] V. Zelevinsky and A. Volya, Physics of Atomic Nuclei (Wiley-VCH, Weinheim, 2017).

[21] C. L. Henning, "Collectivité des noyaux de Zinc riches en neutrons par mesure de temps de vie avec le démonstrateur AGATA. Développement d'une cible d'hydrogène et physique aux énergies relativistes", PhD thesis(2013).

[22] M. M. Hammad, M. M. Yahia, S. B. Doma, "Visualization of some energy levels of even-even Nuclei" (2019).hal-02268933. https://hal.archives-ouvertes.fr/hal-02268933.

[23] A. Bohr, B.R. Mottelson and D. Pines, Phys. Rev. 110, 4 (1958).

[24] M. Matsuo, Phys. Rev. C 73, 044309 (2006).

[25] Grosse, E., Stephens, F. S., Diamond, R. M. (1973). Test of backbending models using odd-A nuclei. Physical Review Letters, 31(13), 840.

[26] L.N. Cooper, R.L. Mills, and A.M. Sessler, Phys. Rev. 114, 1377-1382 (1959).

[27] J. Dobaczewski, H. Flocard, J. Treiner, Nucl. Phys. A 422, 103 (1984).

[28] J. Dobaczewski, W. Nazarewicz, T.R. Werner, J.F. Berger, C.R. Chinn, J. Dechargé, Phys. Rev. C 53, 2809 (1996).

[29] P.-G. Reinhard, M. Bender, K. Rutz, J.A. Maruhn, Z., Phys. A 358, 277 (1997).

[30] M. Bender, K. Rutz, P.-G. Reinhard, J.A. Maruhn, Eur. Phys. J. A 8, 59 (2000).

[31] N. Tajima, Phys. Rev. C 69 034305 (2004).

[32] Bucurescu D. Zamfir N., "Fine structure of alpha decay of even-even trans-lead nuclei - An intriguing nuclear structure paradigm", Journal of Physics Conference (2013).

[33] A1 - Ozawa, A., Kobayashi, T., Suzuki, T., Yoshida, K., Tanihata, I., "New Magic Number, $N = 16$, near the Neutron Drip Line", Phys. Rev. Lett. (2000).

[34] G. F. Bertsch and H. Esbensen, Ann. Phys. (N.Y.) 209, 327 (1991).

[35] J. Dobaczewski, W. Nazarewicz, T. R. Werner, J. F. Berger,C. R. Chinn, and J. Dechargé, Phys. Rev. C 53, 2809 (1996).

[36] J. Dobaczewski, W. Nazarewicz, and P.-G. Reinhard, Nucl. Phys. A 693, 361 (2001).

[37] J. Dobaczewski and W. Nazarewicz, Prog. Theor. Phys. Suppl. 146, 70 (2002); J. Dobaczewski, W. Nazarewicz, and M. V. Stoitsov, Eur. Phys. J. A 15, 21 (2002).

[38] P. G. Hansen and B. Jonson, Europhys. Lett. 4, 409 (1987).

[39] M. V. Zhukov, B. V. Danilin, D. V. Fedorov, J. M. Bang, I. J. Thompson, and J. S. Vaagen, Phys. Rep. 231, 151 (1993).

[40] F. Barranco, P. F. Bortignon, R. A. Broglia, G. Coló, and E. Vigezzi, Eur. Phys. J. A 11, 385 (2001).

[41] S. Aoyama, K. Katō, and K. Ikeda, Prog. Theor. Phys. Suppl. 142, 35 (2001); T. Myo, S. Aoyama, K. Katō, and K. Ikeda, Prog. Theor. Phys. 108, 133 (2002).

[42] K. Hagino and H. Sagawa, Phys. Rev. C 72, 044321 (2005).

[43] D. Sackett, K. Ieki, A. Galonsky, C. A. Bertulani, H. Esbensen, J. J. Kruse, W. G. Lynch, D. J. Morrissey, N. A. Orr, B. M. Sherrill, H. Schulz, A. Sustich, J. A. Winger, F. Deák, Á. Horváth, Á. Kiss, Z. Seres, J. J. Kolata, R. E. Warner, and D. L. Humphrey, Phys. Rev. C 48, 118 (1993).

[44] S. Shimoura, T. Nakamura, M. Ishihara, N. Inabe, T. Kobayashi, T. Kubo, R. H. Siemssen, I. Tanihata, and Y. Watanabe, Phys. Lett. B348, 29 (1995).

[45] M. Zinser, F. Humbert, T. Nilsson, W. Schwab, H. Simon, T. Aumann, M. J. G. Borge, L. V. Chulkov, J. Cub, Th. W. Elze, H. Emling, H. Geissel, D. Guillemaud-Mueller, P. G. Hansen, R. Holzmann, H. Irnich, B. Jonson, J. V. Kratz, R. Kulessa, Y. Leifels, H. Lenske, A. Magel, A. C. Mueller, G. Münzenberg, F. Nickel, G. Nyman, A. Richter, K. Riisager, C. Scheidenberger, G. Schrieder, K. Stelzer, J. Stroth, A. Surowiec, O. Tengblad, E. Wajda, and E. Zude, Nucl. Phys. A619, 151 (1997).

[46] K. Ieki, A. Galonsky, D. Sackett, J. J. Kruse, W. G. Lynch, D. J. Morrissey, N. A. Orr, B. M. Sherrill, J. A. Winger, F. Deák, Á. Horváth, Á. Kiss, Z. Seres, J. J. Kolata, R. E. Warner, and D. L. Humphrey, Phys. Rev. C 54, 1589 (1996).

[47] A. J. Leggett, in Modern Trends in the Theory of Condensed Matter, edited by A. Pekalski and R. Przystawa, Vol. 115 of Lecture Note in Physics (Springer-Verlag, Berlin, 1980); J. Phys.(Paris) 41, C7–19 (1980).

[48] P. Nozières and S. Schmitt-Rink, J. Low Temp. Phys. 59, 195 (1985).

[49] J. Bardeen, L. N. Cooper, and J. R. Schrieffer, Phys. Rev. 108, 1175 (1957); P. G. de Gennes, Superconductivity of Metals and Alloys (Benjamin, New York, 1966); M. Tinkham, Introduction to Superconductivity (McGraw-Hill, New York, 1975).

[50] C. A. R. Sá de Melo, M. Randeria, and J. R. Engelbrecht, Phys.Rev. Lett. 71, 3202 (1993).

[51] J. R. Engelbrecht, M. Randeria, and C. A. R. Sá de Melo, Phys.Rev. B 55, 15153 (1997).

[52] M. Randeria, in Bose-Einstein Condensation, edited by A. Griffin, D. Snoke, and S. Stringari (Cambridge Univ. Press, Cambridge, U.K., 1995).

[53] K. Hagino, H. Sagawa, J. Carbonell and P. Schuck, Phys. Lett. 99, 022506 (2007).

[54] F. London, Nature 141, 3571 (1938).

[55] O. Sorlin and M.-G. Porquet (2013), Phys. Scr. T152, 014003.

[56] A. Barrière, " Study of the $^{13}$B magicity through neutron QFS knockout reaction $^{13}$B(p,pn) $^{12}$B", Master thesis, 2021.

[57] Aumann, T., Navin, A. *et al*., One-Neutron Knockout from Individual Single-Particle States of $^{11}$Be, Phys. Rev. Lett., 2000.

[58] Datar, V M, *et al*. (2013), "Electromagnetic Transition from the $4^+$ to $2^+$ Resonance in $^8$Be Measured via the Radiative Capture in $^4$He+$^4$He," Phys. Rev. Lett. 111 (6), 062502, arXiv:1305.1094 [nucl-ex].

[59] M. Freer *et al*., "Microscopic Clustering in Light Nuclei", Rev. Mod. Phys, 2018.

[60] Charity, R J, *et al*. (2015), "Spin alignment of excited projectiles due to target spin-flip interactions," Phys. Rev. C 91(2), 024610.

[61] Krieger, A, *et al*. (2012), "Nuclear Charge Radius of $^{12}$Be," Phys. Rev. Lett. 108, 142501, arXiv:1202.4873 [physics.atom-ph].

[62] Nörtershäuser, W, *et al*. (2009), "Nuclear Charge Radii of $^7$Be, $^9$Be, $^{10}$Be and the one-neutron halo nucleus $^{11}$Be," Phys. Rev. Lett. 102, 062503, arXiv:0809.2607 [nucl-ex].

[63] Kanada-En′yo and Y, Horiuchi H. Cluster structures of the ground and excited states of $^{12}$Be studied with antisymmetrized molecular dynamics. Phys Rev C, 2003, 68: 014319

[64] E. Liatard, J. F. Bruandet, *et al*. “Matter Distribution in Neutron-Rich Light Nuclei and Total Reaction Cross-Section”. Europhys. Lett., 13, 1990.

[65] I. Tanihata, T. Kobayashi, *et al*. “Measurement of interaction cross sections using isotope beams of Be and B and isospin dependence of the nuclear radii”. Physics Letters B, 206, 1988.

[66] T. Suzuki, R. Kanungo, *et al*. “Nuclear radii of 17, 19B and 14Be”. Nuclear Physics A, 658, 1999.

[67] N. Imai *et al*., "First lifetime measurement of $2_1^+$ state in 12Be", Phys. Lett. B, 2009.

[68] H. Iwasaki *et al*., "Low-lying intruder 1 state in 12Be and the melting of the N=8 shell closure", Phys. Lett. B, 2000.

[69] A. Navin *et al*., "Direct Evidence for the Breakdown of the N=8 Shell Closure in $^{12}$Be", Phys. Rev. Lett., July 2000.

[70] R. Meharchand, R. G. T. Zegers, B. A. Brown *et al*., Phys. Rev.Lett. 108 (2012) 122501.

[71] Suzuki, Toshio, and Takaharu Otsuka (1997), “Gamow-Teller transitions from $^{11}$Li and $^{12}$Be,” Phys. Rev. C (56).

[72] S. Pain *et al*., Phys. Rev. Lett., 96 (2006).

[73] S Shimoura *et al*., "Isomeric $0^+$ state in $^{12}$Be, Phys. Lett. B, 2003.

[74] J. G. Johansen *et al*., Phys. Rev. C 88 (2013) 044619.

[75] R. Kanungo *et al*., Phys. Lett. 682 (2010) 391.

[76] J. Chen *et al*., Phys. Rev. C 98 (2018) 014616.

[77] H. T. Fortune, G.-B. Liu, and D. E. Alburger, Phys. Rev. C 50, 1994.

[78] C. Morse *et al*., "Enhanced collectivity in $^{12}$Be", Phys. Lett. B, 2018.

[79] H. T. Fortune, Eur. Phys. J A 52 (2016) 11.

[80] P.G. Hansen, Studies of Single-Particle Structure at and Beyond the Drip Lines, Nucl. Phys. A 682 (2001) 310

[81] I. Tanihata *et al*., Measurements of Interaction Cross Sections and Nuclear Radii in the Light p-Shell Region, Phys. Rev. Lett. 55 (1985) 2676.

[82] I. Tanihata, Research opportunities with accelerated beams of radioactive ions, Nucl. Phys. A 693 (2001) 1.

[83] T. Kobayashi *et al*., Projectile fragmentation of the extremely neutron-rich nuclei at 0.79 GeV/nucleon, Phys. Rev. Lett. 60 (1988) 2599.

[84] D. Cortina, Knockout reactions: experimental aspects.

[85] C. A. Bertulani and A. Gade. MOMDIS: a Glauber model computer code for knockout reactions. Computer Physics Communications, 175(5):372–380, September 2006. doi:10.1016/j.cpc.2006.04.006.

[86] C. A. Bertulani and P. G. Hansen. Momentum distributions in stripping reactions of radioactive projectiles at intermediate energies. Physical Review C, 70(3), September 2004. doi:10.1103/physrevc.70.034609.

[87] C. A. Bertulani and C. De Conti. Pauli blocking and medium effects in nucleon knockout reactions. Physical Review C, 81(6), June 2010. doi:10.1103/physrevc.81.064603.

[88] J. Tostevin, Single-nucleon knockout reactions at fragmentation beam energies Nucl. Phys. A 682 (2001) 320.

[89] V. Maddalena, Single-neutron knockout reactions: Application to the spectroscopy of $^{16,17,19}$C, Phys. Rev. C (63) 024613.

[90] J.Tostevin, Core Excitation in Halo Nucleus Break-Up, Jour. Phys. G 25 (1999) 735.

[91] Q. Deshayes. Les isotopes d'azote au-delà de la limite de stabilité neutronique: $^{23}$N, $^{24}$N et $^{25}$N. PhD Thesis, Université de Caen Normandie, 2017. http://www.theses.fr/2017NORMC243.

[92] Christoph Langer. Coulomb dissociation of $^{31}$Cl and $^{32}$Ar - constraining the rp process. PhD thesis, 2012.

[93] Aldric Revel. Nuclear forces at the extremes, PhD Thesis, 2018

[94] H. Geissel, et. Al. The gsi projectile fragment separator (frs): a versatile magnetic system for relativistic heavy ions. Nuclear Instruments and Methods in Physics Research Section B: Beam Interactions with Materials and Atoms, 70(1):286 − 297, 1992.

[95] J. K. Smith *et al.*, Low-lying neutron unbound states in $^{12}$Be, Phys. Rev. C 90, 024309, 2014.

[96] H. T. Fortune, Nature of the En = 1.24 MeV state in $^{12}$Be, Eur. Phys. J. A, 2016.

[97] R. Lednicky and V. L. Lyuboshits. Final State Interaction Effect on Pairing Correlations Between Particles with Small Relative Momenta. Sov. J. Nucl. Phys., 35:770, 1982. [Yad.Fiz.35, 1316(1981)].

[98] R. Thies. Prototype Tests and Pilot Experiments for the R3B Scintillator-Based Detection Systems. Master thesis, 2011. Chalmers University of Technology.

[99] Ina J. Syndikus, Proton-Knockout Reactions from Neutron-Rich N Isotopes at $R^3B$, PhD thesis, 2018. Technischen Universität Darmstadt.

[100] Valerii Panin, Fully Exclusive Measurements of Quasi-Free Single-Nucleon Knockout Reactions in Inverse Kinematics, PhD thesis, 2012. Technischen Universität Darmstadt.

[101] C. R. Hoffman *et al.*, Observation of a two-neutron cascade from a resonance in $^{24}$O, Phys. Rev. C 83, 031303(R), 2011.

[102] A. Schiller *et al.*, Selective Population and Neutron Decay of an Excited State of $^{23}$O,

[103] C.A. Kalfas *et al.*, A software package for nuclear and atomic spectroscopy,

[104] J. Alcaraz, *et al.*, "The alpha magnetic spectrometer silicon tracker: Performance results with protons and helium nuclei". Nuclear Instruments and Methods in Physics Research A, vol. 593, pp. 376–398, Aug. 2008.

[105] http://ams-02project.jsc.nasa.gov/.

[106] F. Wamers, "Quasi-Free-Scattering and One-Proton-Removal Reactions with the Proton-Dripline Nucleus $^{17}$Ne at Relativistic Beam Energies". PhD thesis, Technischen Universitat in Darmstadt, Germany, 2011.

[107] K. Mahata, H. Johansson, S. Paschalis, H. Simon, and T. Aumann, "Position reconstruction in large-area scintillating fibre detectors". Nuclear Instruments and Methods in Physics Research Section A: Accelerators, Spectrometers, Detectors and Associated Equipment, vol. 608, no. 2, pp. 331 – 335, 2009.

[108] J. Cub, *et al.*, "A large-area scintillating fibre detector for relativistic heavy ions". Nuclear Instruments and Methods in Physics Research Section A: Accelerators, Spectrometers, Detectors and Associated Equipment, vol. 402, no. 1, pp. 67 – 74, 1998.

[109] T. Blaich, *et al.*, "A large area detector for high-energy neutrons".Nuclear Instruments and Methods in Physics Research Section A: Accelerators, Spectrometers, Detectors and Associated Equipment, vol. 314, no.1, pp.136–154, 1992.

[110] H. T. Johansson, "The daq always runs". Master's thesis, Chalmers University of Technology, Goteborg, Sweden, 2006.

[111] Stefanos Paschalis, "Relativistic One-Nucleon Removal Reactions". PhD thesis, University of Liverpool, 2008.

[112] Dominic M. Rossi, "Investigation of the Dipole Response of Nickel Isotopes in the Presence of a High-Frequency Electromagnetic Field". PhD thesis, Johannes Gutenberg Universität Mainz, 2009.

[113] Cristoph Caesar, January 2015. Private communication.

[114] Matthias Holl, "Quasi-Free Scattering from Relativistic Neutron-Deficient Carbon Isotopes". PhD thesis, Technischen Universität Darmstadt, 2014.

[115] Julian Kahlbow, "One-Neutron Removal Reactions on $^{11}$Be and $^{12}$Be". Master thesis, Technische Universtät Darmstadt, 2015.

[116] Alexandre Lepailleur, "Étude du noyau peu lié de $^{26}$F pour sonder l'évolution des forces nucléaires à l'approche de la limite de liaison nucléaire"

[117] Ronja Thies, "Prototype tests and pilot experiments for the R3B scintillator-based detection systems". Master thesis, Chalmers University of Technology, 2011.

[118] S. Bedoor *et al.*, "Structure of $^{14}$C and $^{14}$B from the $^{14,15}$C(d, 3 He)$^{13,14}$B reactions", PRC (2016).

[119] C. Patrignani, *et al.*, "Review of Particle Physics", Chinese Physics C, 2016. doi:10.1088/1674-1137/40/10/100001.

[120] Steve Baker and Robert D. Cousins, "Clarification of the use of chi-square and likelihood functions in fits to histograms". Nuclear Instruments and Methods in Physics Research, 1984.

[121] Donald H. Perkins, "Introduction to High Energy Physics". Cambridge University Press, 4edition, 2000.

[122] M. Nikolic , "Kinematics and multiparticle systems". Documents on modern physics. Gordonand Breach, 1968.

[123] F. M. Marques, M. Labiche, *et al*. "Three-body correlations in Borromean halo nuclei".Phys. Rev. C, 64, 2001. https://link.aps.org/doi/10.1103/PhysRevC.64.061301

[124] B. Laurent and F. M. Marques. "Chronology of the three-body dissociation of $^{8}$He", 2018.

[125] A. Spyrou, Z. Kohley, T. Baumann, D. Bazin, B. A. Brown, G.Christian, P. A. DeYoung,J. E. Finck, N. Frank, E. Lunderberg, S. Mosby, W. A. Peters, A. Schiller, J. K. Smith,J. Snyder, M. J. Strongman, M. Thoennessen, and A. Volya. "First observation of ground state dineutron decay:$^{16}$Be", Phys. Rev. Lett., 108:102501, Mar 2012.

[126] F. M. Marques *et al*., "Two-neutron interferometry as a probe of the nuclear halo", Phys.Lett., B476:219–225, 2000.

[127] G. Normand,"Investigation of correlations in light neutron-rich nuclei". Theses, Universite de Caen, October 2004.

[128] https://www.nndc.bnl.gov/ensdf/

[129] B.Jäckel, W.Westmeier, P.Patzelt, "On the photopeak efficiency of germanium gamma-ray detectors", Nuclear Instruments and Methods in Physics Research Section A, 1987.

[130] W. A. Peters *et al*., "Neutron knockout of $^{12}$Be populating neutron-unbound states in $^{11}$Be", Phys. Rev. C, 2011.

[131] J. Bardeen, L. N. Cooper and J. R. Schrieffer, "Theory of Superconductivity", Phys. Rev. 162 (1957), 108, 1175 (1957).

[132] F. London, " The $\alpha$ Phenomenon of Liquid Helium and the Bose-Einstein Degeneracy", Nature 141, 3571 (1938).

[133] Belen Monteagudo Godoy. Structure and neutron decay of the unbound Beryllium isotopes $^{15,16}$Be, PhD Thesis, 2019.

[134] W. von Oertzen and A. Vitturi, " Pairing correlations of nucleons and multi-nucleon transfer between heavy nuclei", Rep. Prog. Phys 64, 1247 (2001).

[135] D. Montanari *et al*.," Neutron Pair Transfer in $^{60}$Ni+$^{116}$Sn Far below the Coulomb Barrier", Phys. Rev. Lett. 113, 052501 (2014).

[136] K. Hagino, H. Sagawa, J. Carbonell and P. Schuck, "Coexistence of BCS and BEC-like pair structures in halo nuclei", Phys. Lett. 99, 022506 (2007).

[137] U.C. Bergmann *et al*., "New information on $\beta$-delayed neutron emission from $^{12,14}$Be", Nucl. Phys. A, 1999.

[138] Bergmann, U., Borge, M., Cederkäll, J. *et al*. Analysis of decay data from neutron-rich nuclei. Eur Phys J A 11, 279–284 (2001).

[139] P. L. Reeder, R. A. Warner, W. K. Hensley, D. J. Vieira, and J. M. Wouters, Phys. Rev. C 44, 1991.

[140] M. S. Curtin, L. H. Harwood, J. A. Nolen, B. Sherrill, Z. Q. Xie, and B. A. Brown, Phys. Rev. Lett. 56, 1986.

[141] D. E. Alburger, D. P. Balamuth, J. M. Lind, L. Mulligan, K. C. Young, Jr., R. W. Zurmühle, and R. Middleton, Phys. Rev. C 17, 1978.

[142] H. T. Fortune, G.-B. Liu, and D. E. Alburger, Phys. Rev. C 50, 1994.

[143] T. Otsuka *et al*., Phys. Rev. Lett., 87 (2001).

[144] H. Fortune and R. Sherr, Phys. Rev. C, 74 (2006).

[145] D. E. Alburger, S. Mordechai, H. T. Fortune and R. Middleton, Phys. Rev. C 18, 1978.

[146] M. H. Macfarlane and J. B. French, Rev. Mod. Phys. 32, 1960.

[147] J. P. Schiffer *et al*., Phys. Rev. Lett. 108, 022501 (2012).

[148] J. P. Schiffer *et al*., Phys. Rev. C 87, 034306 (2013).

[149] J. P. Schiffer *et al*., Phys. Rev. Lett. 100, 112501 (2008).

[150] L. Lapikás, Nucl. Phys. A 553, 297c (1993).

[151] G. J. Kramer, H. P. Blok, and L. Lapikás, Nucl. Phys. A, 2001.

[152] H. T. Fortune, Nucl. Instrum. Methods Phys. Res., Sect. A 681, 7 (2012).

[153] H.G. Bohlen, *et al*., "Structure of neutron-rich beryllium and carbon isotopes", Nuclear Physics A (2004).

[154] Y. Hirayama, *et al*., "Study of 11Be structure through $\beta$-delayed decays from polarized $^{11}$Li, Phys. Lett. B (2005).

[155] R.E. Azuma *et al*., Phys. Rev. Lett., 43 (1979), p. 1652.

[156] N. Aoi *et al*., Nucl. Phys. A, 616 (1997), p. 181c.

[157] D.J. Morrissey *et al*., Nucl. Phys. A, 627 (1997), p. 222.

[158] G.-B. Liu and H.T. Fortune, Phys. Rev. C, 42 (1990).

[159] F. Sarazin *et al*., "Halo Neutrons and the Beta Decay of $^{11}$Li", Nucl. Phys. Group, 2004.

[160] F.M. Marqués et al , Phys. Lett. B 476, 219 (2000).

[161] F.M. Marqués et al , Phys. Rev. C 64, 061301 (2001).

[162] A. Revel et al , Phys. Rev. Lett. 120, 152504 (2018).

[163] G. Normand, PhD Thesis, Université de Caen (2004).

[164] J.K. Smith et al , Nuc. Phys. A 955, 27 (2016).

[165] B.A. Brown *et al*., "Absolute spectroscopic factors from nuclear knockout reactions", Physical Review C, Volume 65, 061601, 2002.

[166] C. A. Bertulani and A. Gade. MOMDIS, "A Glauber model computer code for knockout reactions", Computer Physics Communications, 175(5):372–380, 2006.

[167] C. A. Bertulani, private communication (2020).

[168] M. Holl *et al*., "Quasi-free neutron and proton knockout reactions from light nuclei in a wide neutron-to-proton asymmetry range", Phys. Lett. B (2019).

[169] C. Force, "Etude de la structure du $^{44}S$ par sa décroissance isomérique", phD thesis, 2009.

[170] S. Shimoura *et al*., Phys. Lett. B 654, 87 (2007).

[171] N. Imai *et al*., Phys. Lett. B 673, 179 (2009).

[172] H.T Fortune, Phy. Rev. C (2012).

[173] C. Yuan *et al*., Phys. Rev. C85 (2012) 064324

[174] H. Simon, *et al*., Systematic investigation of the drip-line nuclei 11Li and $^{14}$Be and their unbound subsystems $^{10}$Li and $^{13}$Be, Nuclear Physics A, Volume 791, Issues 3–4, (2007).

# Structure of $^{12}$Be via the study of multi-neutron decays and two-neutron correlations


## Abstract

We studied the structure of states in $^{12}$Be, produced by the $^{13}$B$(-1p)^{12}$Be reaction, via their decay patterns and neutron-neutron correlations. This nucleus is very interesting for studying nuclear structure at the dripline, because it is at the crossroad of nuclei with different configurations, from cluster to doubly-magic, as well as halo. For the first time we used a combined analysis of two and three-body decay-energy ($E_d$($^{11}$Be+1n and $E_d$($^{10}$Be+1n) and $\gamma$-ray spectra, as well as the Dalitz plots, allowing us to study states up to 18 MeV excitation energy. The cross-sections and spectroscopic factors are also measured and compared to theoretical calculations for all states. The n-n correlations are studied by the means of Dalitz plots, and discussed in terms of momentum alignment and angular correlations.



**Keywords**: Neutron dripline, Nuclear structure, Knockout reactions, Dalitz plots, Neutron-neutron correlations.



## Résumé

Ce travail de thèse a porté sur l'étude de la structure des états du $^{12}$Be peuplés par la réaction de knockout $^{13}$B$(-1p)^{12}$Be, via leurs modes de décroissance et l'étude des corrélations neutron-neutron. Ce noyau est très intéressant pour l'étude de la structure nucléaire loin de la stabilité, car il est au croisement de noyaux aux configurations différentes, allant des noyaux cluster (comme le $^{8}$Be) au noyaux doublement magiques ($^{14}$C), mais aussi les noyaux halo ($^{11}$Be et $^{14}$Be). Pour la première fois, une l'analyse combinée des spectres d'énergies à deux et trois corps ($E_d$($^{11}$Be+1n et $E_d$($^{10}$Be+1n) et des rayons $\gamma$, a été utilisé permettant d'étudier des états jusqu'à 18 MeV d'énergie d'excitation. Les sections efficaces et les facteurs spectroscopiques sont également mesurés et comparés à des calculs théoriques pour tous les états. Les corrélations neutron-neutron sont étudiés en utilisant les diagrammes de Dalitz, et discutés en termes d'alignement de moment angulaires et corrélations angulaires des neutrons émis.



**Mots clés**: Dripline neutron, Structure nucléaire, Réactions de knockout, Diagrammes de Dalitz, Corrélations neutron-neutron.